UNIVERSITY OF OKLAHOMA

GRADUATE COLLEGE

NANOMATERIAL BASED NON-INVASIVE CANCER DIAGNOSIS METHODS: CANCER IMAGING AND SMALL RNA QUANTIFICATION

A DISSERTATION

SUBMITTED TO THE GRADUATE FACULTY

in partial fulfillment of the requirements for the

Degree of

DOCTOR OF PHILOSOPHY

By

YUEYI SUN
Norman, Oklahoma
2020

Downloaded from SHAREOK. Persistent Handle URL: https://hdl.handle.net/11244/326703

NANOMATERIAL BASED NON-INVASIVE CANCER DIAGNOSIS METHODS: CANCER IMAGING AND SMALL RNA QUANTIFICATION

A DISSERTATION APPROVED FOR THE
DEPARTMENT OF CHEMISTRY AND BIOCHEMISTRY

BY THE COMMITTEE CONSISTING OF

Dr. Rakhi Rajan, Chair

Dr. Wai Tak Yip

Dr. Christina Bourne

Dr. Bin Wang

© Copyright by YUEYI SUN 2020
All Rights Reserved.

Acknowledgements

First of all, I would like to acknowledge the National Institutes of Health (NIH) and the U.S. Department of Energy for funding my research.

I would like to thank my major professor, Dr. Chuanbin, Mao for supporting and encouraging me to overcome the difficulties I have met during my PhD study. With his direction in knowledge and techniques, I could finally finish my interesting research and this dissertation.

I also give the sincerest gratitude to my dear dissertation and advisory committee members, Dr. Rakhi Rajan, Dr. Wai Tak Yip, Dr. Christina Bourne, and Dr. Bin Wang. Thank you for the thoughtful advice for not only my research projects but also teaching experience.

I am very grateful to be rounded by such great group members in Dr. Mao's lab, especially Dr. Binrui Cao and Dr. Penghe Qiu. As the most experienced scientists in our lab and great friends of my life, they never hesitate to share their opinion and experience to help me. Every time I discussed with them, I found points of view for my studies.

Additionally, I would like to express my special thanks to Greg Strout, Dr. Preston Larson, and Dr. Scott Russell who works or worked in Samuel Roberts Noble Microscopy Laboratory and helped me a lot with TEM imaging. I also want to thank Andria F. Hedrick in OUHSC. We worked together for radiation imaging. She was very helpful and nice.

Last but not least, I appreciate Dr. Xuewei Qu's accompany since my first year at OU. Thank you for teaching me all the techniques for cell culture and animal experiments. More importantly, thank you for cheering me up and calming me down when I had difficulties.

Table of Contents

Acknowledgements iv

List of Tables viii

List of Schemes ix

List of Figures x

Abstract xiii

Chapter 1: Introduction ..... - 1 -

1.1 General background ..... - 1 -

1.2 Cancer imaging ..... - 1 -

1.3 Cancer biomarker ..... - 3 -

1.4 Nanomaterials ..... - 4 -

1.4.1 Gold nanoparticles ..... - 5 -

1.4.2 Magnetic nanoparticles ..... - 8 -

1.4.3 Upconversion nanoparticles ..... - 10 -

1.4.4 Bacteriophages, bio-nanomaterials ..... - 12 -

Chapter 2: Non-invasive cancer imaging methods by using nanoparticles and phages ..... - 16 -

2.1 Introduction ..... - 16 -

2.2 Materials and methods of magnetic nanoparticle clusters ..... - 18 -

2.2.1 Preparation of iron oxide nanoparticles ..... - 18 -

2.2.2 Phase transfer of the as-prepared iron oxide nanoparticles from aqueous into oil ..... - 19 -

2.2.3 Preparation of iron oxide nanoparticles clusters ..... - 19 -

2.2.4 Preparation of silica coated MNPCs ..... - 20 -

2.2.5 Size sorting of MNPCs by PVP viscosity gradient medium ..... - 20 -

2.3 Materials and methods of targeted SPECT ..... - 20 -

2.3.1 M13 phage modification with the chelator NHS-MAG_3 ..... - 20 -

2.3.2 Radiation labeling with ^{99m}Tc (Technetium-99m) ..... - 21 -

2.3.3 Animal experiment for SPECT ..... - 21 -
2.4 Results of magnetic nanoparticle clusters ..... - 22 -
2.4.1 Phase transfer of IONPs and Characteristics of hydrophobic IONPs ..... - 22 -
2.4.2 Synthesis of MNPCs ..... - 29 -
2.4.3 Size distribution of MNPCs ..... - 33 -
2.5 Results of targeted SPECT ..... - 35 -
2.6 Conclusion and discussion ..... - 40 -
Chapter 3: Small RNA quantification methods by using nanoparticles ..... - 42 -
3.1 Introduction ..... - 42 -
3.2 Materials and method of pyro and magnetic beads based small RNA quantification ..... - 47 -
3.2.1 Pyro synthesis ..... - 47 -
3.2.2 Pyro labeled probe B ..... - 47 -
3.2.3 Probe A labeled magnetic bead ..... - 48 -
3.2.4 Detection sample preparation ..... - 48 -
3.3 Materials and method of NPMBs based small RNA quantification ..... - 48 -
3.3.1 Synthesis of Au NPs ..... - 48 -
3.3.2 DNA coating of Au NPs ..... - 49 -
3.3.3 Synthesis of UCNPs with green emission ..... - 49 -
3.3.4 DNA coating of UCNPs ..... - 50 -
3.3.5 Synthesis of NPMBs and the control group ..... - 50 -
3.3.6 Detection of the target DNA and RNA ..... - 51 -
3.4 Results of pyro and magnetic beads based small RNA quantification ..... - 51 -
3.4.1 Characterization of pyro and selection of laser treatment ..... - 51 -
3.4.2 Determination of detection range ..... - 52 -
3.4.3 Target miR-21 quantification ..... - 53 -
3.5 Results of NPMB based small RNA quantification ..... - 55 -
3.5.1 Characterization of UCNPs, Au NPs, and DNA modified NPs ..... - 55 -
3.5.2 Characterization of NPMBs and UCNP emission spectrum ..... - 59 -
3.5.3 Detection of DNA and RNA in different solutions ..... - 62 -
3.6 Conclusion and discussion ..... - 68 -

Chapter 4: Summary and discussion ..... - 70 -

4.1 Summary ..... - 70 -

4.2 Novel nanomaterials for cancer imaging ..... - 70 -

4.2.1 New MNPCs synthesis strategy for MRI ..... - 71 -

4.2.2 SPECT for tumor targeting imaging ..... - 71 -

4.3 Accurate and sensitive strategies for small RNA quantification ..... - 72 -

4.3.1 Small RNA quantification based on pyro ..... - 72 -

4.3.2 Low LOD quantification strategy for small RNA quantification ..... - 72 -

References ..... - 74 -

Appendix A: List of Abbreviations ..... - 82 -

Appendix B: List of Copyrights and Permissions ..... - 85 -

List of Tables

Table 2.1. DLS measurement of average size of nanoparticles after being transferred into oil by different anion species 26

Table 3.1. Probe and target sequences of NPMB 46

List of Schemes

Scheme 2.1 Proposed ligand structure on the surface of iron oxide nanoparticles after being transferred from aqueous to oil phase 28

Scheme 3.1 Structure of miR21-A probe/miR21/miR21-B probe complex 43

Scheme 3.2 Scheme of NPMB (nanoparticle based molecular beacon) 45

List of Figures

Figure 1.1 Absorbance spectra of spherical Au NPs of different sizes 6

Figure 1.2 Optical characters of Au NPs 6

Figure 1.3 Surface modification of AuNPs 8

Figure 1.4 Lymph nodes MRI results with and without a monocrystalline IONP 9

Figure 1.5 Principal mechanisms for upconversion (a) excited state absorption, (b) energy-transfer 11

Figure 1.6 NaYF4 nanoparticles with varied dopant ratios 11

Figure 1.7 Typical architecture of the therapeutic UCNPs-based composite 12

Figure 1.8 Phage life cycle 13

Figure 1.9 Basic structure of the M13 bacteriophage and the possible pathway of generic engineering 14

Figure 1.10 Antibody phage display and selection 15

Figure 2.1 Phase transfer of the as-prepared aqueous iron oxide nanoparticles into oil 23

Figure 2.2 Photographs of IONPs transferred from water to hexane by using sodium citrate as the polyanion species 24

Figure 2.3 Phase transfer of IONPs conducted by using sodium acetate and sodium carbonate as the anionic molecules 27

Figure 2.4 Phase transfer of IONPs using oleic acid as the hydrophobic capping molecules 29

Figure 2.5 Iron oxide MNPCs prepared by using hydrophobic nanoparticles obtained through phase transfer. 31

Figure 2.6 Magnetization curves of single and clustered IONPs at 5 and 300 K 32

Figure 2.7 Size sorting of MNPCs through centrifugation in a PVP based viscosity gradient medium 34

Figure 2.8 SPECT for human breast cancer MCF-7 xenograft model 36

Figure 2.9 Biodistribution at 4 h after injection 37

Figure 2.10 Biodistribution at 24 h after injection 39

Figure 3.1 Fluorescence of pyro and SOSG 52

Figure 3.2 Fluorescence of pyro and SOSG with different concentrations of pyro 53

Figure 3.3 Fluorescence of pyro and SOSG with different target miR21 concentrations.. 54

Figure 3.4 TEM image (a) and emission spectrum (b) of UCNPs 56

Figure 3.5 TEM image (a) and emission spectrum (b) of Au NPs 57

Figure 3.6 TEM image (a) and emission spectrum (b) of DNA modified UCNPs 58

Figure 3.7 TEM image of DNA modified UCNPs without IGEPAL® CO-520 59

Figure 3.8 TEM images of NPMB and control group; emission spectrum of control group, NPMBs, and DNA modified UCNPs..... 60

Figure 3.9 Peak fit image of UCNP emission spectrum..... 61

Figure 3.10 UCNPs emission spectrum with different target DNA concentrations 62

Figure 3.11 UCNPs emission spectrum with different target RNA concentration in aqueous solution..... 63

Figure 3.12 UCNPs emission intensity *vs* target RNA concentration in aqueous solution 64

Figure 3.13 UCNPs emission spectrum with different target RNA concentration in plasma 65

Figure 3.14 UCNPs emission intensity *vs* target RNA concentration in plasma 66

Figure 3.15 UCNPs emission intensity *vs* target RNA concentration in aqueous solution at different distance between laser and sample..... 67

Abstract

Cancer is a worldwide disease and causes millions of deaths every year. The fatality of cancer is responsible for approximating a sixth of global death. To reduce cancer mortality, early diagnosis is one of the key factors. If cancer is diagnosed at an early stage, cheaper and less invasive therapeutic strategies can be applied to increase the survival rate. Early non-invasive diagnosis methods for cancer include imaging and biomarker detection. My work mainly focused on developing nanomaterials-based probes for non-invasive cancer diagnosis through cancer imaging and biomarker quantification.

Chapter 2 includes two projects of developing nanoprobes for non-invasive cancer imaging. In Project 1, we developed a robust roundtrip phase transfer approach to construct magnetic nanoparticle clusters (MNPCs) using aqueous iron oxide nanoparticles (IONPs) that were prepared by a simple, scalable, and cost-effective method. The MNPCs have the potential to serve as a contrast agent to enhance magnetic resonance imaging (MRI) contrast. In Project 2, we constructed a radioactively labeled targeted phage for single-photon emission computed tomography (SPECT). Traditional SPECT for cancer imaging relies on the Enhanced Permeability and Retention (EPR) effect. However, research has shown that the EPR effect is specific to each cancer type and patient. The radioactively labeled cancer-targeting phage could overcome the limitation of the EPR effect and improve the SPECT for cancer.

Chapter 3 includes two projects of developing nanoprobes for RNA biomarker quantification. In Project 3, we recruited pyropheophorbide-a (pyro) and magnetic beads to quantify small RNA. Pyro has fluorescence and can produce singlet oxygen with laser treatment. In addition, the singlet oxygen production efficiency positively correlates to the laser power. We hypothesized that the quantification based on the singlet oxygen signal would reduce the limit of detection. However,

magnetic beads triggered singlet oxygen signal unexpectedly, which made this method failed to quantify target RNAs using the singlet oxygen signal. In Project 4, we developed a novel nanoparticle-based molecular beacon (NPMB). In this NPMB, the upconversion nanoparticle (UCNP) was used as a fluorophore, and the gold nanoparticle (Au NP) worked as a quencher. The exciting wavelength of UCNPs is longer than its emitting wavelength so that this method has an ultra-low background. This novel NPMB can detect both small DNA and RNA as low as aM level without purification.

Overall, we developed a MNPC and a radioactively labeled targeted phage with the potential of benefit MRI and SPECT for cancer imaging, respectively, as well as two small RNA quantification strategies to quantify cancer RNA biomarker.

Chapter 1: Introduction

1.1 General background

Cancer is a worldwide disease and causes millions of deaths every year. The fatality from cancer is only exceeded by cardiovascular diseases, and cancer deaths account for approximating one-sixth of global death.[1] Based on the estimation of WHO (World Health Organization), cancer caused 9.6 million deaths in 2018. To reduce cancer mortality, early diagnosis is one of the key factors. When cancer is diagnosed at stage 0 or stage I, cheaper, less invasive, and more effective treatment methods are more available and the patient has a higher possibility to recover.[1] Early diagnosis methods for cancer include non-invasive cancer imaging[2-3] and biomarker detection[4]. My work was developing non-invasive cancer diagnosis methods by using nanomaterials, including cancer imaging methods and biomarker quantification methods.

1.2 Cancer imaging

Current clinical cancer imaging methods are X-ray computed tomography (CT), magnetic resonance imaging (MRI), optical imaging, positron emission tomography (PET), single-photon emission computed tomography (SPECT), and ultrasound. CT, MRI, PET, and SPECT will be introduced here due to their 3D imaging ability.[5]

In CT, a rotary X-ray resource is used to examine the objective and the attenuation is recorded by a detector.[6] Because different tissues as well as the pathological tissue have different attenuation or projection values, the computer can analyze the signal and reconstruct the image. By collecting and stacking data from multiple tissue sections, CT is able to display a 3D image.[6]

CT is a powerful and common cancer diagnosis tool, especially effective for lung cancer. However, it has a limitation of 15% false positive results in all kinds of lesions.[7]

MRI detects nuclear magnetic resonance of elements inside bodies, such as hydrogen, carbon, oxygen, and phosphorus.[8] Hydrogen is frequently used in MRI due to its high sensitivity and the abundance of hydrogen in bodies. Different tissues contain different contents of the element that leads to diverse signal strength. In addition, the electronic environment is varying in tissues and influences the resonance frequency. As a result, lesions including tumors would appear differently in MRI so that could be diagnosed.[8] MRI is very useful to image cancer in soft tissues such as breast cancer.[8] MRI has high resolution but is limited in contrast.[9]

Although helper-reagent-uptake is not required for imaging, contrast media are used in CT and contrast agents are used in MRI to enhance contract in the clinic.[5]

Unlike X-ray CT and MRI, an injection of a radioactive substance is necessary for both PET and SPECT. PET detects positrons emitted by radionuclides with short half-lives while SPECT monitors γ proton from radionuclides with relatively long half-lives.[10-12] In PET, a metabolic substance is usually radioactively labeled such as ^{18}F-fludeoxyglucose, and injected into the patient. Because the metabolic rate is variable in tissues, higher metabolic rates result in aggregation of the radioactive labeled metabolic substance, and hence higher signal.[12] PET has an advantage in early diagnosis that can identify cancer lesions before tumor formation because metabolic activity increases in the cancer cells.[13] PET can also identify malignant tumors from benign tumors according to the higher metabolic activity in malignant tumors.[12] Similar to imaging by PET, a radioactively labeled substance is needed in SPECT, too.[10] The substance would accumulate in tumors due to the high permeability of the blood vessels in tumors. This accumulation effect is known as the Enhanced Permeability and Retention (EPR) effect. SPECT

is also able to identify malignant tumors. The malignant tumors have a higher potential to form vessels that leads to a higher accumulation of the radionuclides.[14] Although PET and SPECT have high sensitivity, their resolutions are relatively low.[10-12] Therefore, they are commonly combined with CT for cancer diagnosis.[10-12]

1.3 Cancer biomarker

Testing for cancer biomarkers in peripheral blood, including alpha-fetoprotein (AFP) and beta-human chorionic Gonadotropin (beta-HCG), have played a key role in cancer diagnosis for decades[15] In the last two decades, scientists have identified that some non-coding RNAs (ncRNAs) play significant roles in enhancing or suppressing cancers,[16-18] and these may be considered as a new type of cancer biomarkers. For example, piR-651 (piRNA) is highly expressed in all breast, lung, colon, and stomach cancer tumors and cells.[19] Other ncRNAs, for example, the lncRNAs: HOTAIR, LSINCT5, and MALAT1, and the miRNAs: miR-21 and major of miRNA 200 family (including miR-200a, b, c, as well as miR-141), are all commonly associated with multiple cancer types.[20-26]

ncRNA is a type of RNAs that does not encode a protein and can be classified by length or function. Those longer than 200 nucleotides (nt) are called long non-coding RNA (lncRNAs), such as Xist-RNA, Airn, and H19.[27] Other ncRNAs are called small non-coding RNAs (sncRNAs) including microRNAs (miRNAs) and short interfering RNAs (siRNAs).[27] ncRNAs are involved in various biological processes, such as translation, gene regulation, and RNA processing, by hybridizing with target nucleic acid or interacting with target proteins.[27] For examples, transfer RNAs (tRNAs) and ribosomal RNAs (rRNAs) assist mRNAs in translation;[28-29] small nuclear RNAs (snRNAs), small nucleolar RNAs (snoRNAs), and small cajal RNAs (scaRNAs) are associated with the RNA modifications;[30] sncRNAs are mainly involved in trans gene regulation

(e.g., gene expression and gene silence);[31] lncRNAs function as both cis- and trans-regulators and modulators of the genome.[32-33] In patients, the concentrations of these ncRNAs change that leads to an abnormal gene expression.[19-26] As a result, these ncRNAs are potential biomarkers for diseases including cancer.

The application of sensitive detection of diagnostic ncRNA cancer biomarkers will advance the current cancer diagnosis and therapy for many reasons. First, the cancer-associated ncRNAs in peripheral blood will reach the detectable levels earlier than the proteins.[34] The techniques for detecting the expression level of ncRNA biomarkers could break the time barriers of the conventional protein-depended cancer diagnosis methods, in order to achieve an early-stage diagnosis of cancers, which is extremely important for cancer treatment.[35] Second, only a small amount of tissue or body liquid sample is needed to determine the ncRNA expression levels for diagnosis. Therefore, it is less invasive compared to biopsy, the conventional cancer diagnosis method. Third, ncRNAs are not only efficient signatures for cancer diagnosis but also potential therapeutic drugs for cancer treatment. For example, ncRNAs miR-34a and siKras were delivered to treat lung cancer in mice. miR-34a activated the response of tumor suppressor gene p53 while siKras silenced the expression of oncogenic Kras.[36]

1.4 Nanomaterials

Nanomaterials (NMs) have been widely investigated for cancer diagnosis and treatment in recent decades mainly because they can approach lesions non-invasively.[14] Meanwhile, the surfaces of NMs are able to be modified and made biocompatible; the characteristic spectra of NMs are potentially applied for imaging and biomarker quantification; special properties of certain NMs such as optothermal response of gold nanoparticles (Au NPs)[37] and magnetism of magnetic

nanoparticles (MNPs)[38-39] can be utilized for specific objectives. In addition, several NMs could be combined to obtain multiple characteristics and thus achieve multi-functional NM.[14]

1.4.1 Gold nanoparticles

Au NPs are frequently used in cancer research due to the following reasons: (1) the synthesis method of Au NPs is simple and quick; (2) the shape and spectra are adjustable; (3) the surface can be easily modified to serve different research goals.[40]

Generally, the citrate reduction method is used to synthesize Au NPs.[41] In this method, spherical Au NPs are obtained within 30 min in a water bath.[41] Additionally, the sizes of Au NPs are tunable by adjusting the concentration of citrate.[42] To synthesize Au NPs in different shapes with tunable sizes, such as Au NRs (gold nanorod), Au ND (gold nanodendrites), and Au NS (gold nanostars), subsequent operations usually take less than 30 min at room temperature.[43-45]

The optical characteristics of Au NPs are determined by their sizes and shapes, hence, are also adjustable. As an example, for spherical Au NPs, the increase of the diameter causes red shifting of the absorbance spectrum. (Figure 1.1)[42] The absorbance spectrum of Au NRs has the same red-shifted pattern and the absorbance wavelength increases with larger Au NRs. However, compared with the single absorbance peak of spherical Au NPs, Au NRs have two absorbance peaks. (Figure 1.2)[46]

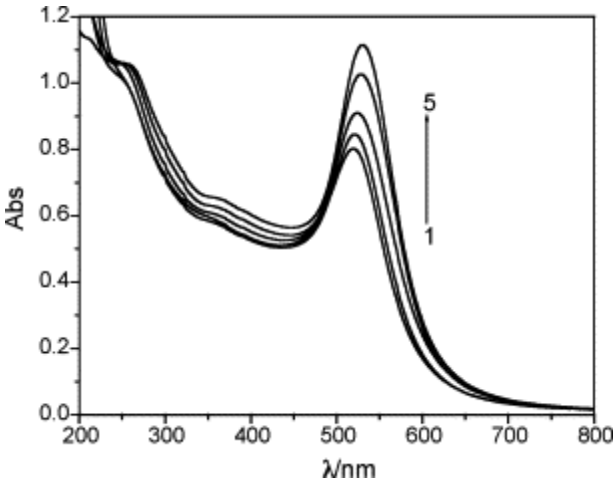

Figure 1.1 Absorbance spectra of spherical Au NPs of different sizes. The diameters are: (1) 12 nm; (2) 19 nm; (3) 24 nm; (4) 33 nm; (5) 41 nm. Reproduced with permission from reference 42, Copyright Elsevier.[42]

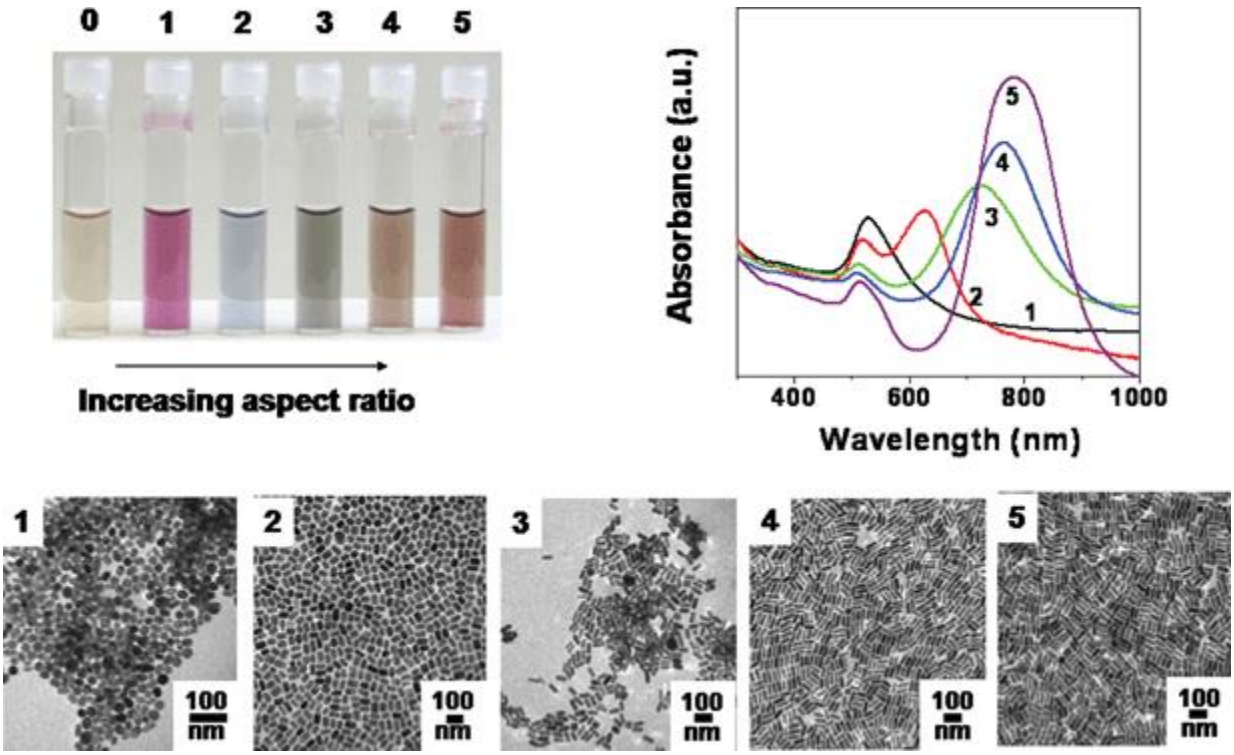

Figure 1.2 Optical characters of Au NPs. (0) 4 nm spherical Au NPs; (1) 25 nm spherical Au NPs; (2-5) Au NRs. Reproduced with permission from reference 46, Copyright Royal Society of Chemistry.[46]

One key characteristic of Au NPs is that the modification is very simple and stable. By modifying the Au NPs with various functional ligands, the Au NP complex could be applied in cancer diagnosis, imaging, cancer biomarker detection, and target-cancer therapy studies. Usually, the surface of Au NPs can be modified in two ways. One is utilizing the thiol group of nonpolar modification reagents to covalently conjugate to the Au NPs, forming strong gold-sulfur bonds (Figure 1.3C). For example, in order to modify the AuNPs with cancer-targeting peptide sequences, the thiol functionalized polyethylene glycol (HS-PEG, MW of 2 kDa) is used to replace the original surface stabilizing molecules, followed by partial replacement with thiol functionalized polyethylene glycol acid (HS-PEG-COOH). This process is similar as shown in Figure 1.3D. Then the interested peptide conjugates to the Au-S-PEG-COOH through peptide bonds.[47] Another modification method is to deposit modification agents by weak interaction forces, such as Van der Waals force and hydrogen bonds (Figure 1.3B). In anti-cancer studies, some special shapes of Au NPs including nanocages, nanostars, and nanoclusters have a large surface area to be modified with plenty of anti-cancer drugs. Thus, the loaded Au NPs could transport the drugs to the tumors.[48]

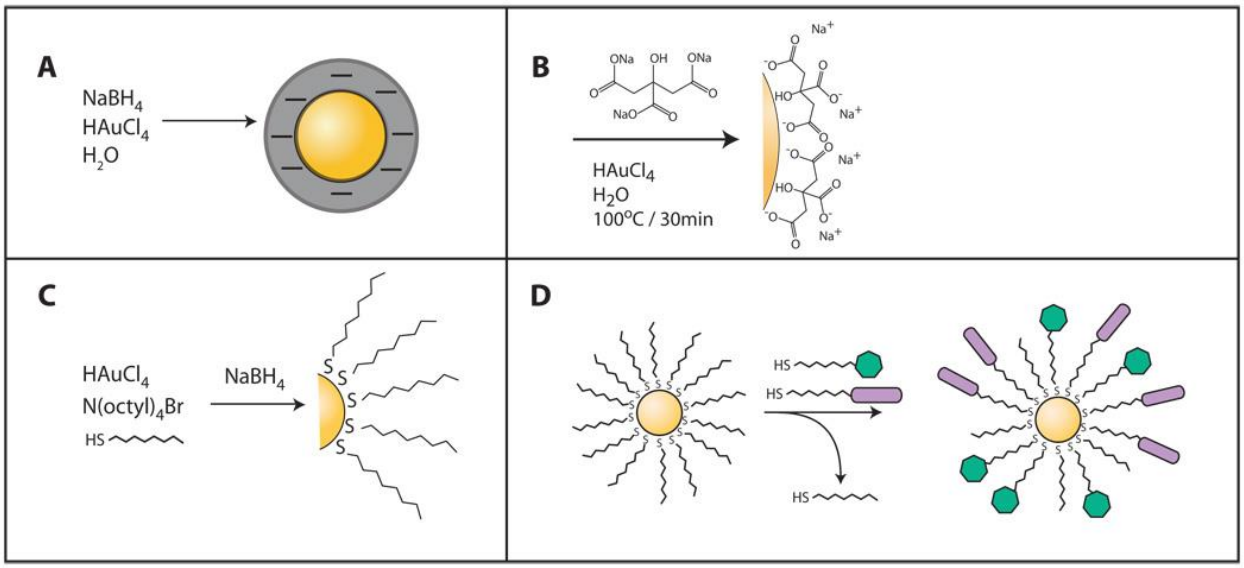

Figure 1.3 Surface modification of AuNPs. Reproduced with permission from reference 49, Copyright Informa.[49]

1.4.2 Magnetic nanoparticles

MNP is a type of NPs that can be influenced by a magnetic field, manifesting as moving towards the stronger magnetic field. The main elements comprising MNPs are usually iron and cobalt.[50] Between them, iron based MNPs, also known as iron oxide nanoparticles (IONPs), are extremely common in cancer diagnosis studies as they enhance the contrast of MRI. Some IONPs have been approved by the FDA (Food and Drug Administration) as clinical MRI contrast agents.[51] For example, metastatic hepatic cancer and lymph nodes can be diagnosed at the early stage by MRI only with those IONPs.[52] Harisinghani *et al.* compared the MRI of lymph nodes with and without a monocrystalline IONP. (Figure 1.4)[53] In the MRI without the IONP, both normal (Figure 1.4 A) and metastatic lymph nodes (Figure 1.4 D)presented as bright white dots, therefore were hard to be distinguished. However, the IONP darkens the healthy lymph node (Figure 1.4 B) while the metastatic lymph node (Figure 1.4 E) was still bright, so that the metastatic lymph node could be diagnosed.

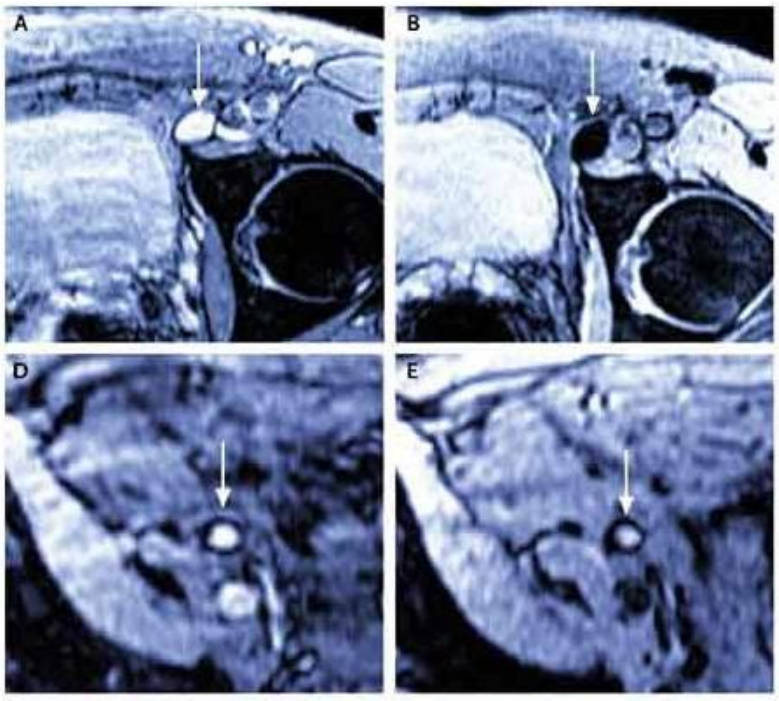

Figure 1.4 Lymph nodes MRI results with and without a monocrystalline iron oxide agent. (A, D) MRI without the agent; (B, E) MRI with the agent. The arrows indicate healthy lymph nodes (A, B), and metastatic lymph nodes (D, E). Reproduced with permission from reference 53, Copyright Massachusetts Medical Society.[53]

Generally, IONPs are synthesized by co-precipitating $FeCl_3$ and $FeCl_2$ in alkaline or acidic aqueous solutions at room temperature.[54-55] The size of IONPs depends on the pH as well as the ratio between ferrous and ferric salts, and is able to be strictly controlled with the presence of citrate.[54-55] Hydrophobic IONPs are also available. Sun et al developed an IONP synthesis method in the oil phase.[56] In this method, the NH-group provider oleylamine is crucial as a surface ligand to stabilize the IONPs in the organic phase. Meanwhile, oleic acid plays an important role to increase the yield of the reaction. The IONPs' size is precisely tunable within 4 to 10 nm and can be further synthesized as MFe_2O_4 (M = Fe, Co, Mn) nanoparticles with comprehensive magnetic properties.[56]

Beyond the application in MRI, MNPs are also popular in biomolecule separation.[57] It is not only because MNPs are controllable by the magnetic field, but also the property of high and stable dispersion in the aqueous phase.[57]

1.4.3 Upconversion nanoparticles

The upconversion nanoparticle (UCNP) is a type of material that uniquely transforms from longer wavelength exciting light to shorter wavelength emitted light. Lanthanide ions, also called rare earth ions, are the most efficient deposit elements in an upconversion illumination system.[58] There are two common mechanisms for UCNPs: excitation and emission happening within a single element called excited state absorption pathway, or excitation and emission happening in two-element atoms called energy-transfer pathway(Figure 1.5).[58] In the excited state absorption pathway, two or more photons at longer wavelengths are absorbed to raise the electron to the excited state. Then, one photon at a shorter wavelength is emitted when the excited electron falls back to the ground state. Three major examples are erbium (Er^{3+}), thulium (Tm^{3+}), and holmium (Ho^{3+}).[58] In the energy-transfer pathway, another element so-called sensitizer, commonly is ytterbium (Yb^{3+}), is also involved in activators' excitation. Briefly, both sensitizer and activator are excited by one photon to an excited state and an intermediate excited state, respectively. Then, the activator at the intermediate excited state is further excited to the fully excited state by the sensitizer's emission photon. According to the unique characteristic of UCNP illumination, the emitted color of the particles is controlled by the combination, or abundance of the rare earth elements (Figure 1.6). Therefore, differently functionalized UCNPs could be distinguished by the different emitting colors in the same condition.

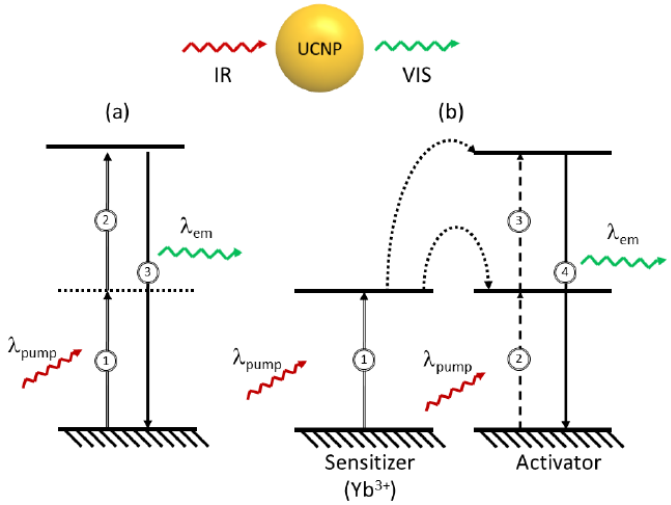

Figure 1.5 Principal mechanisms for upconversion (a) excited state absorption, (b) energy-transfer. Reproduced with permission from reference 58, Copyright MDPI.[58]

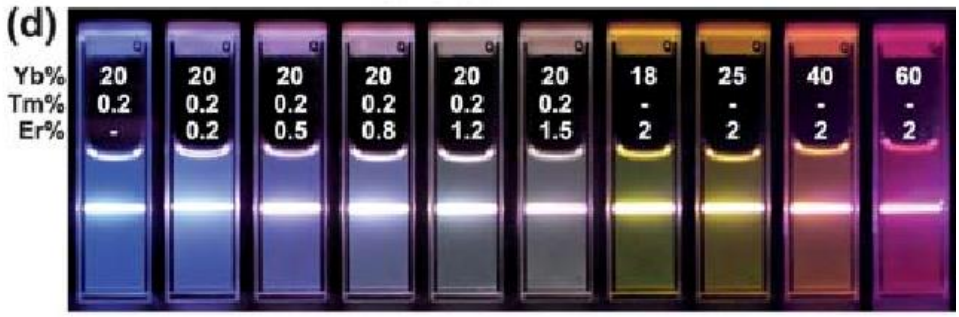

Figure 1.6 NaYF4 nanoparticles with varied lanthanide ion ratios. Reproduced with permission from reference 59, Copyright Society of Public Analysis.[59]

As a promising nanomaterial for *in vivo* imaging, the advantage of UCNPs is that lanthanide doped UCNP could be excited by near-infrared (NIR) light at 980 nm, which can penetrate biological tissues deeper than other wavelengths without increasing photodamage.[60-61] Another advantage of UCNPs for applications in cancer study is that the surface of UCNPs can be modified by various functional ligands at the same particle, including DNA probes, peptide sequences, and

targeting ligands. (Figure 1.7)[62] In summary, the multifunctional UCNP is an ideal candidate for either cancer imaging purposes or a nano-detector for cancer biomarkers.

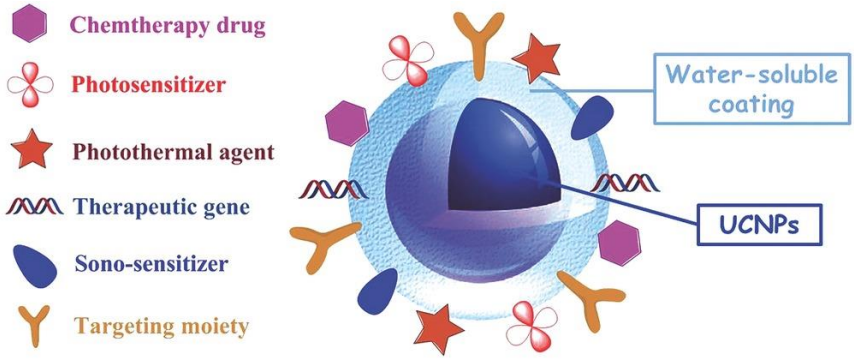

Figure 1.7 Typical architecture of the therapeutic UCNPs-based composite. Reproduced with permission from reference 62, Copyright John Wiley and Sons.[62]

1.4.4 Bacteriophages, bio-nanomaterials

The name of bacteriophage means "bacteria-eater".[63] A bacteriophage, also called a phage, is a type of virus that only infects, replicates, and assemblies in bacterial cells. Phages are composed of a protein capsid and a DNA or RNA genome. In the common life cycle of a phage (Figure 1.8), it first captures the host bacteria cell by the host specific protein fiber at the tip, and then injects its genome that is commonly ssDNA or dsDNA into the bacterial cytoplasm.[63] Integration of the phage genome into the bacterial genome is necessary in the lysogenic cycle, but not in the lytic cycle or the chronic cycle. In the lytic and virulent cycles, the genome and protein capsid assemble in the cytoplasm to form a number of new phages released by lysing the host bacteria. In the case of temperate phages, they assemble in the bacterial membrane and are released without killing the host bacteria.

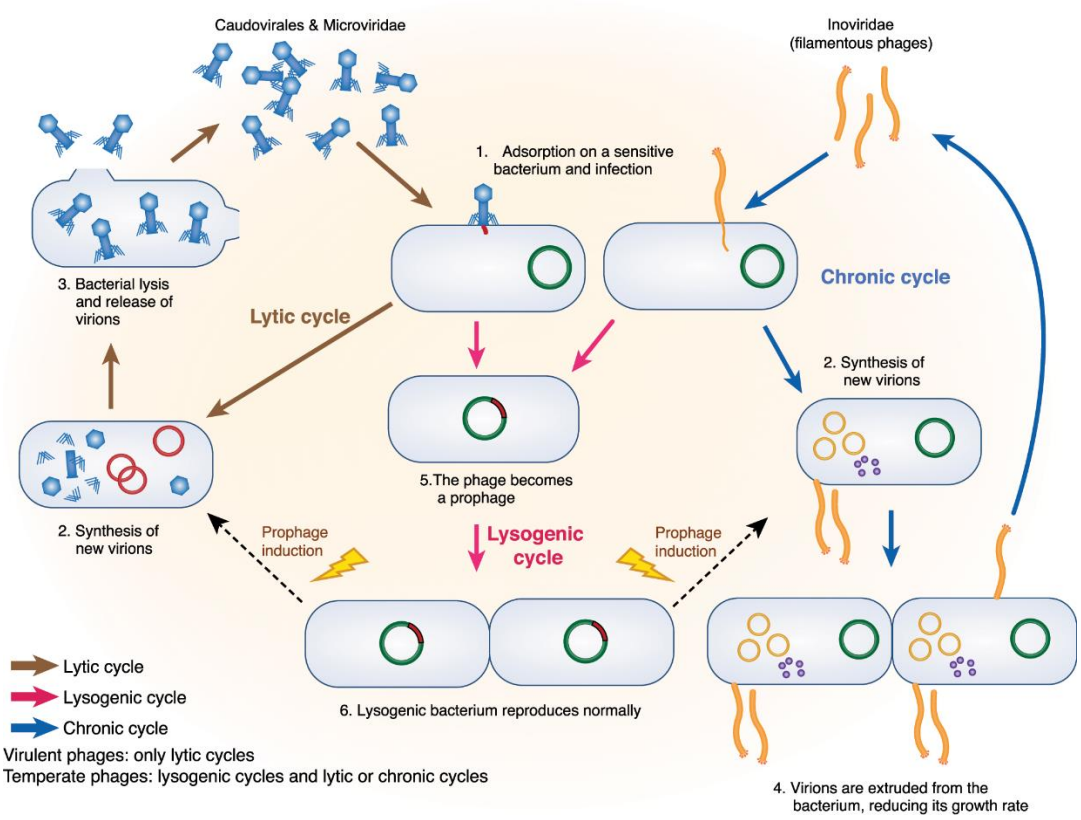

Figure 1.8 Phage life cycle. Reproduced with permission from reference 63, Copyright Creative Commons.[63]

Phages have the following advantages to be applied as nanomaterials in cancer studies: 1. The amplification of phages is rapid and cheap according to their life cycles in bacteria; 2. The genome of phage is simple and well-studied for gene edition and protein engineering; 3. The phages could be applied in clinical therapy since they are harmless for humans.[64] For example, a temperate filamentary M13 phage has a one-segment ssDNA genome encoding five types of coat proteins, including around 2700 copies of the major protein pVIII and 5 copies of four minor coat proteins pIII, pVI, pIX, and pVII (Figure 1.9).[65-67] All the five coat proteins are able to display foreign peptides by genetic engineering. However, the peptide display is commonly applied on pVIII, pIII, and pIX for experimentation due to their relatively bigger sizes.[68] By modifying the

coat proteins of M13 phages with random peptide sequences, the phages could be used for their most significant application, phage display or phage biopanning.[69-72] A phage display library usually contains billions of viral particles displaying different peptides with the diversity of 10^{12}.[73] By incubating the random peptide-displaying phages with the target molecules such as cancer biomarkers or cancer cells followed by washing away the unbound phages, or by circulating them in cancer animal models, the phage displaying peptides with high target-binding affinity is selected.[73] After verified the specificity and affinity, the identified targeting peptides could be used as a targeting agent or further engineered to phage-derived antibodies by using the identified targeting peptides as the antigen binding site in antibodies(Figure 1.10).[73]

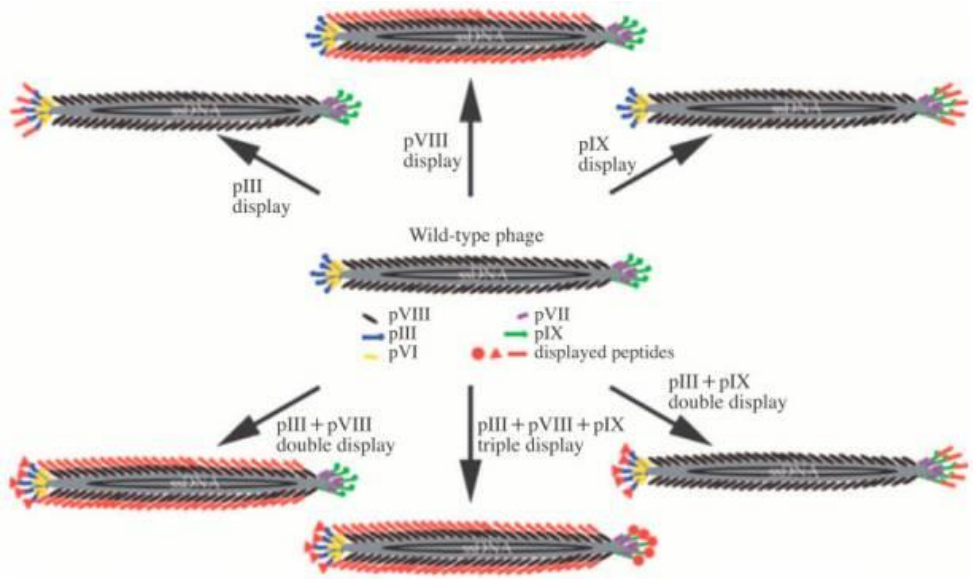

Figure 1.9 Basic structure of the M13 bacteriophage and the possible pathway of genetic engineering. Reproduced with permission from reference 68, Copyright MDPI.[68]

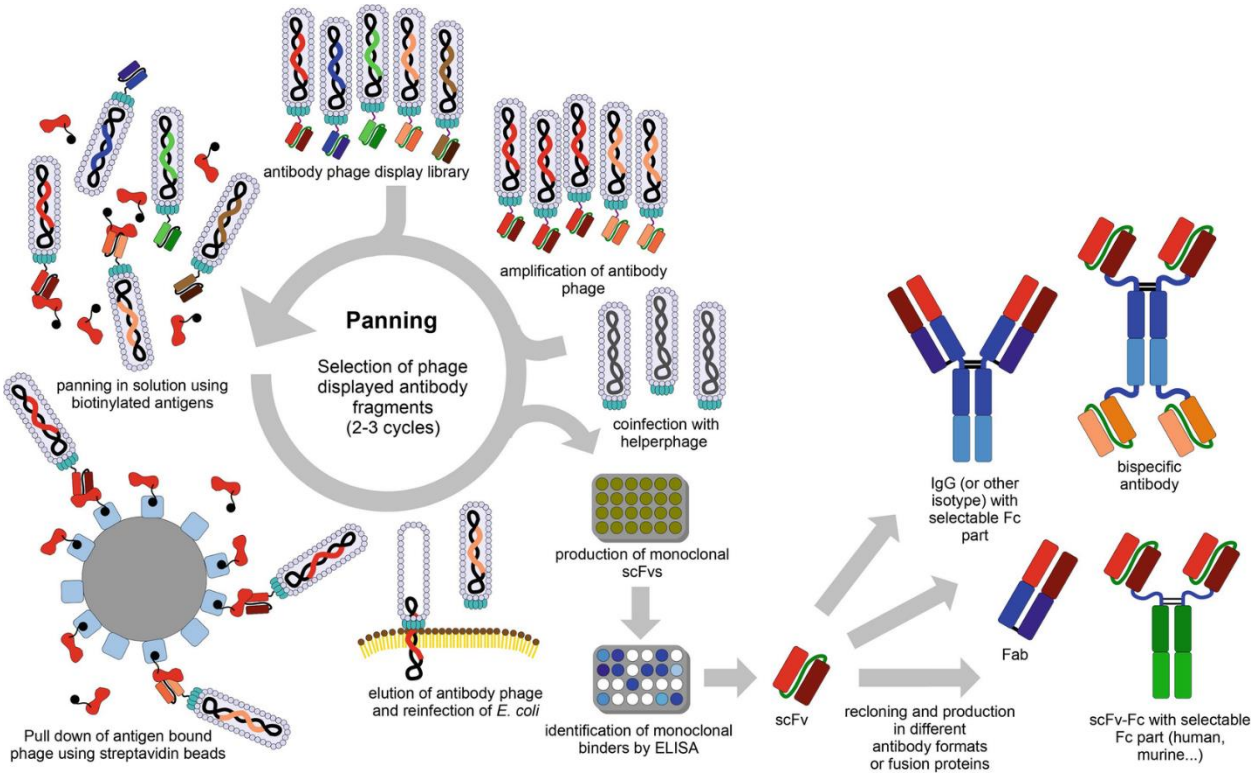

Figure 1.10 Antibody phage display and selection. By incubating the random peptide-displaying phages with the target molecules, the phage displaying peptides with high target-binding affinity is selected. After verified the specificity and affinity, the identified targeting peptides could be further engineered to phage-derived antibodies by using the identified targeting peptides as the antigen binding site in antibodies. Reproduced with permission from reference 73, Copyright Springer Nature.[73]

Chapter 2: Non-invasive cancer imaging methods by using nanoparticles and phages

2.1 Introduction

Clinically, cancer imaging relies on CT, MRI, optical imaging, PET, SPECT, and ultrasound. The discoveries of these imaging techniques have highly benefitted cancer diagnosis but still have limitations. Optical imaging and ultrasound can only present 2D images.[5] CT has an approximating 15% false positive rate.[7] Higher contrast of MRI is desired.[9] PET and SPECT have relatively low resolutions.[10-12] In addition, traditional SPECT for cancer imaging relies on the EPR effect. However, recent researches show that the EPR effect is specific to each cancer type and patient.[74] Besides, the EPR effect is different in mice models compared to that in humans, possibly hindering clinical applications.[74-76]

To improve the contrast of MRI, two types of contrast agents are frequently used in the clinic. Gadolinium (Gd) based paramagnetic small molecules are used to decrease the longitudinal relaxation time (T_1), thus providing contrast. Another is iron oxide based superparamagnetism nanoparticles (IONPs) to reduce transverse relaxation time (T_2).[51] Overall, a shorter T_1 leads to a lighter image and a lower T_2 generates a darker image.[77] Current research starts to pay more attention to iron oxide based contrast agents because Gd based agents can have side effects such as nephrogenic systemic fibrosis.[78] The relatively short circulating time of Gd based agents also limits the application in imaging.[79] Among iron oxide nanoparticles (IONPs), nanoclusters have the potential of better contrast enhancement compared with individual IONPs.[80] It is probably because magnetic iron oxide nanoparticle clusters (MNPCs) have higher magnetic interactions so that the response to an external field is stronger.[80-81]

Previously, most of the MNPCs were made from hydrophobic IONPs that were directly synthesized in the oil phase. The oil phase preparation of magnetic NPs can be very costly and non-scalable, involving the use of several types of pricey precursors and intensive heating.[82-85] On the other hand, in the aqueous phase, the magnetic NPs can be obtained facilely using inexpensive chemicals, i.e. ferric and ferrous chlorides, and yet highly stable and relatively uniform in size.[86-87] Therefore, aqueous prepared IONPs properly transferred into the oil phase can replace the costly hydrophobic IONPs made directly in the oil phase as the starting materials for the synthesis of MNPCs. The key factor that determines the success of this strategy is the quality of the hydrophobic IONPs obtained through aqueous to oil phase transfer. Currently, there no straightforward and productive phase transfer approach that results in high-quality hydrophobic IONPs. Although an oleic acid assisted method was reported previously,[88-89] the hydrophobic IONPs obtained through this method are not individually dispersed, containing a light portion of aggregated nanoparticles that interferes with the formation of MNPCs if not removed.

In the current work, Dr. Penghe Qiu, Dr. Lin Wang, and I developed a simple and straightforward protocol to transfer aqueous IONPs of high concentration into the organic phase and used the hydrophobic IONPs to synthesize MNPCs. In this method, no costly chemicals or heating was involved, making it very cost-effective and simple. The resultant hydrophobic IONPs are highly dispersed and aggregation-free in oil. We also carried out detailed studies over parameters that impact the quality of hydrophobic IONPs. The MNPCs prepared from such hydrophobic IONPs have comparable quality to those made from IONPs directly synthesized in oil. Finally, we attempted to narrow down the size distribution of the MNPCs using a viscosity gradient mediated nanoparticles separation approach. The IONPs larger than 40 nm are classified as SPIO (small particle of iron oxide) agents, and smaller than 40 nm are called USPIO (ultra-

small particle of iron oxide) agents. Because of the differences in size, SPIO and USPIO agents prefer to accumulate in disparate organs and tissues, and hence can benefit cancer imaging of various cancer types. SPIO agents are considered better for reticuloendothelial system imaging, while USPIO agents have longer blood circulating time.[77] In this project, MNPCs that are larger and smaller than 40 nm can both be obtained to be applied as SPIO agents and USPIO agents.

To break the limitation of the EPR effect in SPECT, Dr. Aron Roxin, Andria Hedrick, and I designed a radioactively labeled targeted phage. The phages were displayed with a 15 amino-acids oligopeptide at each copy of pIII coat protein. The peptide was previously selected to specifically target the tumor by *in vivo* phage biopanning against tumor-bearing mice. Then, a chelator, N-hydroxysuccinimide (NHS), was conjugated to the coat proteins of the tumor-targeting phages at the N-terminal by NHS ester reaction. Since the major protein pVIII is present at around 2700 copies, which is over 99% of all coat proteins,[65-67] the most chelators would be conjugated to pVIII and likely leaving the "tumor affinity site" of the pIII proteins un-blocked. The tumor-targeting phages were radioactively labeled with ^{99m}Tc through the chelator. With the help of tumor-targeting peptides, the radioactive phages were theoretically able to enhance the signal accumulation in the tumor sites compared to typical SPECT imaging results. In this study, we used human breast cancer MCF-7 xenograft models for f3-15mer phage library biopanning. The tumor-targeting peptide sequence, AREYGTRFSLIGGYR, was identified in the previous studies accomplished by Dr. Xuewei Qu.[47]

2.2 Materials and methods of magnetic nanoparticle clusters

2.2.1 Preparation of iron oxide nanoparticles[54]

To synthesize iron oxide nanoparticles, 4.0 ml of 1.0 M aqueous ferric chloride and 1.0 ml of 2.0 M ferrous chloride were mixed with 40 ml of 0.7 M ammonia solution with vigorous stirring.

The stirring was continued for about 5 min, and then the product was centrifuged at 3,000 rpm for 10 min. The pellet was redispersed into 10 ml of 2 M nitric acid for 1 h and the nanoparticles were harvested by centrifugation at 3,000 rpm for 10 min, and subsequently resuspended into 10 ml of water. To prepare a TEM sample, 2 µl of the as-prepared aqueous IONPs solution was added on a TEM grid. The grid was set for 2 min and dried with filter paper. All the TEM images in this dissertation were characterized by Zeiss 10 TEM. The size distribution of all the NPs in this project was measured by a dynamic light scattering (DLS) instrument.

2.2.2 Phase transfer of the as-prepared iron oxide nanoparticles from aqueous into oil

In a typical phase transfer, 0.5 ml of 40 mM sodium citrate and 3.0 ml of 0.5 M oleylamine in hexane were added subsequently to 2.5 ml of the as-prepared aqueous IONPs solution, and the mixture was sonicated intensively for 2 min. Then 3.0 ml of ethanol was added and mixed by vigorous handshaking. Phase transfer of iron oxide nanoparticles from water to hexane could be visualized after the solution was incubated at room temperature for a few hours. The nanoparticles in hexane were extracted with a separation funnel, washed twice with ethanol, and redispersed into hexane at the desired concentration. To prepare a TEM sample, 2 µl of the as-prepared hexane-dispersed IONPs solution was added on a TEM grid and air-dried. The zeta potential was measured by a zeta potential analyzer.

2.2.3 Preparation of iron oxide nanoparticles clusters

To prepare MNPCs, 200 µl of the above hexane-dispersed iron oxide nanoparticles were mixed with 4.0 ml of 0.1 M aqueous CTAB (cetrimonium bromide) solution, followed by sonication to form a stable oil in water dispersion. The solution was then heated in an 80 ^{o}C water bath for 15 min under stirring, during which iron oxide nanoparticles inside the oil-in-water micelles self-assembled, as a result of hexane evaporation, to form MNPCs.

2.2.4 Preparation of silica coated MNPCs

The as-prepared iron oxide MNPCs (1 ml) were centrifuged once and redispersed into 4 ml of 0.02 M CTAB aqueous solution. Then, 50 µl of 28% ammonium hydroxide and 20 µl of tetraethyl orthosilicate were introduced subsequently to the MNPCs solution. Silica coated MNPCs were obtained by stirring the above mixture solution under room temperature for 24 h. To prepare a TEM sample, 2 µl of the MNPCs with or without silica coat was added to TEM grids. The grids were set for 2 min and dried with filter paper.

2.2.5 Size sorting of MNPCs by PVP viscosity gradient medium

The viscosity gradient medium was created by stacking subsequent polyvinylpyrrolidone (PVP) solutions of decreasing concentrations into a 15 ml centrifuge tube. To enhance the stability of MNPCs in the centrifuge medium, in all the PVP solutions, the polymer was dissolved into 0.1 M CTAB solution, instead of pure water. Specifically, 3 ml of 40 wt% PVP was loaded first to the bottom of the centrifuge tube by a Pasteur pipette, followed by 1.5 ml of 35, 30, 25, and 20 wt% PVP solutions successively. On top of the PVP medium, 200 µl of MNPCs solution, concentrated by centrifugation from 1.0 ml of the as-prepared MNPCs, was carefully loaded. The MNPCs were immediately centrifuged in a swing-bucket rotor, for a total of 2.5 h at 4300 rpm. The centrifuge was interrupted every 30 min to take photos. Finally, a small amount of sample was extracted with a syringe and needle at different levels inside the PVP medium. The effectiveness of size sorting by the PVP viscosity gradient medium was then evaluated by TEM.

2.3 Materials and methods of targeted SPECT

2.3.1 M13 phage modification with the chelator NHS-MAG_3

Methods to modify the targeted peptide displayed M13 phages or wild-type phages with a chelator NHS-MAG_3 (NHS-mercaptuacetyltriglycine) were referred to previously published

work.[90] The chelator NHS-MAG_3 underwent an NHS ester reaction to become covalently attached to available primary amines on the phage. 500 µl of M13 phages was mixed with NHS-MAG_3at a molar ratio of 2750: 1 (phage: chelator). The pH was subsequently adjusted to be in the range of 8 to 10 by addition of 15 µl of 0.1 M sodium bicarbonate. The mixture was rotated overnight at room temperature and the phage was purified using PEG (polyethylene glycol)/NaCl precipitation twice. The modified M13 phages were resuspended in 500 µl of water for the following use.

2.3.2 Radiation labeling with ^{99m}Tc (Technetium-99m)

The radiation labeling of the modified M13 phages followed previously published work.[90] The radioactive substance ^{99m}Tc interacts with MAG_3 and forms a stable complex. Briefly, 8.5 µg of $SnCl_2 \cdot 2H_2O$ was dissolved in 2 µL of degassed 10 mM HCl and was mixed with a sixth of the final volume of 50 mg/mL tartrate buffer, 500 µl of the modified phages, and approximating 5 mCi of TcO_4. The mixture was placed at room temperature for 1 h after which phage was purified using PEG/NaCl precipitation twice. TLC was carried out after each purification to verify the efficiency of the purification and the radioactive label. Ideally, the free radioactive substance should be less than 10 % of overall radioactivity and the overall radioactivity should be more than 100 µCi. The radioactively labeled phages were resuspended in normal saline for the following experiment. The volume of the normal saline was decided by the radioactivity to make approximating half a million counts per minute (CPMs) per µL.

2.3.3 Animal experiment for SPECT

The animal protocol 17-068-SSCHIR-H was approved by IACUC. Two groups of 3 female nude mice in each were used in this study. Estradiol pellets were implanted subcutaneously when mice were 5 weeks old, and two days after which approximating 3×10^6 of MCF-7 was implanted in mice *in situ*. When the diameters of the tumors were larger than 5 mm, approximating 200 µL

of the as prepared radioactive labeled targeted M13 phage or wildtype M13 phage was tail intravenous (*i.v.*) injected in the target group and wild-type group respectively. The radioactivities of the injected substances were recorded by a Gamma Counter instrument. SPECT images were taken at 30 min, 1 h, 2h, 4 h, 6h, and 24 h respectively after the injection.

To investigate the distribution, two mice from each group were sacrificed at 4 h and one mouse from each group was sacrificed at 24 h after the injection. Blood, bladder, bone, brain, heart, intestine, kidney, liver, lung, muscles, salivary, spleen, stomach, thymus, and tumor were weighed, and their radioactivities were counted by a Gamma Counter instrument.

2.4 Results of magnetic nanoparticle clusters

2.4.1 Phase transfer of IONPs and Characteristics of hydrophobic IONPs

The aqueous IONPs were synthesized simply by following previously published work.[54] The IONPs made by this approach are very stable that can stay in water for years without forming any visible sedimentation. In addition, the preparation can be easily scaled up to a few liters in a lab since it is conducted in the open air under room temperature. Therefore, we used these hydrophilic IONPs as the starting material in our protocol. In a typical phase transfer of the IONPs from aqueous to oil, partial phase separation could be observed shortly after sonication, while complete extraction of IONPs into the hexane phase took place immediately upon introduction of 3 ml of ethanol (Figure 2.1a). The IONPs in the oil phase readily showed ferrofluidic behavior in the presence of an external magnet (Figure 2.2), which is an indication that such phase transfer can be done at very high IONPs concentration.[91] In practice, nanoparticles can form aggregates easily during the transfer from one phase to another. The Transmission Electron Microscopy (TEM) images and the hydrodynamic size distribution of IONPs before and after the phase transfer showed that by our method the IONPs successfully remained as individually-dispersed and

aggregation-free nanoparticles in the oil phase (Figure 2.1b to e). The IONPs transferred by the current method are highly stable in a number of organic solvents, such as chloroform, hexane, cyclohexane, and toluene. They retained as individual dispersion even after 5 times of repeated precipitation (by ethanol) and resuspension (by oil) cycles.

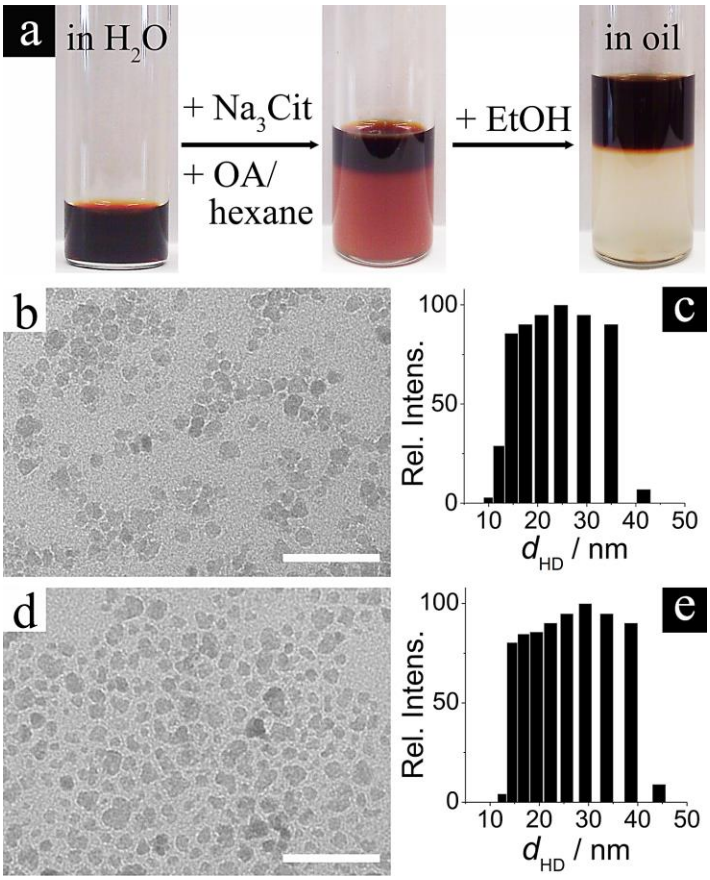

Figure 2.1 Phase transfer of the as-prepared aqueous iron oxide nanoparticles into oil. (a) A brief illustration of the phase transfer process; (b to e) TEM images and the corresponding hydrodynamic size distribution of iron oxide nanoparticles before (b, c) and after (d, e) the phase transfer. Scale bar: 50 nm.

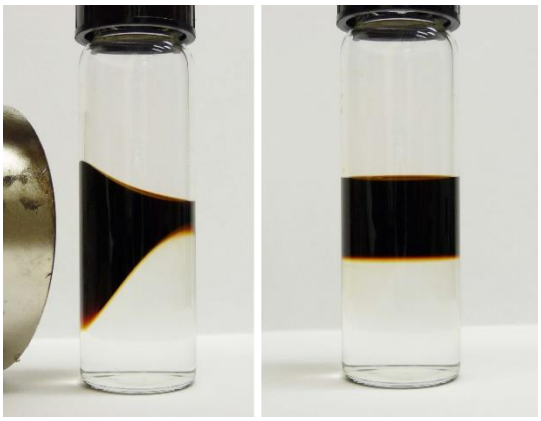

Figure 2.2 Photographs of IONPs transferred from water to hexane by using sodium citrate as the polyanion species. The bottom layer is the aqueous layer and the upper layer is the organic layer. Left: ferrofluidic behavior of IONPs in hexane in the presence of an external magnet; Right: No IONPs were attracted to the sidewall of the container after sitting by the magnet for 10 min, suggesting high stability and aggregation-free of IONPs in hexane.

Sodium citrate is a critical reagent in the successful phase transfer of the as-prepared IONPs. Without it, the IONPs refused to enter into the oil phase and remained at the interface. To examine the role of sodium citrate and the structure of ligands on the surface of IONPs in oil, we carried out the same phase transfer procedures but replaced sodium citrate with other types of carboxylate/carboxyl based anion species, including sodium acetate, sodium carbonate, ascorbic acid and polyacrylic acid (PAA). The effectiveness of the phase transfer with these reagents was then evaluated by measuring the average particle size by DLS. A broad range of concentrations was tested to ensure that the best performance of each type of the anions has been tested. The size distribution of IONPs transferred into oil by each anion type at four typical concentrations is shown in Table 2.2. This reveals that the concentration of the anion species did have an impact on the effectiveness of the phase transfer. For singly-charged anion species, namely sodium acetate and sodium carbonate, the lowest possible particles size in the oil phase was 86.3 and 38.4 nm

respectively. However, both of them are far larger than the hydrodynamic size of IONPs shown in Figure 2.1d, which is around 24 nm, suggesting that single carboxylate anions cannot effectively contribute to the phase transfer of IONPs. As a matter of fact, for most samples obtained from these two reagents, a large portion of the IONPs in oil were attracted by a magnet to the sidewall of the container, and aggregated (Figure 2.3). On the other hand, in the presence of reagents containing polyanion groups, i.e. sodium citrate, ascorbic acid, and polyacrylic acid, the average size of IONPs after phase transfer can reach very close to 24 nm. Thus, polyanion molecules are indispensable in transferring the IONPs from water to oil.

Table 2.1 DLS measurement of the average size of nanoparticles after being transferred into oil by different anion species.

Anion Species	Conc. (mM)	Avg. size of NPs in oil (nm)*
Sodium Acetate	20.0	ND**
	26.7	179.4
	33.3	86.3
	40.0	204.8
Sodium Carbonate	5.0	195.7
	10.0	51.9
	20.0	38.4
	33.3	220.2
Sodium Citrate	1.3	35.4
	3.9	24.1
	12.9	24.5
	25.9	24.7
Ascorbic Acid	0.5	117.9
	1.3	30.5
	2.6	30.8
	26.3	25.2
Polyacrylic Acid ***	22.0	195.6
	44.0	55.3
	73.3	32.9
	110.0	26.6

* After phase transfer, all the samples were washed once with ethanol and resuspended into hexane for DLS measurement.

** ND means non-dispersible in hexane.

*** Molecular weight: 1.8 K. Concentration was calculated based on the repeating unit.

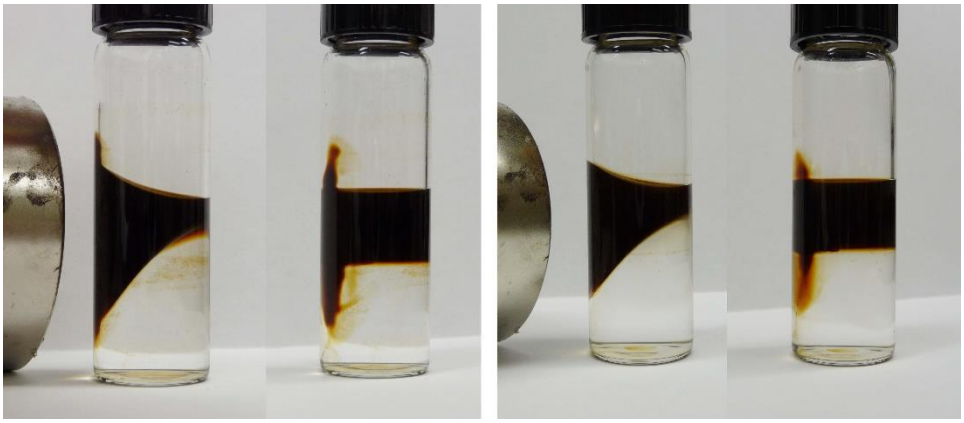

Figure 2.3 Phase transfer of IONPs conducted by using sodium acetate (left, 33.3 mM in Table 2.2) and sodium carbonate (right, 20.0 mM in Table 2.2) as the anionic molecules. Aggregates of IONPs on the sidewall after removal of the magnet suggest partial nanoparticles' aggregation during the phase transfer process. Thus, single anion species, namely sodium acetate and sodium carbonate, are not as effective as polyanion species, namely sodium citrate, in assisting the phase transfer of IONPs.

Based on the above observation, we proposed the structure of ligands on the surface of the IONPs, which is depicted in Scheme 2.1. The polyanion species can cap the IONPs once they are added into the nanoparticle solution, which was indicated by a surface charge reversal of the IONPs. The as-prepared IONPs have a zeta potential value of +25.2 mV, but it became negative upon the introduction of the polyanion species (exact values are in the range of -21.4 mV to -54.1 mV depending on the type and the concentration of the polyanion species). These poly-anion molecules can also provide additional negatively charged groups to interact with the amine groups of oleyamine so as to form a second robust coating around the IONPs, which enabled the nanoparticles to be successfully transferred into the oil phase. For single anion species, although they can effectively coat the IONPs, due to the lack of additional groups for interaction with amines, they are not efficient reagents for the phase transfer. In addition, it seems feasible that oleic acid

alone can replace the functions of both the polyanion species and oleylamine to achieve phase transfer by the mechanism described above. However, in practice, oleic acid cannot induce the phase transfer at all, the IONPs remained in the aqueous phase in the presence of oleic acid. As a result, poly-anion molecules are necessary for phase transfer by interacting with both IONPs and oleylamine (Figure 2.4).

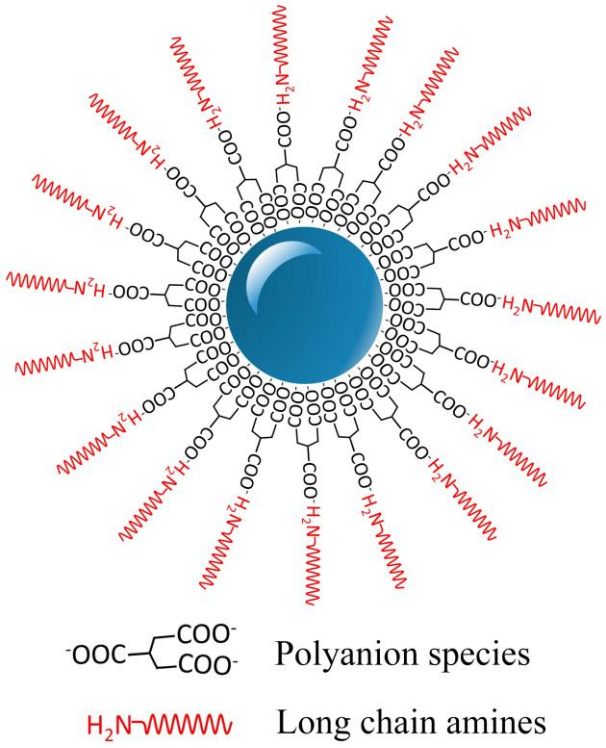

Scheme 2.1 Proposed ligand structure on the surface of iron oxide nanoparticles after being transferred from aqueous to the oil phase.

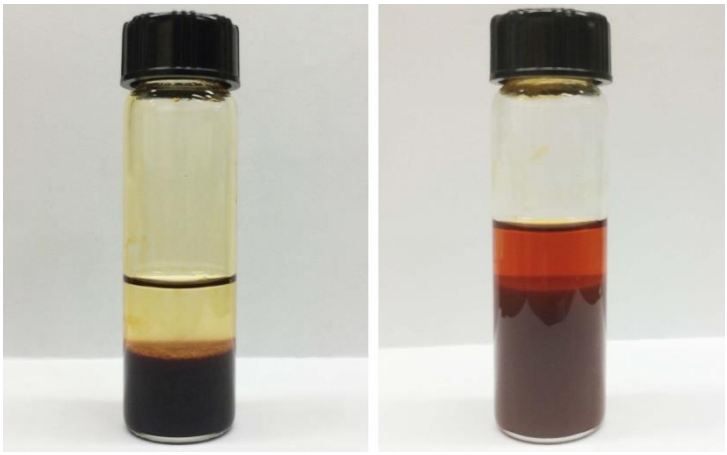

Figure 2.4 Phase transfer of IONPs using oleic acid as the hydrophobic capping molecules. No polyanionic molecules were used here. Left: upon sonicating the mixture solution of oleic acid/hexane and as-prepared aqueous IONPs for 2 min; Right: after addition of ethanol. The majority of the IONPs remained in the water/ethanol phase, suggesting the ineffectiveness of oleic acid as the capping reagent for the phase transfer of IONPs.

2.4.2 Synthesis of MNPCs

We then proceeded to make MNPCs with the hydrophobic IONPs obtained from the optimized phase transfer. The preparation was conducted through a well-known oil phase evaporation-induced self-assembly of hydrophobic nanoparticles in an oil-in-water emulsion.[92] Cetyltrimethylammonium bromide (CTAB, 0.1 M) was used as the surfactant to form the emulsion. A 32 mg/ml hexane dispersion of IONPs (sodium citrate was used as the polyanion species for phase transfer) was employed to ensure that the MNPCs will be produced at a high yield. The formation of the MNPCs was confirmed by the TEM images shown in Figures 2.5a and b. These MNPCs have a typical 3D spherical structure, which is very similar to those made from hydrophobic IONPs synthesized directly under high temperature in the oil phase. The as-prepared MNPCs have a wide size distribution. A statistical study of DLS showed that the particle size

ranges continuously from 20 to 100 nm (Figure 2.5c). TEM images of typical MNPCs of around 40, 60, and 80 nm are shown in Figure 2.5d to f. In each of these MNPCs, the individual IONPs were densely packed, despite the fact that the as-prepared IONPs in aqueous are not uniform in either size or shape. This confirms that IONPs made in this manner can perform as well as the originally hydrophobic nanoparticles in terms of forming MNPCs. To make sure that the clustering in TEM images was caused during the sample preparation rather than by the gathering of micelles during the TEM sample preparation, we coated directly the as-prepared MNPCs a thin silica shell. The core/shell nanoparticles show clearly that the MNPCs were individually dispersed in the solution phase (Figure 2.5g and h). Besides, we measured the magnetization curves of both individual and clustered IONPs. The MNPCs synthesized by our protocol presented the same superparamagnetic characters and fairly highly-saturated magnetization as the individual IONPs (Figure 2.6). Therefore, the MNPCs has the potential to be applied as a contrast agent in MRI.

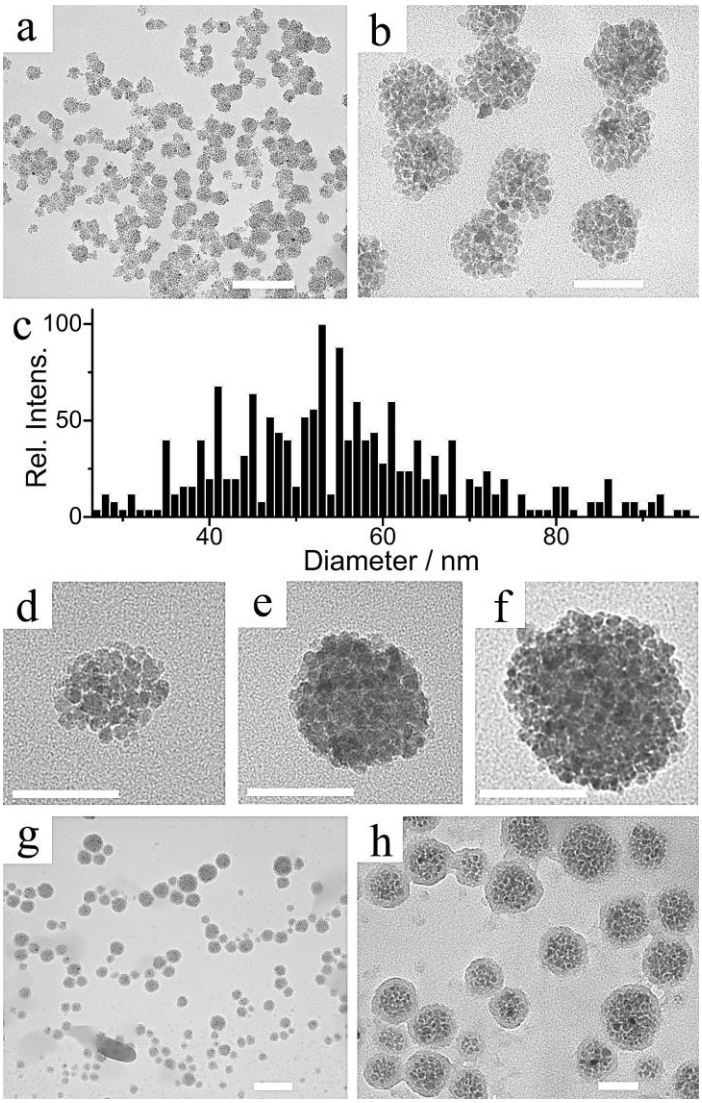

Figure 2.5 Iron oxide MNPCs prepared by using hydrophobic nanoparticles obtained through phase transfer. (a, b) Low and high magnification TEM images of as-prepared MNPCs; (c) Plot of the size distribution of the as-prepared MNPCs; (d-f) TEM images of a typical MNPC of around 40, 60, and 80 nm; (g, h) Silica coated MNPCs. Scale bars: 200 nm (a, g); 50 nm (b, d to f, h).

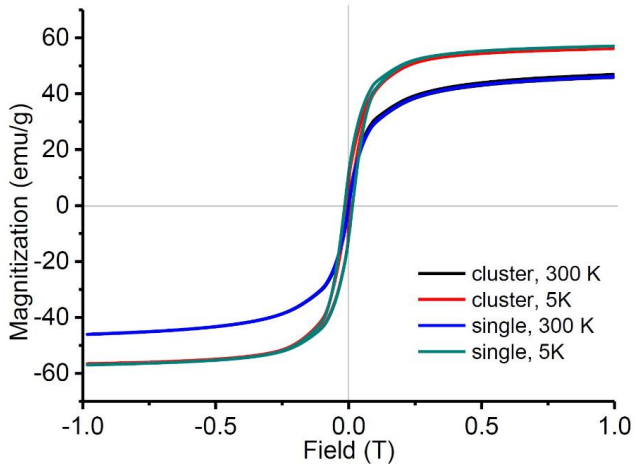

Figure 2.6 Magnetization curves of single and clustered IONPs at 5 and 300 K. Similar curves between the single IONPs and the MNPCs proved strong magnetization of MNPCs and indicated the MNPCs could be applied in MRI.

In addition to using sodium citrate as the polyanion species, we also tried to make MNPCs with IONPs obtained from two other types of polyanion species, namely ascorbic acid and PAA. MNPCs similar to those shown in Figure 2.5 can be produced from hydrophobic IONPs assisted by ascorbic acid. However, only non-dispersible aggregates were generated with the PAA assisted hydrophobic IONPs. We think this is likely the result of incomplete anchoring of the polymer chains to the surface of IONPs. In other words, the individual PAA chains were only partially anchored to the IONPs, while the rest of the chains were extended into the solvent. Such a ligand configuration would lead to the formation of an incomplete hydrophobic shell during the aqueous to oil phase transfer process, which would further cause massive aggregation of IONPs once they were introduced back into water to form the oil-in-water emulsion. Due to these reasons, although highly water-dispersible PAA coated small IONPs have been prepared by different methods,[93-94] they are not suitable for making MNPCs through the selective oil phase evaporation approach.

2.4.3 Size distribution of MNPCs

Previously, the Mao's lab has reported that nanoparticles of nonuniform size distribution can be sorted effectively through centrifugation in a PVP-based viscosity gradient.[95] Here, we also attempt to narrow down the size distribution of the MNPCs prepared in this work in a medium of gradient viscosity. The medium was created by layering aqueous PVP solutions of 40, 35, 30, 25, and 20 wt% in a 15 ml centrifuge tube (Figure 2.7a). Photographs taken at 30 min intervals show that the PVP-based viscosity gradient medium could effectively differentiate the settling velocity of MNPCs of different sizes. After 2.5 h of centrifugation, the MNPCs formed a continuous distribution throughout the medium based on the size ranges. TEM examination of samples taken from different PVP density fractions confirmed that MNPCs were well separated by the viscosity gradient medium and that the particles at the same depth inside the centrifuge tube were indeed quite uniform in size (Figure 2.7b to d).

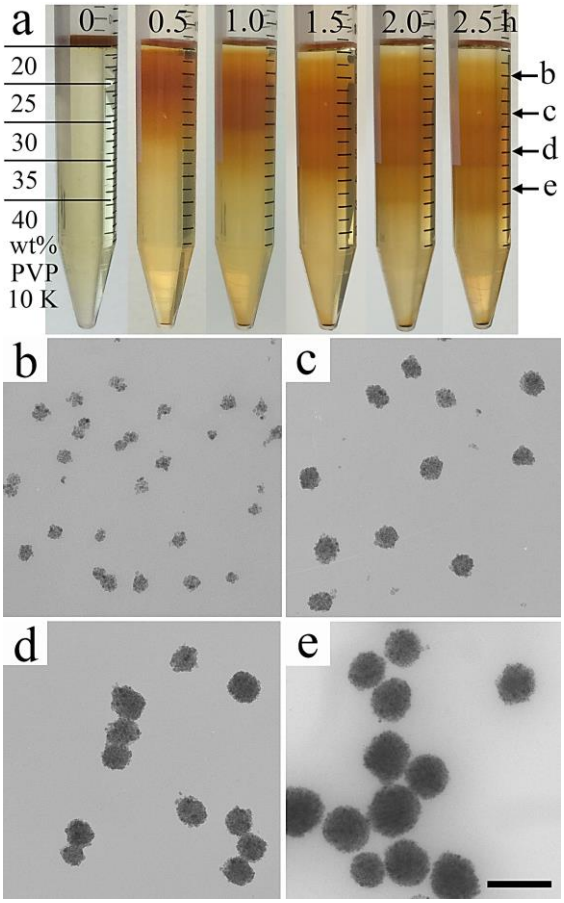

Figure 2.7 Size sorting of MNPCs through centrifugation in a PVP based viscosity gradient medium. (a) Leftmost, composition of the viscosity gradient medium. All the PVP solutions contain 0.1 M CTAB. Photographs, taken at 30 min intervals, showing the sedimentation of NPCs in the medium during centrifuge. (b to e) TEM images of NPCs sampled at different levels inside the centrifuge tube indicated by arrows in a. Scale bar: 200 nm.

In conclusion, we developed a straightforward and productive phase transfer approach to make MNPCs based on the reported aqueous IONPs that were prepared by a simple, scalable, and cost-effective method. We found that small polyanionic molecules are important for the successful transfer of IONPs from the aqueous to the oil phase. The hydrophobic IONPs made by our phase transfer method were highly stable in the organic phase even after repeated washes. They could

form MNPCs comparable to those prepared by using originally hydrophobic IONPs in terms of shape and packing density of NPs. In contrast to the conventional method of making MNPCs, our current method does not involve any sophisticated experimental setups nor costly precursor chemicals. Thus, it significantly reduces the efforts and cost needed for the preparation of MNPCs.

2.5 Results of targeted SPECT

Radioactively labeled M13 phages with or without targeted peptide displayed were injected in mice having breast cancer tumors. The mice were imaged at 30 min, 1 h, 4 h, and 6 h respectively after the injection. (Figure 2.8) The image for 2 h time point was excluded from the result due to the bad quality. The mouse from the targeting group died between the 6 h and 24 h time points, which precluded imaging beyond 6 h. At 30 min (Figure 2.8a), the tumor of the targeting group was visualized by the radioactive signal, while the one of the wild-type group was not visible until 4 h after the injection (Figure 2.8a to c). This indicates the radioactively labeled targeting phages were able to enhance the radioactive signal accumulation in the tumor sites faster than the radioactively labeled wild-type phages. Additionally, the overall signal of the targeting group is visually lower than the wild-type group after 1 h (Figure 2.8b to e), likely because the targeting phages have stronger interactions with vascular endothelial cells than the wild-type phages so that the targeting phages have a higher metabolic rate. The biodistribution also presented the same case. (Figure 2.9 and 2.10) The percent injected dose for the targeting group is generally lower than the wild-type group at both 4 h and 24 h after the injection. The remaining % injected dose in the mouse is 76.4 % for the targeting group and 88.9 % for the wild-type group at 4 h. At 24 h, it is 54.5 % and 65.6 % respectively.

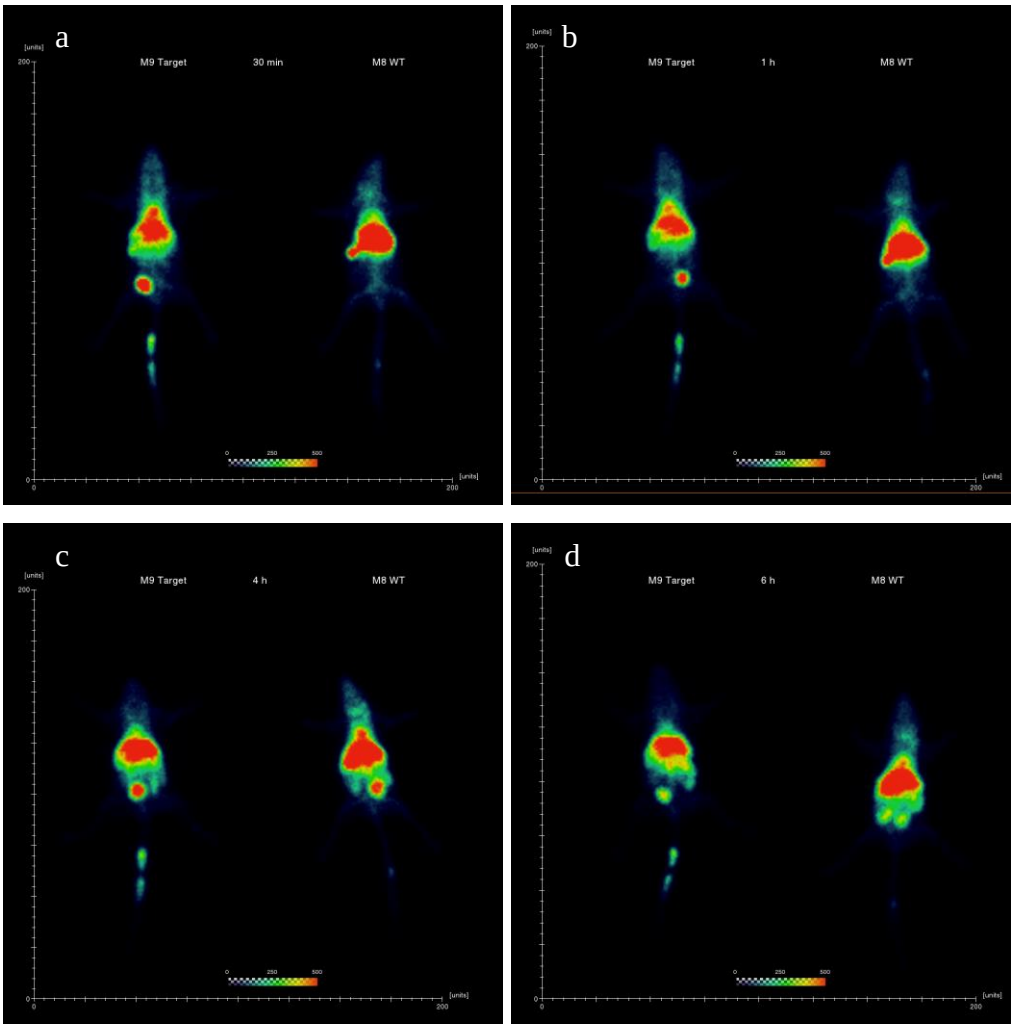

Figure 2.8 SPECT for human breast cancer MCF-7 xenograft model. The images were taken at 30 min (a), 1 h (b), 4 h (c), and 6 h (d) respectively after the injection. In each one, the left mouse was injected with the radioactively labeled targeting phages and the right one was injected with the radioactively labeled wild-type group. The breast tumor was implanted in the fat pad on the right side of the mice (left side in the image). The mice sometimes turned over during imaging such as the left mouse in b.

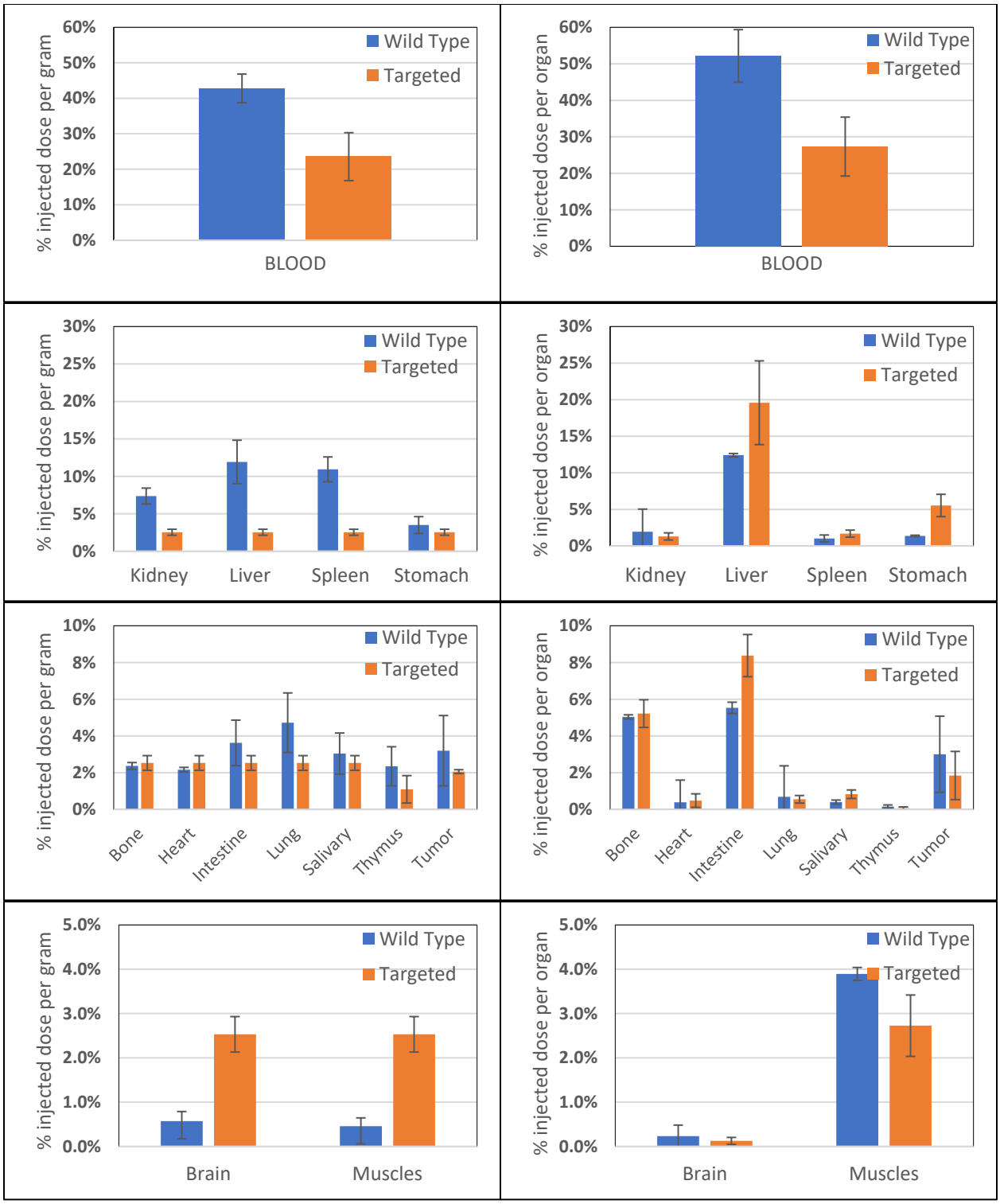

Figure 2.9 Biodistribution at 4 h after injection. The percent injected dose per gram equals to radioactivity per gram of the organ corrected for time decay divided by the total radioactivity injected into the animal; the percent injected dose per organ equals to total radioactivity in organ

corrected for time decay divided by the total radioactivity injected into the animal. The radioactivity was recorded from two mice for each group; error bars therefore represent the range for each of these two values.

Although the biodistribution at 4 hours shows the wild-type group has higher average radioactivity in the tumor, considered the few objects (only two mice in each group) and the large standard bars, there was no significant difference between the two groups. With the imaging results (figure 2.8), it is clear that the radioactively labeled targeting phages accumulated in the tumor in a shorter time while metabolized more quickly compared with the radioactively labeled wild-type phages. At 4 h post injection, the tumor imaging quality seemed to be similar between the two groups, and at 24 h, most radioactive substance ^{99m}Tc decayed and did not work for imaging anymore.

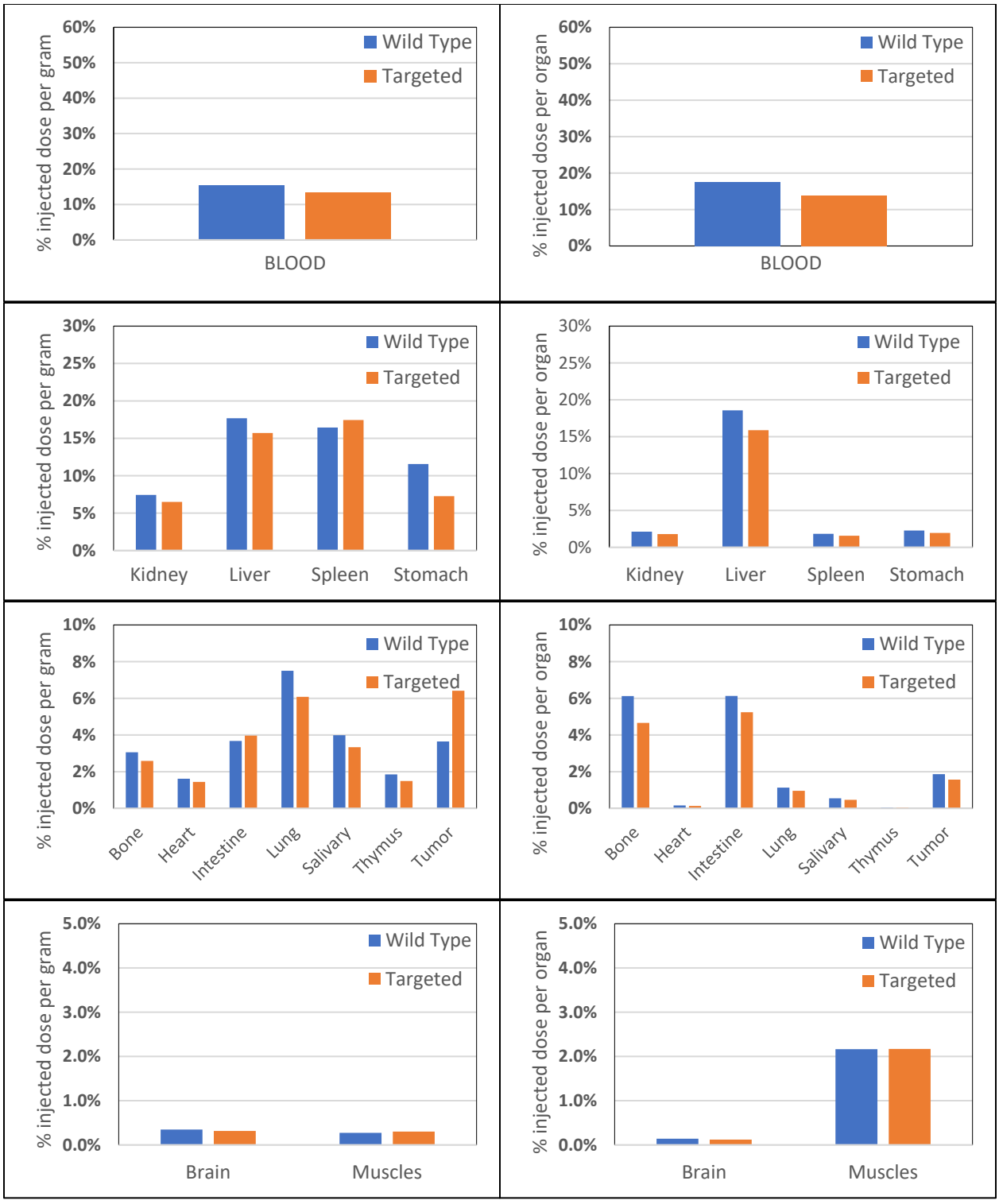

Figure 2.10 Biodistribution at 24 h after injection. The percent injected dose per gram equals to radioactivity per gram of the organ corrected for time decay divided by the total radioactivity injected into the animal; the percent injected dose per organ equals to total radioactivity in organ

corrected for time decay divided by the total radioactivity injected into the animal. The radioactivity was recorded from the mice in Figure 2.9.

In summary, we developed a radioactively labeled targeting phage for breast cancer SPECT. With this targeting phage, the breast tumor could be imaged earlier (within 30 min after the injection) than using the radioactively labeled wild-type phages. However, the analysis of the biodistribution was only carried out for the 4 h and 24 h time points post the injection, while in hindsight the 4 h time point would be desirable. In addition, a larger number of experimental subjects in each group should be used to limit the uncertainty and account for the possibility of premature death of the subjects. Besides, another group with free ^{99m}Tc should be investigated to compare with typical SPECT.

2.6 Conclusion and discussion

Overall, we designed a method of MNPC synthesis as well as a radioactively labeled targeted phage. These have the potential to benefit the MRI and the SPECT imaging methods, respectively. However, further investigations are needed for both studies.

The MNPCs we synthesized are simple, scalable, and cost-effective, but we have not evaluated them in MRI applications. The proton transverse relaxivity with an extra magnetic field should be analyzed because it is a key factor to enhance the contrast in the MRI. Moreover, MRI with and without the MNPCs by using animal tumor models would provide visual evidence of its potential to be a contrast agent.

The SPECT imaging strategy with radiolabeled phage is an advanced alternative strategy for the traditional *in vivo* fluorescent imaging to evaluate the tumor affinity of the candidate peptide of *in vivo* phage biopanning against a tumor model. SPECT is also the first time to be used for this

typical purpose. In most studies, the regular imaging strategy for this purpose is to compare the fluorescent accumulation by *in vivo* fluorescent imaging which has two major limitations: 1. The background or noise is usually high since the image represents the overall fluorescence of the whole body. 2. The resolution of *in vivo* fluorescent images is low and the fluorescent accumulation is unable to quantify or semi-quantify. However, by imaging the animals with radiolabeled phage candidates and SPCET imaging system, then precisely quantifying the organs by a Gamma Counter instrument, we are able to evaluate the tumor affinity clearly as well as the biodistribution of the phages. In sum, SPECT imaging of tumor models directly using the radiolabeled phage candidate is a powerful strategy for phage-derived anti-cancer antibody screening research.

Chapter 3: Small RNA quantification methods by using nanoparticles

3.1 Introduction

Small non-coding RNA (sncRNA) is a type of RNA that does not encode proteins and is less than 200 nucleotides (nts).[27] sncRNA is crucial for multiple biological processes due to its gene regulation functions. For example, micro RNA (miRNA) hybridizes to mRNAs to down-regulating gene expression;[96] Piwi-interacting RNA (piRNA) silences genes by suppressing transposon activity to ensure genetic fidelity.[97] Therefore, the abnormal expression level of small ncRNAs is related to diverse diseases, such as cardiovascular diseases and cancer.[98-105] Accurate quantification of the small ncRNAs can not only benefit our understanding of the mechanism for these diseases, but also improve the precision of clinical diagnosis and prognosis.[25, 99, 104, 106-108]

Despite there are several common detection methods for RNA, such as qRT-PCR and cDNA microarray, these methods are difficult to be applied to small ncRNA especially when the sequence length is as short as 20 nts/bps. Such a small size makes small RNA unsuitable for cDNA synthesis that is required for both qRT-PCR and cDNA microarray.[109-110]

Therefore, Dr. Aron Roxin, Dr. Yan Zeng, and I attempted to develop a small RNA quantification method by recruiting pyropheophorbide-a (pyro) and magnetic beads. (Scheme 3.1) In this method, miR21, which is associated with multiple cancer types,[25-26] was used as a target RNA. Magnetic beads are able to capture pyro only when the target miR-21 is present in the sample, and the concentration of miR-21 can be quantified by analyzing the concentration-dependent signal of the captured pyro. Pyro is a fluorescent molecule (excitation: 410 nm, emission: 675) and can produce singlet oxygen with 680 nm excitation. Because it can produce singlet oxygen, it is frequently used for tumor photodynamic therapy and photodynamic

diagnostics.[111] This small RNA quantification method is the first time to recruit pyro to RNA quantification. We hypothesized the concentration of singlet oxygen and pyro are linear dependent so that the singlet oxygen signal would be concentration dependent on the captured pyro. Meanwhile, the singlet oxygen production efficiency of pyro positively correlates to the laser power. We expected that the quantification based on the singlet oxygen would reduce the limit of detection by amplifying the signal. The concentration of singlet oxygen can be quantified by a commercial reagent called Singlet Oxygen Sensor Green (SOSG). The fluorescent signal arising from the interaction of singlet oxygen and SOSG is linear with respect to singlet oxygen concentration.

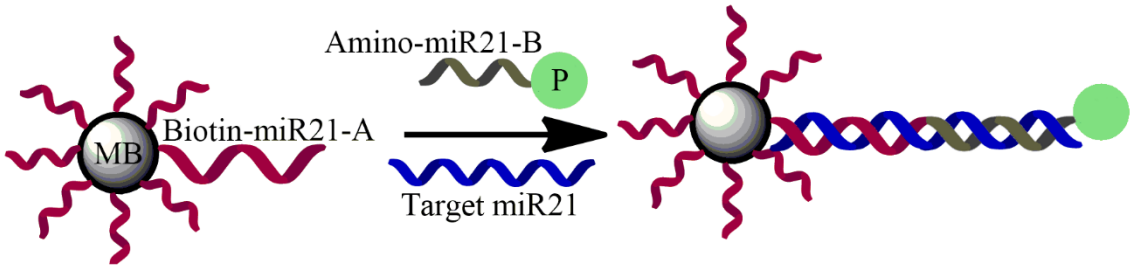

Scheme 3.1 Structure of miR21-A probe/miR21/miR21-B probe complex. "MB" presents streptavidin modified magnetic beads. "P" presents pyro. The biotin modified miR21-A probes and the amino modified miR21-B probes are respectively partial complementary to the target, miR-21. The biotin modified miR21-A probes are conjugated to the streptavidin modified magnetic beads as probe A labeled magnetic beads. The amino modified miR21-B probes are conjugated to the pyro as pyro labeled probe B. As a result, the magnetic beads are able to capture pyro when the target miR-21 exists. Uncompleted pyro can be separated from the captured pyro by a magnet. The fluorescence of the captured pyro would be measure and represents the amount of the target miR-21. Furthermore, 680 nm laser treatment, pyro would produce singlet oxygen which can be detected by SOSG (ex: 485 nm, em: 528 nm).

Another available method for small RNA detection is to use molecular beacon (MB), a DNA based probe having a hairpin structure. This hairpin probe is used to position a quencher and a fluorophore in proximity. The fluorescence signal can only be detected when the probe is hybridized with its target. This strategy does not require reverse-transcription of the target small RNAs. Aside from nucleic acid detection, MBs are also meaningful for disease monitoring, the study of protein-DNA interaction, and other applications.[112]

However, traditional MBs mainly use fluorescent molecules as fluorophores, which has several limitations. First of all, many cells and tissues have an autofluorescence that causes relatively high background,[113-114] requiring RNA purification before detection. This is undesirable because it leads to unavoidable RNA loss.[115-116] In addition, fluorescent molecules can be photobleached,[117-118] impacting fluorescent signal intensity stability that reduces the reliability of detection and quantification. Although there are several methods to solve this issue, such as minimizing light exposure and creating a photobleach curve, it would be easier if we can find something stable to replace the fluorescent molecules.

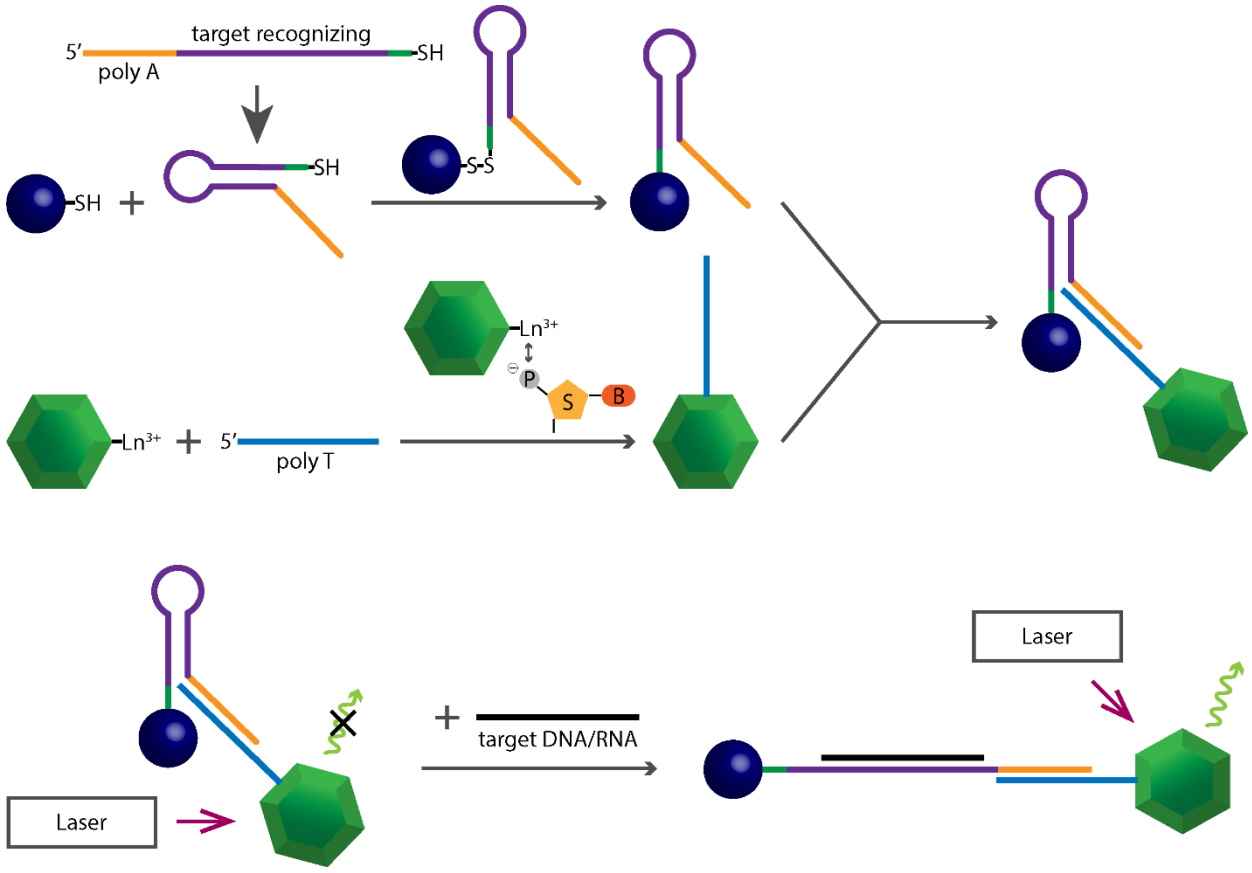

Scheme 3.2 Scheme of NPMB (nanoparticle based molecular beacon). A thiol modified hairpin DNA probe contains three regions: a poly A region, a target recognizing region, and a 3' thiol end. The thiol group modified at the 3' end of the hairpin DNA probe and conjugates to a Au NP (dark blue sphere) that serves as a quencher of the UCNPs (green hexagon). There are several extra nucleotides between the target recognizing region and the thiol group, to protect the target recognizing DNA from potential damage in the conjugation process of DNA and Au NPs. UCNP bind with a poly T DNA oligo by lanthanide ion and phosphate group interaction, and the poly T tract is hybridized to the poly A tract on Au NPs. Thus, the DNA modified Au NP and the DNA modified UCNP are assembled. The hairpin structure of the target recognizing region can unwind and hybridize with the target RNA. UCNP is quenched by Au NP without the target RNA; when

the target presents, the hairpin DNA probe hybridizes with the target and the UCNP fluorescence will be detected.

In this study, Dr. Penghe Qiu and I present a novel nanoparticle-based MB (NPMB) for small RNA detection using upconversion nanoparticles (UCNPs) as fluorophores, and gold nanoparticles (Au NPs) as quenchers. (Scheme 3.2) NPMB is a promising small RNA detection candidate for the following two reasons. First, the NPMBs are able to detect and quantify small RNAs without purification. Unlike fluorescent molecules, the exciting wavelength of UCNPs is longer than the emitting wavelength.[119] Due to this unique optical property, this detection method has an ultra-low background and can detect RNAs in a complex environment such as plasma, serum, and urine samples. Second, UCNPs are stable and can be stored at room temperature for years without being protected from light. To evaluate the NPMBs small RNA detection strategy, miR-21 and DNA-mi21 were employed as example targets. The nucleic acid sequences involved in this project are listed in Table 3.1. This novel NPMB can detect both small DNA and RNA as low as aM level, even in plasma. The linear detection ranges from 1 aM to 100 fM for DNA and 10 aM to 1 pM for RNA.

Table 3.1 Probe and target sequences of NPMB

DNA on UCNPs	TTTTTTTTTTTTTTTTTTTT
DNA on Au NPs for NPMB	AAAAAAAAAAAAAGTTGTATCGAATAGTCTGACTACA ACTGGG-Thiol
Target DNA (DNA-mi21)	TAGCTTATCAGACTGATGTTGA
Target RNA (miR-21)	UAGCUUAUCAGACUGAUGUUGA

3.2 Materials and method of pyro and magnetic beads based small RNA quantification

3.2.1 Pyro synthesis[120]

Pyro was synthesized by following previously published work. 673 mg of Chlorin e6 trimethyl ester was dissolved in 25 ml of collidine and then heated to 50°C under vacuum. Potassium tert-butoxide in THF (tetrahydrofuran) was added dropwise over 10 min until the color changed from dark green to dark orange. The mixture was moved to room temperature and stirring at 350 rpm for 2h in the dark. Then 27 ml of degassed acetic acid was added to the mixture dropwise over 10 min while stirring at 350 rpm. The solvents were removed under vacuum sequentially at different temperatures: THF at 20°C, Acetic acid at 70-90°C, and collidine at 95-130°C. The crude was again dissolved in 38ml collidine, stirred at 350 rpm, degassed under vacuum, and heated to 185-191°C for 5 hours. Finally, after the removal of collidine, the product was placed in nitrogen gas, stored in the dark at -20°C.

3.2.2 Pyro labeled probe B

Amino modified miR21-B probe was bound to pyro following a reported method.[121] For each detection sample, the following components are mixed successively in a foil-covered tube: 20 μL of 5 mM pyro in DMF (N,N-Dimethylformamide), 5 μL of 20 mM TBTU [N,N,N′,N′-tetramethyl-O-(benzotriazol-1-yl)uronium tetrafluoroborate] in DMF, 20 μL of 100 μM amino modified miR21-B probe, and 42.5 μL of water. 1 μL of N,N-diisopropylethylamine (DIPEA) was added and mixed. The samples were rotated overnight at room temperature. To purify the pyro labeled probes, the samples were washed with ethyl ether twice; the aqueous phase contained the pyro labeled probes, and the organic phase contained the extra pyro.

3.2.3 Probe A labeled magnetic bead

For each detection sample, 100 μg of streptavidin magnetic bead was washed with PBS three times and resuspended in 100 μL of TE buffer. 15 μL of 100 μM biotin modified miR21-A probe or desthiobiotin modified miR21-A probe was added. The samples were shaken for 30 min at room temperature. The free probe would be separated from the captured probe by a magnet. Each sample was resuspended in 100 μL of water.

3.2.4 Detection sample preparation

For each detection sample, the probe A labeled magnetic bead, pyro labeled probe B, and gradient concentration of the target miR-21 were added. Water was added to fill 500 μL. The samples were rotated for 1 h at room temperature. Then, the samples were washed with water and resuspended in 150 μL of water. 150 μL of methanol and 3 μL of SOSG was added. The fluorescence intensities of pyro (ex: 410 nm, em: 675 nm) were recorded before 680 nm laser treatments, and the fluorescence intensities of SOSG (ex: 485 nm, em: 528 nm) were recorded before and after 680 nm laser treatments. The fluorescence was measured by a plate reader.

3.3 Materials and method of NPMBs based small RNA quantification

3.3.1 Synthesis of Au NPs

Au NP seeds were synthesized by following a reported method.[41] 600 μL of 0.06 M HAuCl4 was mixed with 45 mL of H_2O under heating and stirring. After the temperature got 95 ℃, 7 mL of 40 mM sodium citrate was added. About 10 min later, the color of the solution changed from light yellow to light red, and then became dark red. The Au NP seeds were suspended in the solution.

To synthesize Au NPs with 540 nm absorption, we referred to a polyvinylpyrrolidone (PVP) coating method on Au NPs.[41] By adjusting the concentration of Au NP seeds and PVP, we

developed the Au NPs absorbing at 540 nm. Specifically, 200 μL of 5× concentrated Au NP seeds in EtOH with 1% PVP was stirred overnight. The 5× Au NPs solution was mixed with 4 mL of dimethylformamide with 10% PVP and 40 μL of 60 mM $HAuCl_4$ under vigorous stirring. 20 μL of 78.8mM sodium ascorbic was added twice with a gap of 15 min. About 1 hour later, the Au NPs were suspended in the solution.

To make the TEM sample, 2 μL of the Au NP sample was loaded on the TEM grid. The grid was dried with filter paper after 2 min. The absorption spectrum of Au NPs was measured by Implen NanoPhotometer.

3.3.2 DNA coating of Au NPs

The AuNPs were modified with the DNA probe, "DNA on Au NPs", by following report work.[122] The Au NPs were washed with EtOH three times and with water twice. The Au NPs were resuspended in 4.5 mL of H_2O. 34 μL of 100 μM DNA on Au NPs and 1 μL of 10 mM TCEP was mixed and incubated at room temperature for 1 hour. The Au NPs in 4.5 mL of H_2O and the incubated DNA solution was mixed under stirring overnight. The unbound DNA was removed by centrifugation. The DNA modified Au NPs were resuspended in 4.5 mL of H_2O. To make the TEM sample, 2 μL of the DNA modified Au NPs were loaded on the TEM grid. The grid was dried with filter paper after 2 min.

3.3.3 Synthesis of UCNPs with green emitting light

UCNPs were synthesized by following a reported method.[119] 2 mmol of $YCl_3 \cdot 6H_2O$, 0.45 mmol of $YbCl_3 \cdot 6H_2O$, and 0.05 mmol of $ErCl_3 \cdot 6H_2O$ were dissolved in 13.75 mL oleic acid and 11.25 mL 1-octadecene under stirring and vacuuming at 110 ℃. 10 mmol of NaF was dissolved in 13.75 mL oleic acid and 11.25 mL 1-octadecene under stirring and vacuuming 110 ℃. After dissolving, the above two solutions were mixed and vacuumed for 30 min under stirring at 110 ℃.

The reaction system was flushed with N_2 for 20 min and was heated in an oil bath (300℃) under the protection of N_2 for 30 min. When the solution cooled down, EtOH with the same volume was added to it and was centrifuged for 20 min at 3000 RPM. Later, 10 mL hexane was mixed with the sediment and then kept stand for 10 min. After repeating adding EtOH and centrifuging, the UCNPs were kept in 4 mL chloroform for the following use. To make the TEM sample, 2 μL of 10-time diluted UCNP sample was directly loaded on the TEM grid. To quantify the concentration of UCNP solution, 1 mL of the undiluted sample was dried in a 1.5 mL centrifuge tube. The weight of the centrifuge tube was measured with and without the dried sample. All the emission spectra of UCNPs including NPMB were measure by an Agilent Cary Eclipse Fluorescence Spectrophotometer.

3.3.4 DNA coating of UCNPs

Based on the published DNA coating method of UCNPs,[119] we enrolled IGEPAL® CO-520 to modify UCNPs with DNA. 10 mL of cyclohexane with 5 mg of UCNPs was mixed with 500 μL of IGEPAL® CO-520 under sonication for 15 min. The mixture was mixed with 40 μL of 1 nM DNA on UCNPs under vigorous stirring overnight. 10 mL of EtOH was added to wash the DNA coated UCNPs. The DNA coated UCNPs were further washed with EtOH twice and with water once. The DNA modified UCNPs were resuspended in 1 mL of H_2O. To make the TEM sample, 2 μL of the 10-time diluted DNA modified UCNPs were loaded on the TEM grid. The grid was dried with filter paper after 2 min.

3.3.5 Synthesis of NPMBs and the control group

1 mL of DNA modified Au NPs and 200 μL of DNA modified UCNPs were mixed under stirring for 1 hour. The NPMBs or the control group were centrifuged and resuspended in 1 mL of

H_2O. To make the TEM sample, 2 μL of the NPMB sample or the control group was loaded on the TEM grid. The grid was dried with filter paper after 2 min.

3.3.6 Detection of the target DNA and RNA

The NPMBs were centrifuged and resuspended in 1 mL of H_2O or 1 ml of spiked plasma, respectively. The spiked plasma was made by the removal of endogenous target RNAs by magnetic beads from a commercial plasma. Gradient concentrations of 1 μL of target DNA or miR-21 were mixed with 199 μL of NPMBs under stirring for 1 hour. The emission spectrum was detected by a spectrometer and analyzed by Origin® 8.6. A 980 nm laser was used as the excitation light and the excitation of 400 nm to 600 nm was recorded.

3.4 Results of pyro and magnetic beads based small RNA quantification

3.4.1 Characterization of pyro and selection of laser treatment

Streptavidin can specifically bind to both biotin and desthiobiotin with similar binding affinities.[123] However, the binding between desthiobiotin and streptavidin is published as more readily reversible.[124] To examine if using biotin or desthiobiotin would impact our assay, both biotin modified miR21-A probe and desthiobiotin modified miR21-A probe were conjugated to streptavidin modified magnetic beads, referred to probe A (Biotin) labeled magnetic beads or probe A (DTB) labeled magnetic beads respectively. Excess miR-21 and pyro labeled probe B were mixed with probe A (Biotin) labeled magnetic beads and probe A (DTB) labeled magnetic beads separately. The fluorescence signals of pyro and SOSG were recorded in Figure 3.1. There was no significant difference between desthiobiotin and biotin. Considering the price, we chose to use biotin for the following research.

Different doses of 680 nm laser treatment were tried (Figure 3.1 b) to select the laser treatment with the best singlet oxygen generation efficiency. The result presented the fluorescence

intensity of SOSG was higher under 680 nm laser treatment with stronger power. The fluorescence increase per Joule was highest under 0.5-1 J. As a result, we would use 25 mW of 680 nm laser to treat each sample for 20 s to make 0.5 J.

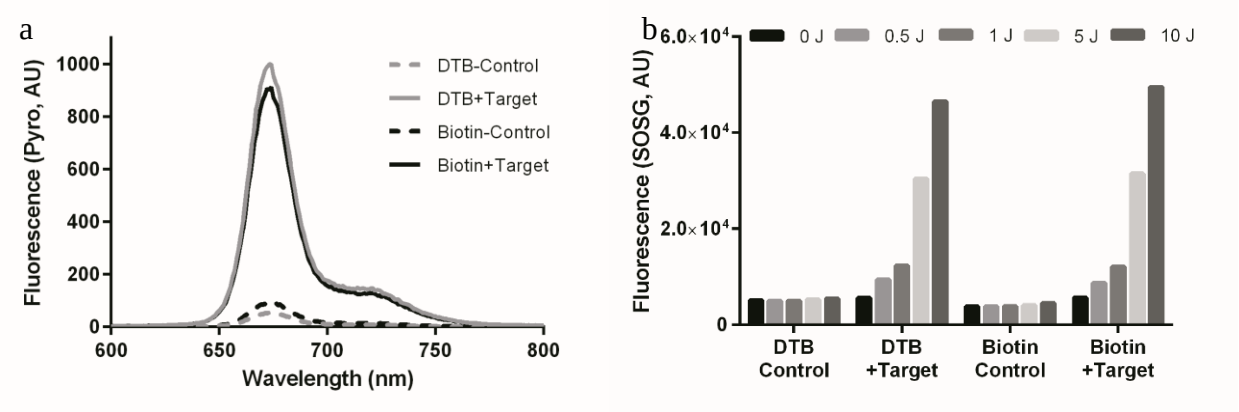

Figure 3.1 Fluorescence of pyro (a) and SOSG (b). The biotin modified miR21-A probe (Biotin) and the desthiobiotin modified miR21-A probe (DTB) were both tried to verify the conjugation efficiency. Excess miR-21 was added for target groups; there was no miR-21 for the control groups. There was no significant difference between using biotin or desthiobiotin since the fluorescence signals are similar of DTB+Target and Biotin+Target. The fluorescence increase per Joule was highest under 0.5-1 J.

3.4.2 Determination of detection range

To estimate the detection range, the fluorescence of pyro in the absence of any conjugation was measured, resulting in a limit of detection (LOD) for pyro was about 100 fM. LOD was calculated by following a reported equation: LOD = 3Sa/b, where Sa presents the standard deviation, and b is the slope of the trend line.[125] As a result, quantification of the target miR-21 was tested within concentrations between 100 fM to 10 μM. Subsequently, we detected the fluorescence of SOSG with different concentrations of pyro from 100 fM to 1 μM. The linear

detection range of singlet oxygen by SOSG was 10 pM to 1 μM. Although the detection range based on the singlet oxygen signal is higher than the detection based on the fluorescence signal, the linearity of singlet oxygen signal is better since the R square value of singlet oxygen is closer to 1 compared with the one of fluorescence of pyro (Figure 3.2). Further studies are needed to determine if the LOD based on the singlet oxygen signal with fluorescent SOSG readout can be improved by laser treatment with stronger power.

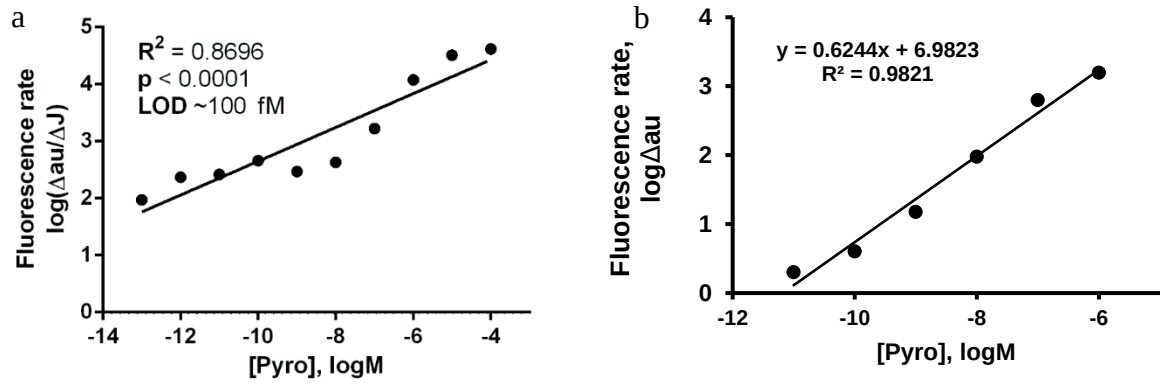

Figure 3.2 Fluorescence of pyro (a) and the fluorescence change of SOSG (b) with different concentrations of pyro. a: The p value lower than 0.01 indicated the relationship between the fluorescence and the concentration of pyro is a linear regression even though the R square value was lower than 0.9. b: the singlet oxygen signal was proved to be linear dependent on the concentration of pyro.

3.4.3 Target miR-21 quantification

To verify the quantification efficiency of this pyro and magnetic beads based system, we measured the fluorescent signal of pyro and SOSG with different concentrations of the target miR-21(Figure 3.3). Based on the detection results of pyro's fluorescence, (Figure 3.3 a) the logarithm of fluorescence intensity showed a linear correlation with the logarithm of the target concentration when the target miR-21 ranges from 2 pM to 20 nM. However, when referring to the signal based

on singlet oxygen, (Figure 3.3 b) the fluorescence signals have no significant change among variable target concentrations. Furthermore, pure magnetic beads (MB in Figure 3.3 b) triggered the fluorescence of SOSG, which indicates magnetic beads may be able to generate singlet oxygen with 680 nm laser treatment because SOSG was reported to be highly selective for singlet oxygen. This phenomenon has not been reported before. Further research is required to verify this discovery.

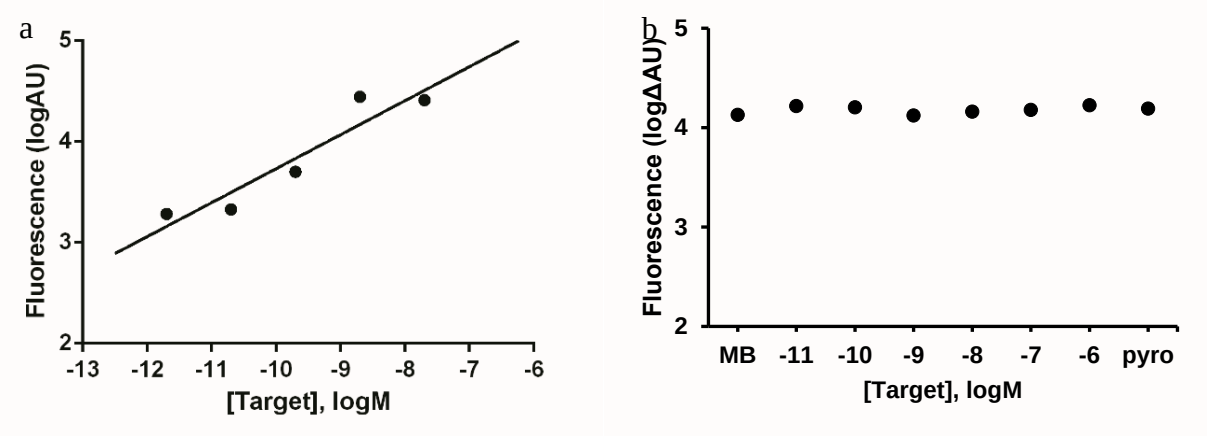

Figure 3.3 Fluorescence of pyro (a) and the fluorescence change of SOSG (b) with different target miR-21 concentrations. a: The linear quantification range of miR-21 based on the fluorescence of pyro is 2 pM to 20 nM. b: MB means there is no pyro or target miR-21 in the system and is used as a negative control. Pyro indicates there is only pyro and SOSG in the solution and is a positive control. There was no significant difference among groups with different miR-21 concentrations because of the background signal from magnetic beads that was as strong as the signal in the positive control.

In summary, we attempted to develop a small RNA quantification method by utilizing pyro and magnetic beads. In this method, we would like to take the advantage of pyro that its fluorescent signal and singlet oxygen producing ability are both in proportion to the concentration. Meanwhile,

we used magnetic beads for separation and purification. We did achieve linear detection based on the fluorescence of pyro and the detection range is from 2 pM to 20 nM. However, because of the significant background of magnetic beads, we could not detect the target RNA based on the singlet oxygen signal. We found magnetic beads might have the ability to generate singlet oxygen as well, but further verifications are needed.

3.5 Results of NPMB based small RNA quantification

3.5.1 Characterization of UCNPs, Au NPs, and DNA modified NPs

Figure 3.4 presents the TEM image and the emission spectrum of the as-prepared UCNPs. The TEM image of UCNPs (Fig. 3.4a) shows that hexagonal UCNPs has a uniform size of 30 nm in diameter without obvious aggregation. The emission spectrum of UCNPs (Fig. 3.4b) was determined after excitation with a 980 nm laser. The spectrum indicates two emission areas of UCNPs, a weak peak from 400 nm to 415 nm, and two major peaks from 510 nm to 570 nm. The highest emission is at 541 nm. To assure a measurable quench-release fluorescence change, the 510 nm to 570 nm area was selected for detection.

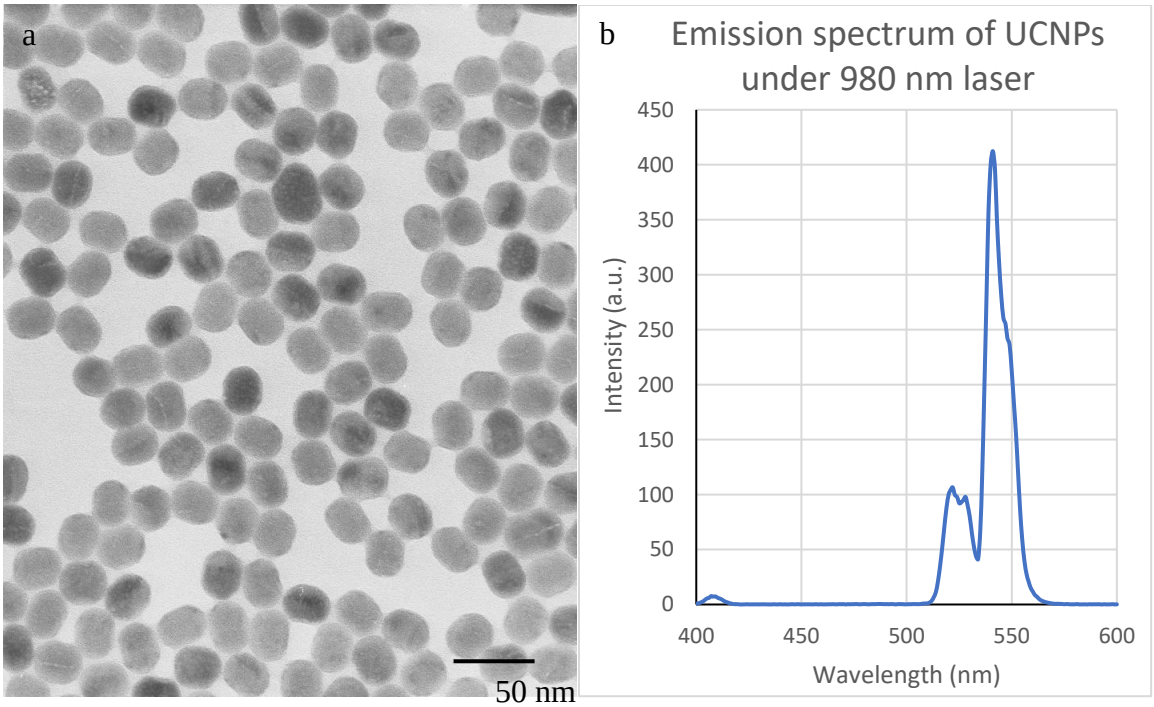

Figure 3.4 TEM image (a) and emission spectrum (b) of UCNPs. The diameter of UCNP is 30 nm; the scale bar indicates 50 nm. The excitation wavelength of UCNP is 980 nm; the emission light is at 541 nm.

The TEM image of Au NPs (Fig. 3.5a) shows that Au NPs are irregular in shape with a uniform size of 20 nm as the diameter. The absorption spectrum (Fig. 3.5b) proves the absorption area of Au NPs overlaps the emission light of UCNPs. The highest absorbance of Au NPs is at 546 nm. The spectrums of UCNPs and Au NPs demonstrate that Au NPs can be used as a quencher for UCNPs.

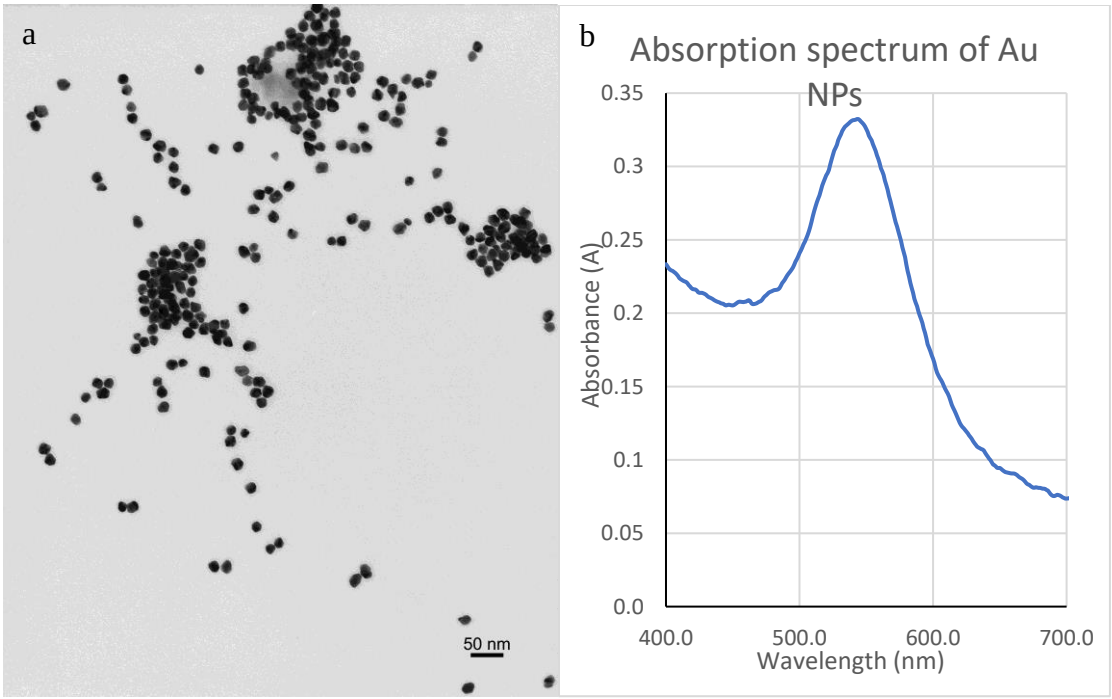

Figure 3.5 TEM image (a) and absorption spectrum (b) of Au NPs. The diameter of the Au NP is 20 nm; the scale bar indicates 50 nm. The absorption peak of Au NP in b is at 546 nm.

After DNA modification, UCNPs and Au NPs were characterized by TEM and emission spectrum to study the influence of the DNA label. As shown in Figure 3.6, for both UCNPs and Au NPs, there is no significant change in size, shape, or spectrum after DNA modification. Therefore, DNA modified Au NPs are still able to quench the DNA modified UCNPs. However, UCNPs are slightly aggregated after DNA modification. We suggest this aggregation follows the mechanism of the interaction between DNA and UCNPs. The phosphate groups on DNA interact with the lanthanide ions on UCNPs.[119] Thus, a single DNA strand can react with a few UCNPs and links them together; each UCNP may interact with several DNA strands as well, that further aggregates the UCNPs. Although we used IGEPAL® CO-520 to lower the interaction between DNA and UCNPs, aggregation could not be fully avoided. The TEM image of DNA modified UCNPs without IGEPAL® CO-520 is shown in Figure 3.7, in which aggregation is prominent.

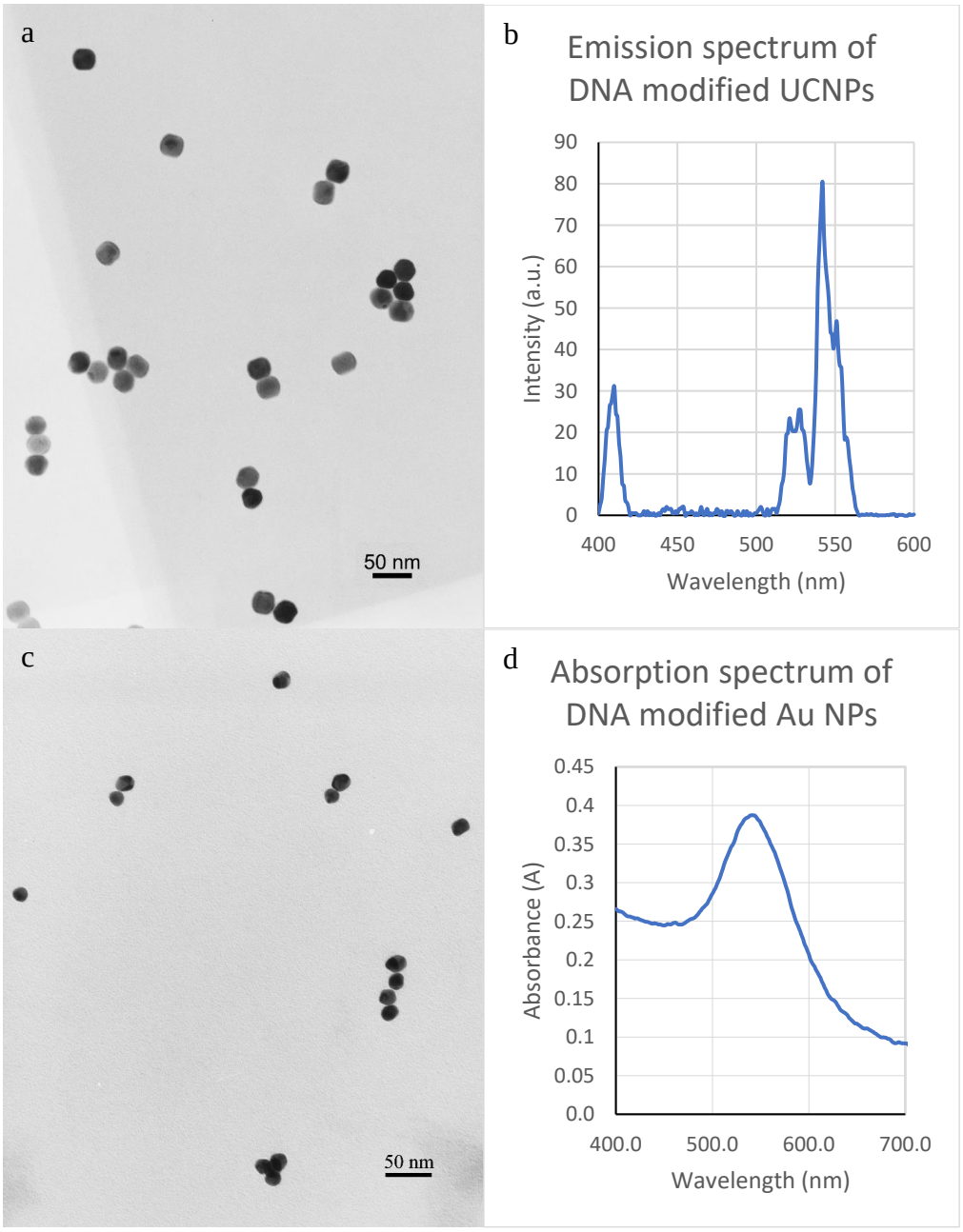

Figure 3.6 TEM image (a) and emission spectrum (b) of DNA modified UCNPs; TEM image (c) and absorption spectrum (d) of DNA modified Au NPs. The scale bars in a and c indicate 50 nm. Neither the shape nor the spectrum was significantly changed for UCNPs and Au NPs after the DNA modification.

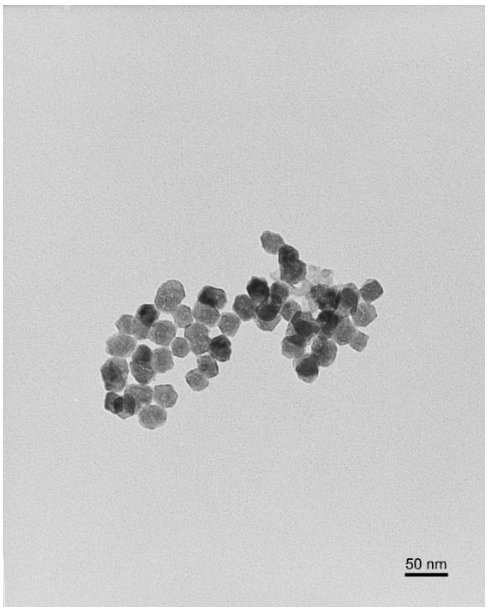

Figure 3.7 TEM image of DNA modified UCNPs without IGEPAL® CO-520. The scale bar indicates 50 nm.

3.5.2 Characterization of NPMBs and UCNP emission spectrum

Different ratios between UCNPs and Au NPs were tried to ensure maximum quench efficiency without the target but measurable fluorescence recovery with the target present. Finally, NPMBs were made by 1 mL of DNA modified Au NPs with 200 μL of DNA modified UCNPs due to the best performance of DNA detection. The NPMBs were characterized by TEM and fluorescence spectrometer as shown in Figure 3.8. In the TEM images (Fig. 3.8a), several UCNPs are observed surrounding one or two Au NPs. This likely arises from two sources. First, UCNPs slightly aggregated during DNA modification. Second, on the surface of Au NPs, there are dozens of DNA strands, but there are only a few DNA stands on UCNPs. As a result, each Au NP can bind with multiple UCNPs. Unlike NPMB, in the control group, most Au NPs and UCNPs are separate. This indicates that the function of DNA probes in positioning the quencher and the fluorophore in proximity. The spectrums of NPMBs, control MBs, and DNA modified UCNPs

(Fig. 3.8c) were detected with the same concentration of UCNPs. The 980 nm laser was used as excitation light. The spectrums prove that the DNA modified Au NPs can significantly quench DNA modified UCNPs without changing the spectrum pattern. In addition, the fluorescence intensity of the control group is lower than NPMB, which further proves the function of DNA probes. These spectrums indicate the NPMBs could be potentially applied for nucleic acid detection.

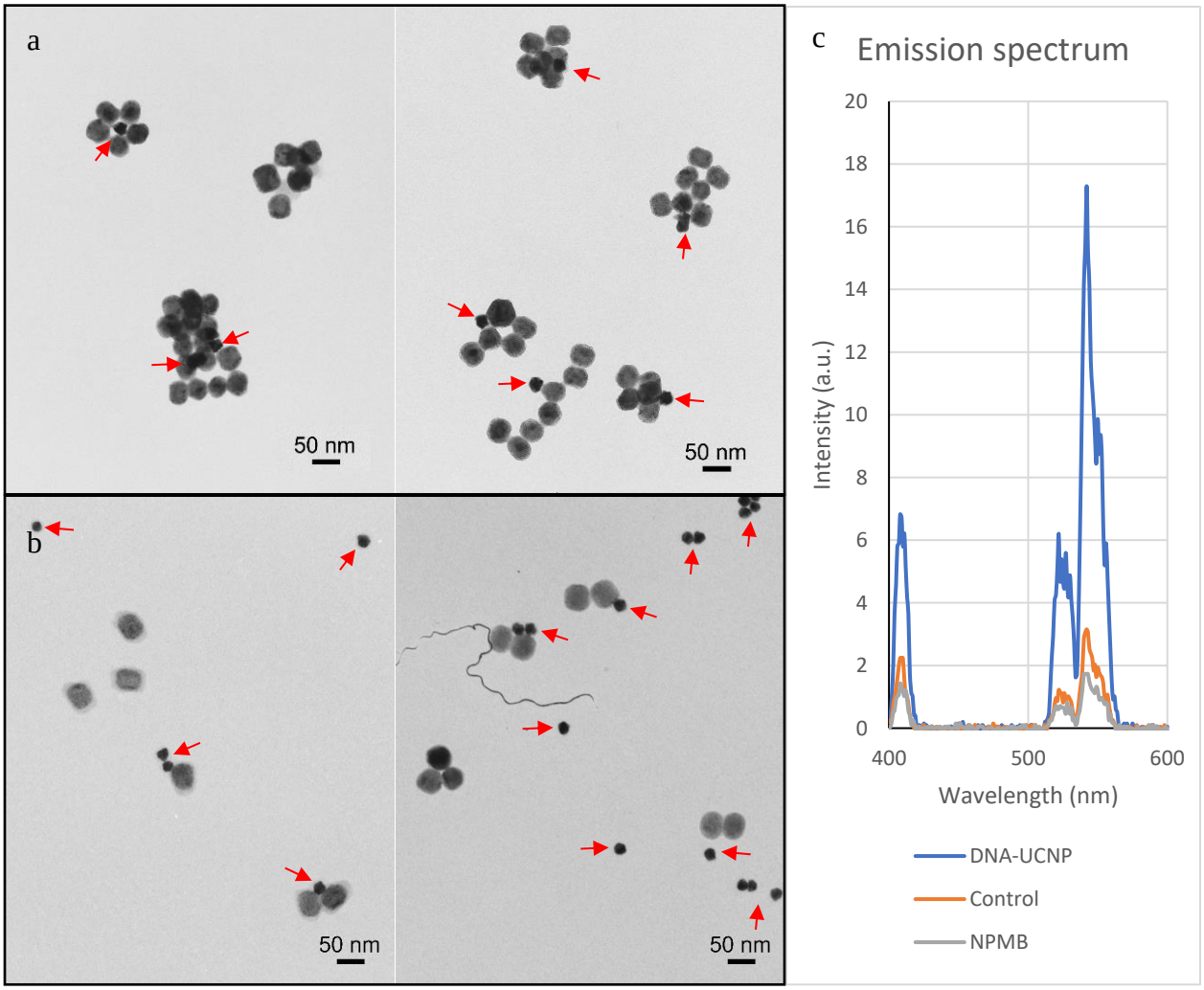

Figure 3.8 TEM images of NPMB (a) and control group (b); emission spectrum (c) of the control group (Blue), NPMBs (Orange), and DNA modified UCNPs (DNA-UCNPs, gray). The scale bar indicates 50 nm in the TEM images. The red arrows indicate the Au NPs. Same concentrations of

UCNPs are detected for spectrum in NPMB solution, control solution, and DNA modified UCNPs. The control group was synthesized by using non-complementary DNA probes.

Origin® 8.6 was used to fit the UCNP emission spectrum as shown in Figure 3.9. The spectrum is fitted as 4 peaks. In data analysis, the cumulative peak area of fit peak 3 and fit peak 4 is used as the main peak area; the cumulative peak area of all four fit peaks is used as the whole peak area. Based on the subsequent study, the detection linearity of the main peak area is better than the whole peak area, yet both the main peak area and the whole peak area can be used to determine the target concentration.

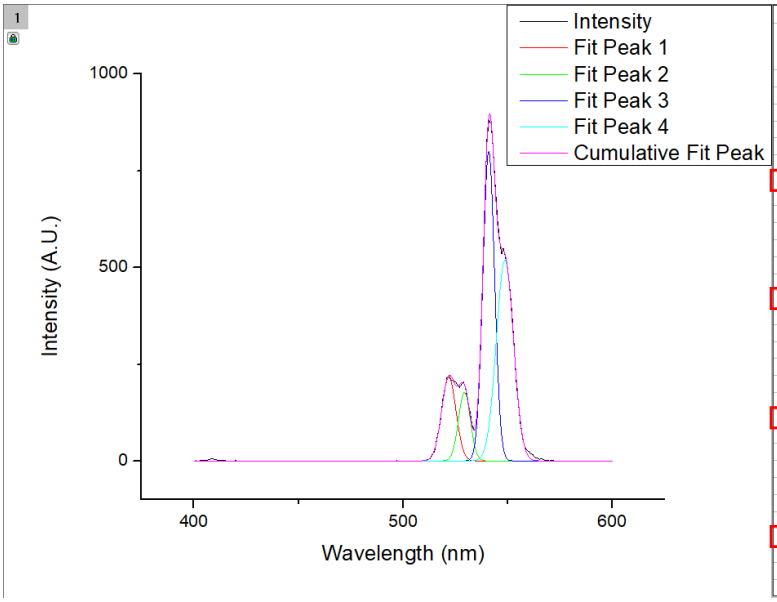

Model	Gauss		
Equation	y=y0 + (A/(w*sqrt(PI/2)))*exp(-2*((x-xc)/w)^2)		
Reduced Chi-Sqr	13.77049		
Adj. R-Square	0.99955		
		Value	Standard Error
Peak1(Intensity)	y0	0.87077	0.29888
Peak1(Intensity)	xc	521.82766	0.12753
Peak1(Intensity)	w	6.84736	0.17998
Peak1(Intensity)	A	1848.21966	62.89878
Peak1(Intensity)	sigma	3.42368	0.08999
Peak1(Intensity)	FWHM	8.06216	0.21191
Peak1(Intensity)	Height	215.36257	2.83592
Peak2(Intensity)	y0	0.87077	0.29888
Peak2(Intensity)	xc	529.27763	0.12228
Peak2(Intensity)	w	5.6353	0.1808
Peak2(Intensity)	A	1250.19071	63.13549
Peak2(Intensity)	sigma	2.81765	0.0904
Peak2(Intensity)	FWHM	6.63506	0.21288
Peak2(Intensity)	Height	177.0106	4.39832
Peak3(Intensity)	y0	0.87077	0.29888
Peak3(Intensity)	xc	540.91709	0.0225
Peak3(Intensity)	w	5.54603	0.0355
Peak3(Intensity)	A	5559.15062	67.59565
Peak3(Intensity)	sigma	2.77301	0.01775
Peak3(Intensity)	FWHM	6.52995	0.04179
Peak3(Intensity)	Height	799.7727	5.74126
Peak4(Intensity)	y0	0.87077	0.29888
Peak4(Intensity)	xc	548.64297	0.05951
Peak4(Intensity)	w	8.20292	0.08621
Peak4(Intensity)	A	5328.61907	68.90719
Peak4(Intensity)	sigma	4.10146	0.04311
Peak4(Intensity)	FWHM	9.6582	0.10151
Peak4(Intensity)	Height	518.30583	2.43665

Figure 3.9 Peak fit image of UCNP emission spectrum. The emission spectrum of UCNP is fitted as 4 peaks by Origin® 8.6. The cumulative peak area of fit peak 3 and fit peak 4 is used as the main peak area for data analysis; the cumulative peak area of all four fit peaks is used as the whole peak area.

3.5.3 Detection of DNA and RNA in different solutions

To validate the detection of NPMBs, DNA-mi21 in an aqueous solution was detected. As shown in Figure 3.10, within the DNA concentration range of 1 aM to 1 pM, the fluorescence signal of NPMBs increased correspondingly to the increasing concentration. The main peak area and whole peak area were used for analysis, and the coefficient of determination (R^2) for both area versus target concentration plotting, from 1aM to 100 fM, is larger than 0.99, which indicates high linearity. In other words, the detection range of NPMBs for DNA in an aqueous solution is from 1 aM to 1 pM while the linear detection range is from 1 aM to 100 aM.

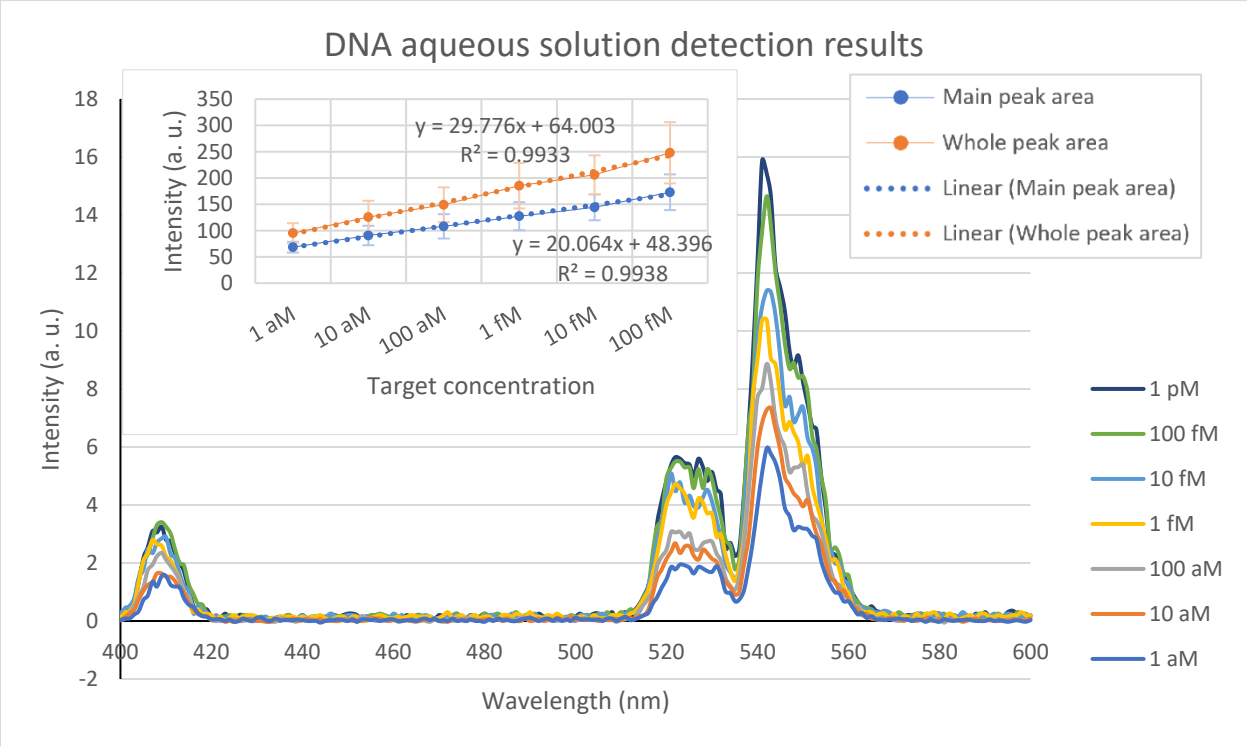

Figure 3.10 UCNPs emission spectrum with different target DNA concentrations. The concentrations are the final concentrations of detected samples. The error bar indicates the cumulative standard errors from Origin® 8.6. Both the main peak area (Blue) and whole peak area

(Orange) indicate that the linear detection range for the target DNA aqueous solution is from 1 aM to 100 fM.

miR-21 in aqueous solution was also analyzed to evaluate the detecting resolution of NPMBs against RNAs (Fig. 3.11 and 3.12). Similar to DNA aqueous solution detection, the higher target concentration leads to the growth of the fluorescence signal when the target RNA ranges from 1 aM to 1 pM. However, the linear detection range rose to 100 fM to 1 pM, which was 1 aM to 100 fM for DNA. One possible reason is that RNA is less stable than DNA sharing a similar sequence, especially with such a short length at such low concentrations. Although autoclaved Milli-Q™ (Millipore) purified water and RNase free pipette tips were used for the experiments, part of RNAs might still degrade.

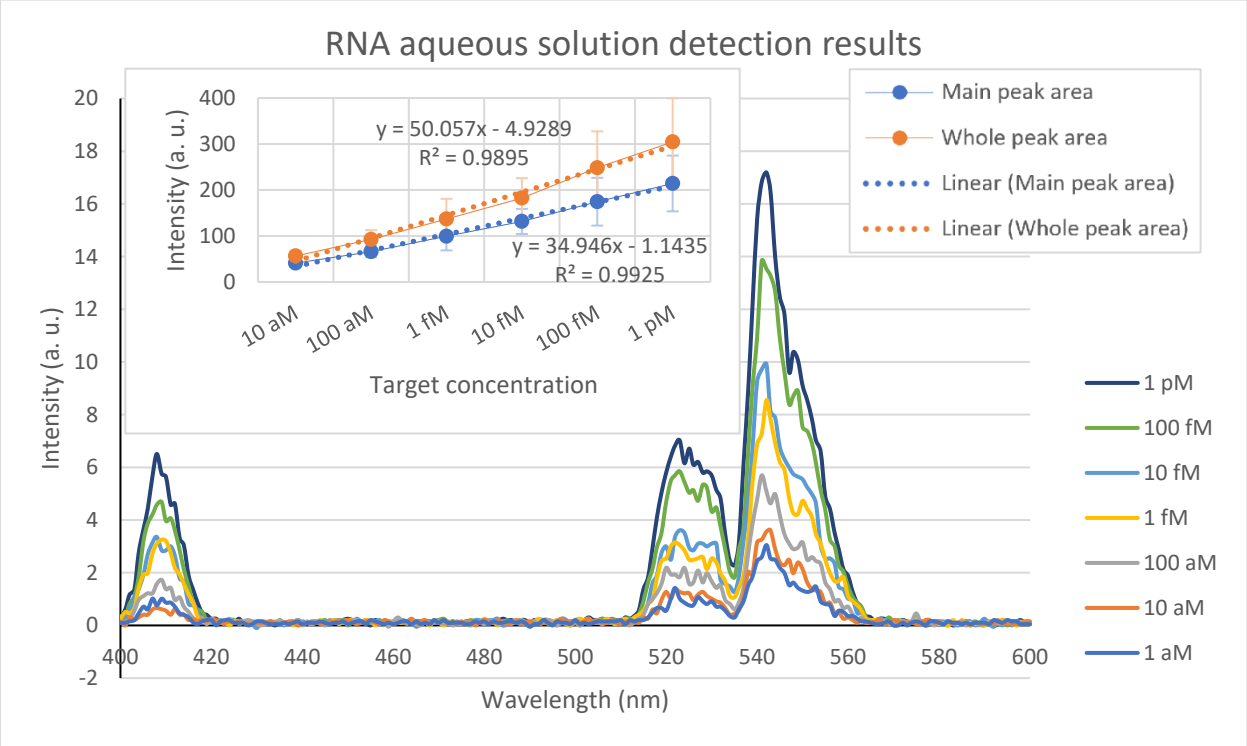

Figure 3.11 UCNPs emission spectrum with different target RNA concentration in aqueous solution. The concentrations are the final concentrations of detected samples. The error bar

indicates the cumulative standard errors from Origin® 8.6. Both the main peak area (Blue) and the whole peak area (Orange) indicate that the linear detection range for target RNA aqueous solution is from 10 aM to 1 pM.

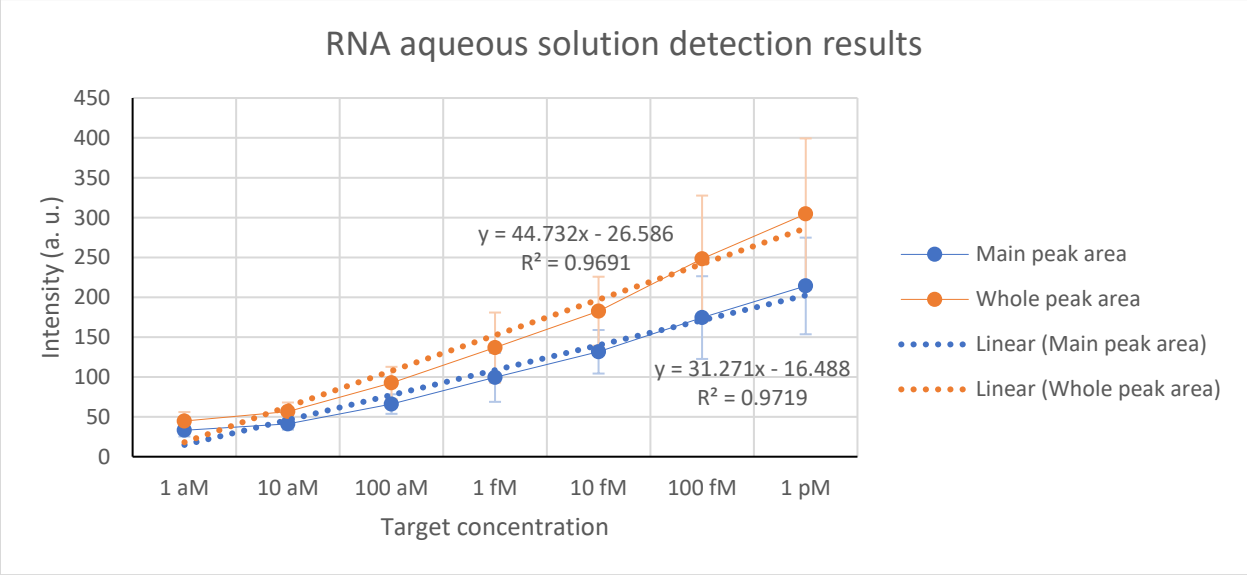

Figure 3.12 UCNPs emission intensity vs target RNA concentration in aqueous solution. The data point at 1 aM of the target miR-21 concentration was off from the trendline, which indicates that 1 aM is out of the linear detection range for RNA, so as the lower R^2.

To further study the NPMBs detection performance in a complex environment, miR-21 in spiked plasma was investigated (Fig. 3.13 and 3.14). Figure 3.13 proves that NPMBs are capable to quantify aM level RNA in plasma without purification. Furthermore, Figures 3.13 and 3.14 proved that the detection sensitivity of NPMBs is not influenced by background nucleic acids and proteins in plasma, because the detectable concentration is still 1 aM to 1 pM and the linear detection range is still from 10 aM to 1 pM, as same as the one for RNA in aqueous solution. This indicates NPMBs can be potentially used to detect small RNA in cell lysis solution without purification. In this RNA plasma detection, although the coefficients of determination (R^2) for 1

aM to 1 pM is higher than the one for 10 aM to 1 pM (Fig. 3.13 and 3.14), we think the data at 1 aM is not reliable and should not be counted into the linear detection range. Because the fluorescence signal at 1 aM had a different peak shape, which contained four peaks in the main peak area rather than two (Fig. 3.13). The different shape of fluorescence indicates experimental errors and the data at 1 aM is not reliable. In addition, we would like to point out that the 980 nm laser was repaired for the damage before the RNA plasma detection. It resulted in different laser power for RNA plasma detection compared to the other two detection trails. Figures 3.10 to 3.14 presented that the fluorescence intensity of RNA plasma detection is overall higher than DNA/RNA aqueous detection. The variable laser powers generate the variation of detection resolution that can be evaluated by the slopes of the linear fitting equations. The larger slop indicates a higher resolution.

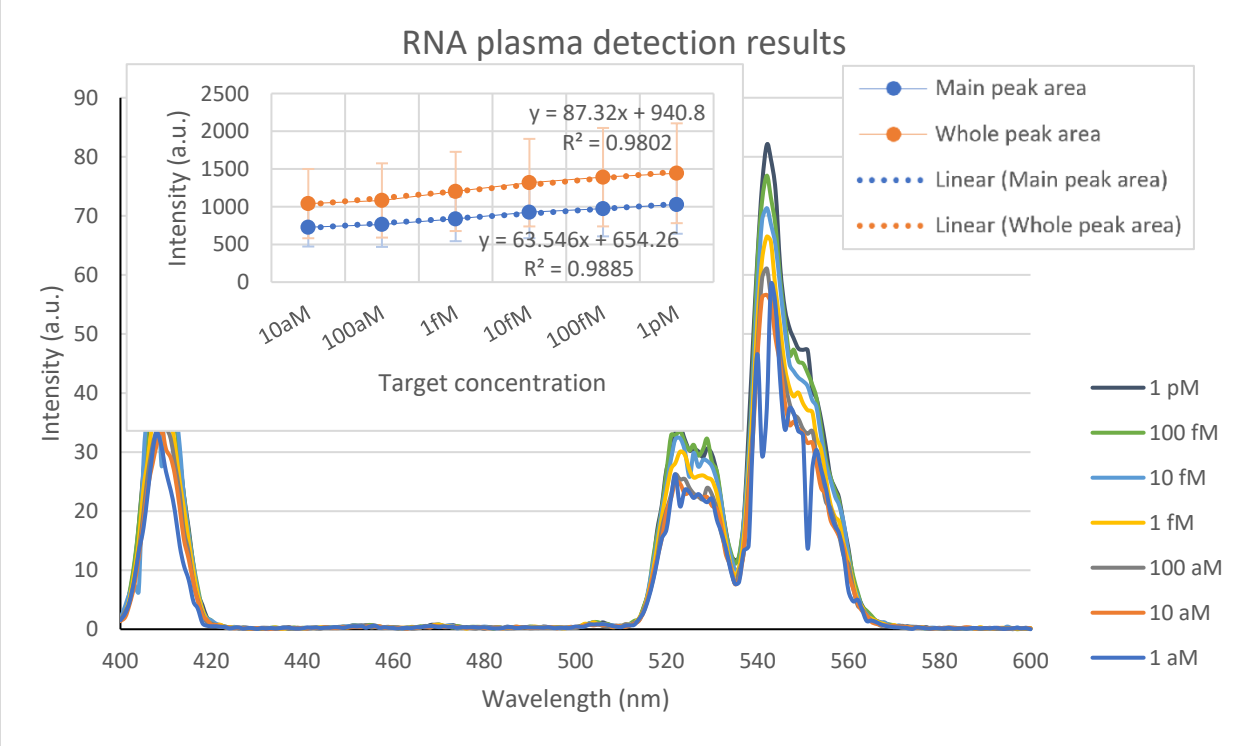

Figure 3.13 UCNPs emission spectrum with different target RNA concentration in plasma. The

concentrations are the final concentrations of detected samples. The error bar indicates the cumulative standard errors from Origin® 8.6. Both the main peak area (Blue) and the whole peak area (Orange) indicate that the linear detection range for target RNA plasma solution is from 10 aM to 1 pM.

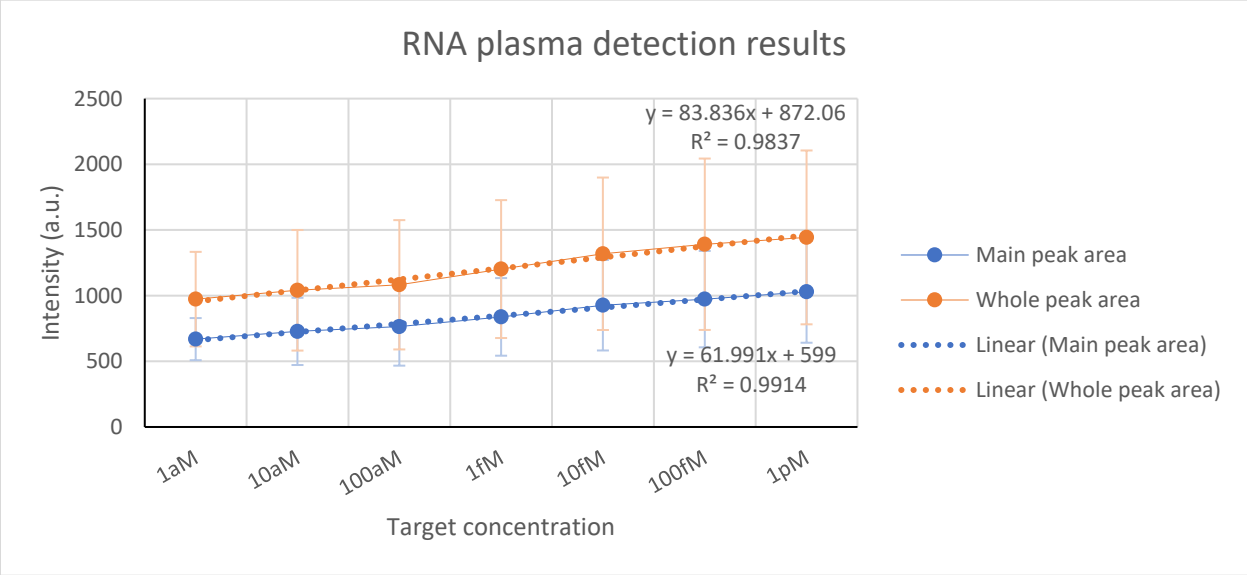

Figure 3.14 UCNPs emission intensity vs target RNA concentration in plasma. Although R^2 is higher for range 1 aM to 1 pM than the one for range 10 aM to 1 pM, 1 aM should not be included in the linear detection range for RNA in the plasma due to the abnormal shape of the fluorescence at 1 aM.

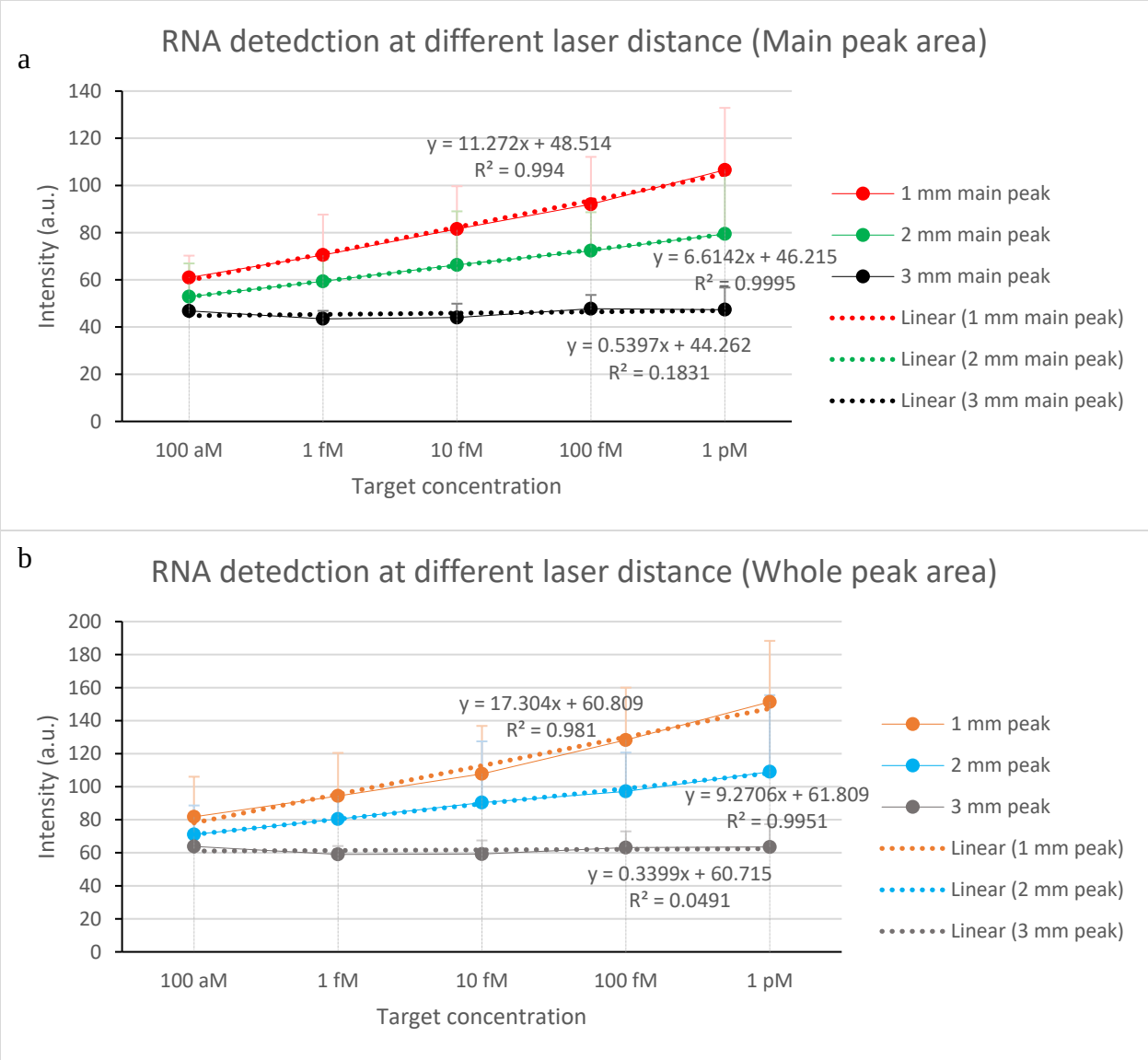

Figure 3.15 UCNPs emission intensity *vs* target RNA concentration in aqueous solution at different distances between laser and sample. The slopes of the trendlines decrease while the laser-sample distances increase.

Another important factor to promise repeatable precise small RNA/DNA quantification by NPMBs is to standardize the distance between the laser point and the sample solution. In the experiment, the external laser was settled manually. In every detection trail, the position of the laser could be slightly moved. To investigate the relation between the detection resolution and the

distance from the laser source, the detection was operated under different distances between the samples and the laser source with the same laser power. The results are presented in Figure 3.15. The increasing laser-sample distance decreased the detection resolution. When the distance is further than 2 mm, the fluorescence signals of NPMBs has no significant difference among different target concentrations. Overall, the excitation light intensity, decided by the laser power and the laser-sample distance, influences the fluorescence intensity to control the detection resolution.

In sum, the small RNA/DNA quantification probe, NPMB, can successfully detect both small DNA and small RNA from 1 aM to 1 pM. The linear detection range is 1 aM to 100 fM for DNA and 10 aM to 1 pM for RNA. Furthermore, the unpurified RNA in plasma can be detected with the same detection region.

3.6 Conclusion and discussion

In conclusion, we verified the fluorescence of pyro has the potential to be utilized for RNA quantification. Although the singlet oxygen signal linearly depends on the concentration of pyro, we failed to quantify the target RNA by using the singlet oxygen signal due to the background caused by magnetic beads. However, if the purification method is redesigned to avoid magnetic beads in the analyte, the singlet oxygen signal of pyro might be helpful for RNA quantification. For instance, biotin could be replaced by desthiobiotin. Because the binding between desthiobiotin and streptavidin is reversible,[124] magnetic beads are able to be separated from pyro after the washing step.

In addition, magnetic beads were found to trigger the fluorescent signal of SOSG which is considered to be triggered only by singlet oxygen. This indicates that either magnetic beads can

generate singlet oxygen that was not reported, or SOSG's fluorescence could be triggered by something besides singlet oxygen. Further investigations are required to verify our hypotheses.

Besides, we developed a NPMB for simple and rapid small RNA detection with low background and detection limit by using UCNPs as fluorophores and Au NPs as quenchers. The special optical property of UCNPs enables NPMB to achieve label-free and purification-free RNA detection. This method can detect small RNA as low as aM level in complex, such as plasma. This indicates that the NPMB has the potential to quantify small RNAs in cell lysis solutions. The detection resolution is influenced by the laser power and the laser-sample distance.

Chapter 4: Summary and discussion

4.1 Summary

As one of the most common causes of death, cancer terminates millions of lives globally every year.[1] For most types of cancers, early diagnosis is one of the key factors to increase the survival rate.[1] My studies were focusing on developing and applying various functional nanomaterials for early diagnosis of cancer, including non-invasive cancer imaging[2-3] and RNA biomarker detection[4].

On one hand, we developed an effortless strategy to synthesize MNPCs as a potential contrast agent to enhance the quality of MRI for tumor diagnostic imaging. Meanwhile, to specifically increase the accumulation of diagnostic isotope in the tumors, we tagged a tumor-homing peptide sequence with ^{99m}Tc for targeted SPECT.

On the other hand, we proposed two strategies utilizing pyro and UCNPs to quantify small RNA biomarkers with approximating 20 nts/bps which are so small that unsuitable for cDNA synthesis.

4.2 Novel nanomaterials for cancer imaging

Here, we proposed two strategies to improve and expand the application of MRI or SPECT cancer imaging associating studies. One is to develop a simple, economic method to recompose the IONPs to MNPCs those are contract agent for MRI. The other one is to surface modify tumor targeted phages with chelator NHS-MAG_3 and ^{99m}Tc to evaluate the tumor imaging quality of SPECT in an animal tumor model.

4.2.1 New MNPCs synthesis strategy for MRI

Although starting with hydrophobic IONP precursors is inevitable to assemble MNPCs, instead of directly synthesizing costly and non-scalable hydrophobic IONPs, our phase transfer strategy starts with aqueous IONPs and converts aqueous IONPs to hydrophobic IONP precursors in an extremely rapid and simple way. The polyanionic molecules were confirmed to play an important role to successfully transfer the IONPs from the aqueous to the oil phase. The polyanion can cap the IONPs once they are added into the nanoparticle solution, which was indicated by a surface charge reversal of the IONPs. The highly negative charge of the poly-anion molecules can further interact with the amine groups of oleyamine to form a second coating around the IONPs, which enabled the nanoparticles to be successfully transferred from the aqueous phase to the oil phase. Neither the aqueous IONPs synthesis nor the phase transfer required any sophisticated experimental setups or costly precursor chemicals. Therefore, our novel strategy significantly reduces the efforts and costs needed for the preparation of MNPCs. However, the performance of our as-prepared MNPCs as a MRI contrast agent needs to be examined.

4.2.2 SPECT for tumor targeted imaging

To surmount the barrier of the uncertainty of the EPR effect, breast cancer targeting phages were radioactively labeled and applied in SPECT for targeting imaging. These phages were likely to achieve targeting imaging because the breast cancer tumor was visualized at 1 h post injection while there was no visible signal in the tumor in the wild-type group until 4 h post injection. However, it cannot be concluded without a repeat of the animal studies. More objects in each group and an extra group with the injection of free ^{99m}Tc are desirable.

4.3 Accurate and sensitive strategies for small RNA quantification

In the two strategies we proposed, pyro and UCNPs were utilized for RNA quantification for the first time because of their special optical characters. Pyro produces singlet oxygen with a laser treatment; the stronger the laser treatment, the more singlet oxygen for quantification. UCNPs emit light at a shorter wavelength compared with its excitation light. It is the opposite of most substances that leads to the ultra-low background for quantification.

4.3.1 Small RNA quantification based on pyro

In this strategy, pyro was proved to have the potential to be applied in RNA quantification because its singlet oxygen producing ability was found to be linear dependent on its concentration. Although the RNA quantification based on the singlet oxygen was failed due to the strong background of magnetic beads, the quantification based on the fluorescence of pyro was achieved within the target concentration ranges of 2 pM to 20 nM. In addition, the influence of the background causing by magnetic beads could be theoretically removed by replacing the biotin with desthiobiotin which reversibly binds with magnetic beads with high affinity. Furthermore, SOSG, reported as highly selective for singlet oxygen, had a response to magnetic beads, whereas the mechanism is unclear.

4.3.2 Low LOD quantification strategy for small RNA quantification

We developed a NPMB for simple and rapid small RNA detection with low background and low detection limit by using UCNPs as fluorophores and Au NPs as quenchers. This label-free and purification-free RNA detection probe is able to quantify small RNA from 10 aM to 1 pM.

Future work can focus on applying NPMBs to multi-target detection by recruiting UCNPs with different emissions. As an example, two types of NPMB could be used in one analyte, NPMB-21 and NPMB-195. NPMB-21 is composed of UCNP with green emission and Au NP modified

by miR-21 recognizing hairpin DNA while NPMB-195 comprises UCNP with red emission and Au NP modified by miR-195 detection probe. The target miR-21 would hybridize with NPMB-21 following a green fluorescence recovery, and the target miR-195 can hybridize with NPMB-195 leading to a red fluorescent signal. As a result, the intensity of 540 nm (green) presents the concentration of miR-21 while the intensity of 650 nm (red) presents the concentration of miR-195. In the same way, a third target RNA can be detected by UCNPs emitting blue light.

References

1. Fact sheets: Cancer. https://www.who.int/news-room/fact-sheets/detail/cancer (accessed 11 January).
2. Reggiani, C.; Manfredini, M.; Mandel, V. D.; Farnetani, F.; Ciardo, S.; Bassoli, S.; Casari, A.; Guida, S.; Argenziano, G.; Lallas, A.; Ulrich, M.; Pellacani, G.; Longo, C., Update on non-invasive imaging techniques in early diagnosis of non-melanoma skin cancer. *G Ital Dermatol Venereol* **2015,** *150* (4), 393-405.
3. Wu, X.; Wu, M.; Zhao, J. X., Recent development of silica nanoparticles as delivery vectors for cancer imaging and therapy. *Nanomedicine* **2014,** *10* (2), 297-312.
4. Necula, L.; Matei, L.; Dragu, D.; Neagu, A. I.; Mambet, C.; Nedeianu, S.; Bleotu, C.; Diaconu, C. C.; Chivu-Economescu, M., Recent advances in gastric cancer early diagnosis. *World J Gastroenterol* **2019,** *25* (17), 2029-2044.
5. Frangioni, J. V., New technologies for human cancer imaging. *J Clin Oncol* **2008,** *26* (24), 4012-21.
6. Buzug, T. M., Computed Tomography. In *Springer Handbook of Medical Technology*, Kramme, R.; Hoffmann, K.-P.; Pozos, R. S., Eds. Springer Berlin Heidelberg: Berlin, Heidelberg, 2011; pp 311-342.
7. Reuveni, T.; Motiei, M.; Romman, Z.; Popovtzer, A.; Popovtzer, R., Targeted gold nanoparticles enable molecular CT imaging of cancer: an in vivo study. *Int J Nanomedicine* **2011,** *6*, 2859-64.
8. Nitz, W. R., Magnetic Resonance Imaging. In *Springer Handbook of Medical Technology*, Kramme, R.; Hoffmann, K.-P.; Pozos, R. S., Eds. Springer Berlin Heidelberg: Berlin, Heidelberg, 2011; pp 439-460.
9. Na, H. B.; Song, I. C.; Hyeon, T., Inorganic Nanoparticles for MRI Contrast Agents. *Advanced Materials* **2009,** *21* (21), 2133-2148.
10. Beheshti, M.; Langsteger, W.; Fogelman, I., Prostate cancer: role of SPECT and PET in imaging bone metastases. *Semin Nucl Med* **2009,** *39* (6), 396-407.
11. Farwell, M. D.; Pryma, D. A.; Mankoff, D. A., PET/CT imaging in cancer: current applications and future directions. *Cancer* **2014,** *120* (22), 3433-45.
12. Wagner, L. M.; Kremer, N.; Gelfand, M. J.; Sharp, S. E.; Turpin, B. K.; Nagarajan, R.; Tiao, G. M.; Pressey, J. G.; Yin, J.; Dasgupta, R., Detection of lymph node metastases in pediatric and adolescent/young adult sarcoma: Sentinel lymph node biopsy versus fludeoxyglucose positron emission tomography imaging-A prospective trial. *Cancer* **2017,** *123* (1), 155-160.
13. Yen, T. C.; See, L. C.; Chang, T. C.; Huang, K. G.; Ng, K. K.; Tang, S. G.; Chang, Y. C.; Hsueh, S.; Tsai, C. S.; Hong, J. H.; Lin, C. T.; Chao, A.; Ma, S. Y.; Lin, W. J.; Fu, Y. K.; Fan, C. C.; Lai, C. H., Defining the priority of using 18F-FDG PET for recurrent cervical cancer. *Journal of Nuclear Medicine* **2004,** *45* (10), 8.
14. Barreto, J. A.; O'Malley, W.; Kubeil, M.; Graham, B.; Stephan, H.; Spiccia, L., Nanomaterials: applications in cancer imaging and therapy. *Adv Mater* **2011,** *23* (12), H18-40.
15. Schiffman, J. D.; Fisher, P. G.; Gibbs, P., Early detection of cancer: past, present, and future. *Am Soc Clin Oncol Educ Book* **2015**, 57-65.
16. Mendell, J. T., MicroRNAs: critical regulators of development, cellular physiology and malignancy. *Cell Cycle* **2005,** *4* (9), 1179-84.
17. Gibb, E. A.; Vucic, E. A.; Enfield, K. S.; Stewart, G. L.; Lonergan, K. M.; Kennett, J. Y.; Becker-Santos, D. D.; MacAulay, C. E.; Lam, S.; Brown, C. J.; Lam, W. L., Human cancer long non-coding RNA transcriptomes. *PLoS One* **2011,** *6* (10), e25915.
18. Yang, G.; Lu, X.; Yuan, L., LncRNA: a link between RNA and cancer. *Biochim Biophys Acta* **2014,** *1839* (11), 1097-109.

19. Assumpcao, C. B.; Calcagno, D. Q.; Araujo, T. M.; Santos, S. E.; Santos, A. K.; Riggins, G. J.; Burbano, R. R.; Assumpcao, P. P., The role of piRNA and its potential clinical implications in cancer. *Epigenomics* **2015,** *7* (6), 975-84.
20. Gupta, R. A.; Shah, N.; Wang, K. C.; Kim, J.; Horlings, H. M.; Wong, D. J.; Tsai, M. C.; Hung, T.; Argani, P.; Rinn, J. L.; Wang, Y.; Brzoska, P.; Kong, B.; Li, R.; West, R. B.; van de Vijver, M. J.; Sukumar, S.; Chang, H. Y., Long non-coding RNA HOTAIR reprograms chromatin state to promote cancer metastasis. *Nature* **2010,** *464* (7291), 1071-6.
21. Silva, J. M.; Boczek, N. J.; Berres, M. W.; Ma, X.; Smith, D. I., LSINCT5 is over expressed in breast and ovarian cancer and affects cellular proliferation. *RNA Biology* **2014,** *8* (3), 496-505.
22. Nakagawa, T.; Endo, H.; Yokoyama, M.; Abe, J.; Tamai, K.; Tanaka, N.; Sato, I.; Takahashi, S.; Kondo, T.; Satoh, K., Large noncoding RNA HOTAIR enhances aggressive biological behavior and is associated with short disease-free survival in human non-small cell lung cancer. *Biochem Biophys Res Commun* **2013,** *436* (2), 319-24.
23. Lai, M. C.; Yang, Z.; Zhou, L.; Zhu, Q. Q.; Xie, H. Y.; Zhang, F.; Wu, L. M.; Chen, L. M.; Zheng, S. S., Long non-coding RNA MALAT-1 overexpression predicts tumor recurrence of hepatocellular carcinoma after liver transplantation. *Med Oncol* **2012,** *29* (3), 1810-6.
24. Chiyomaru, T.; Fukuhara, S.; Saini, S.; Majid, S.; Deng, G.; Shahryari, V.; Chang, I.; Tanaka, Y.; Enokida, H.; Nakagawa, M.; Dahiya, R.; Yamamura, S., Long non-coding RNA HOTAIR is targeted and regulated by miR-141 in human cancer cells. *J Biol Chem* **2014,** *289* (18), 12550-65.
25. Yan, L. X.; Huang, X. F.; Shao, Q.; Huang, M. Y.; Deng, L.; Wu, Q. L.; Zeng, Y. X.; Shao, J. Y., MicroRNA miR-21 overexpression in human breast cancer is associated with advanced clinical stage, lymph node metastasis and patient poor prognosis. *RNA* **2008,** *14* (11), 2348-60.
26. Tejero, R.; Navarro, A.; Campayo, M.; Vinolas, N.; Marrades, R. M.; Cordeiro, A.; Ruiz-Martinez, M.; Santasusagna, S.; Molins, L.; Ramirez, J.; Monzo, M., miR-141 and miR-200c as markers of overall survival in early stage non-small cell lung cancer adenocarcinoma. *PLoS One* **2014,** *9* (7), e101899.
27. Aprea, J.; Calegari, F., Long non-coding RNAs in corticogenesis: deciphering the non-coding code of the brain. *EMBO J* **2015,** *34* (23), 2865-84.
28. de Duve, C., Transfer RNAs: the second genetic code. *Nature* **1988,** *333* (6169), 117-8.
29. Smit, S.; Widmann, J.; Knight, R., Evolutionary rates vary among rRNA structural elements. *Nucleic Acids Res* **2007,** *35* (10), 3339-54.
30. Matera, A. G.; Terns, R. M.; Terns, M. P., Non-coding RNAs: lessons from the small nuclear and small nucleolar RNAs. *Nat Rev Mol Cell Biol* **2007,** *8* (3), 209-20.
31. Koerner, M. V.; Pauler, F. M.; Huang, R.; Barlow, D. P., The function of non-coding RNAs in genomic imprinting. *Development* **2009,** *136* (11), 1771-83.
32. Sharma, V.; Misteli, T., Non-coding RNAs in DNA damage and repair. *FEBS Lett* **2013,** *587* (13), 1832-9.
33. Wahlestedt, C., Targeting long non-coding RNA to therapeutically upregulate gene expression. *Nat Rev Drug Discov* **2013,** *12* (6), 433-46.
34. Xi, X.; Li, T.; Huang, Y.; Sun, J.; Zhu, Y.; Yang, Y.; Lu, Z. J., RNA Biomarkers: Frontier of Precision Medicine for Cancer. *Noncoding RNA* **2017,** *3* (1).
35. Cohen, J. D.; Javed, A. A.; Thoburn, C.; Wong, F.; Tie, J.; Gibbs, P.; Schmidt, C. M.; Yip-Schneider, M. T.; Allen, P. J.; Schattner, M.; Brand, R. E.; Singhi, A. D.; Petersen, G. M.; Hong, S.-M.; Kim, S. C.; Falconi, M.; Doglioni, C.; Weiss, M. J.; Ahuja, N.; He, J.; Makary, M. A.; Maitra, A.; Hanash, S. M.; Dal Molin, M.; Wang, Y.; Li, L.; Ptak, J.; Dobbyn, L.; Schaefer, J.; Silliman, N.; Popoli, M.; Goggins, M. G.; Hruban, R. H.; Wolfgang, C. L.; Klein, A. P.; Tomasetti, C.; Papadopoulos, N.; Kinzler, K. W.; Vogelstein, B.; Lennon, A. M., Combined circulating tumor DNA and protein biomarker-based liquid biopsy for the earlier detection of pancreatic cancers. *Proceedings of the National Academy of Sciences* **2017,** *114*, 10202-10207.

36. Xue, W.; Dahlman, J. E.; Tammela, T.; Khan, O. F.; Sood, S.; Dave, A.; Cai, W.; Chirino, L. M.; Yang, G. R.; Bronson, R.; Crowley, D. G.; Sahay, G.; Schroeder, A.; Langer, R.; Anderson, D. G.; Jacks, T., Small RNA combination therapy for lung cancer. *Proc Natl Acad Sci U S A* **2014,** *111* (34), E3553-61.
37. Riley, R. S.; Day, E. S., Gold nanoparticle-mediated photothermal therapy: applications and opportunities for multimodal cancer treatment. *Wiley interdisciplinary reviews. Nanomedicine and nanobiotechnology* **2017,** *9* (4).
38. Hayashi, K.; Nakamura, M.; Sakamoto, W.; Yogo, T.; Miki, H.; Ozaki, S.; Abe, M.; Matsumoto, T.; Ishimura, K., Superparamagnetic Nanoparticle Clusters for Cancer Theranostics Combining Magnetic Resonance Imaging and Hyperthermia Treatment. *Theranostics* **2013,** *3* (6), 366-376.
39. Katagiri, K.; Ohta, K.; Sako, K.; Inumaru, K.; Hayashi, K.; Sasaki, Y.; Akiyoshi, K., Development and Potential Theranostic Applications of a Self-Assembled Hybrid of Magnetic Nanoparticle Clusters with Polysaccharide Nanogels. *Chempluschem* **2014,** *79* (11), 1631-1637.
40. Huang, X.; El-Sayed, M. A., Gold nanoparticles: Optical properties and implementations in cancer diagnosis and photothermal therapy. *Journal of Advanced Research* **2010,** *1* (1), 13-28.
41. Qiu, P.; Mao, C., Viscosity gradient as a novel mechanism for the centrifugation-based separation of nanoparticles. *Adv Mater* **2011,** *23* (42), 4880-5.
42. He, Y. Q.; Liu, S. P.; Kong, L.; Liu, Z. F., A study on the sizes and concentrations of gold nanoparticles by spectra of absorption, resonance Rayleigh scattering and resonance non-linear scattering. *Spectrochim Acta A Mol Biomol Spectrosc* **2005,** *61* (13-14), 2861-6.
43. Qiu, P.; Yang, M.; Qu, X.; Huai, Y.; Zhu, Y.; Mao, C., Tuning photothermal properties of gold nanodendrites for in vivo cancer therapy within a wide near infrared range by simply controlling their degree of branching. *Biomaterials* **2016,** *104*, 138-144.
44. Scarabelli, L.; Grzelczak, M.; Liz-Marzán, L. M., Tuning Gold Nanorod Synthesis through Prereduction with Salicylic Acid. *Chemistry of Materials* **2013,** *25* (21), 4232-4238.
45. Senthil Kumar, P.; Pastoriza-Santos, I.; Rodríguez-González, B.; Javier García de Abajo, F.; Liz-Marzán, L. M., High-yield synthesis and optical response of gold nanostars. *Nanotechnology* **2008,** *19* (1).
46. Murphy, C. J.; Gole, A. M.; Hunyadi, S. E.; Stone, J. W.; Sisco, P. N.; Alkilany, A.; Kinard, B. E.; Hankins, P., Chemical sensing and imaging with metallic nanorods. *Chem Commun (Camb)* **2008,** (5), 544-57.
47. Qu, X.; Qiu, P.; Zhu, Y.; Yang, M.; Mao, C., Guiding nanomaterials to tumors for breast cancer precision medicine: from tumor-targeting small-molecule discovery to targeted nanodrug delivery. *NPG Asia Materials* **2017,** *9* (12), e452-e452.
48. Ghosh, P.; Han, G.; De, M.; Kim, C. K.; Rotello, V. M., Gold nanoparticles in delivery applications. *Adv Drug Deliv Rev* **2008,** *60* (11), 1307-15.
49. Arvizo, R.; Bhattacharya, R.; Mukherjee, P., Gold nanoparticles: opportunities and challenges in nanomedicine. *Expert Opin Drug Deliv* **2010,** *7* (6), 753-63.
50. Podaru, G.; Chikan, V., CHAPTER 1 Magnetism in Nanomaterials: Heat and Force from Colloidal Magnetic Particles. In *Magnetic Nanomaterials: Applications in Catalysis and Life Sciences*, The Royal Society of Chemistry: 2017; pp 1-24.
51. Thakor, A. S.; Jokerst, J. V.; Ghanouni, P.; Campbell, J. L.; Mittra, E.; Gambhir, S. S., Clinically Approved Nanoparticle Imaging Agents. *J Nucl Med* **2016,** *57* (12), 1833-1837.
52. Corot, C.; Robert, P.; Idee, J. M.; Port, M., Recent advances in iron oxide nanocrystal technology for medical imaging. *Adv Drug Deliv Rev* **2006,** *58* (14), 1471-504.
53. Harisinghani, M. G.; Barentsz, J.; Hahn, P. F.; Deserno, W. M.; Tabatabaei, S.; van de Kaa, C. H.; de la Rosette, J.; Weissleder, R., Noninvasive detection of clinically occult lymph-node metastases in prostate cancer. *N Engl J Med* **2003,** *348* (25), 2491-9.
54. Massart, R., Preparation of Aqueous Magnetic Liquids in Alkaline and Acidic Media. *Ieee Transactions on Magnetics* **1981,** *17* (2), 1247-1248.

55. Bee, A.; Massart, R.; Neveu, S., Synthesis of very fine maghemite particles. *Journal of Magnetism and Magnetic Materials* **1995,** *149* (1-2), 6-9.
56. Sun, S.; Zeng, H.; Robinson, D. B.; Raoux, S.; Rice, P. M.; Wang, S. X.; Li, G., Monodisperse MFe2O4 (M = Fe, Co, Mn) nanoparticles. *J Am Chem Soc* **2004,** *126* (1), 273-9.
57. Liu, Z.; Li, M.; Yang, X.; Yin, M.; Ren, J.; Qu, X., The use of multifunctional magnetic mesoporous core/shell heteronanostructures in a biomolecule separation system. *Biomaterials* **2011,** *32* (21), 4683-90.
58. Naccache, R.; Rodriguez, E. M.; Bogdan, N.; Sanz-Rodriguez, F.; Cruz Mdel, C.; Fuente, A. J.; Vetrone, F.; Jaque, D.; Sole, J. G.; Capobianco, J. A., High resolution fluorescence imaging of cancers using lanthanide ion-doped upconverting nanocrystals. *Cancers (Basel)* **2012,** *4* (4), 1067-105.
59. Wang, F.; Banerjee, D.; Liu, Y.; Chen, X.; Liu, X., Upconversion nanoparticles in biological labeling, imaging, and therapy. *Analyst* **2010,** *135* (8), 1839-54.
60. Chen, W.; Chen, M.; Zang, Q.; Wang, L.; Tang, F.; Han, Y.; Yang, C.; Deng, L.; Liu, Y. N., NIR light controlled release of caged hydrogen sulfide based on upconversion nanoparticles. *Chem Commun (Camb)* **2015,** *51* (44), 9193-6.
61. Weissleder, R., A clearer vision for in vivo imaging. *Nat Biotechnol* **2001,** *19* (4), 316-7.
62. Tian, G.; Zhang, X.; Gu, Z.; Zhao, Y., Recent Advances in Upconversion Nanoparticles-Based Multifunctional Nanocomposites for Combined Cancer Therapy. *Adv Mater* **2015,** *27* (47), 7692-712.
63. Sausset, R.; Petit, M. A.; Gaboriau-Routhiau, V.; De Paepe, M., New insights into intestinal phages. *Mucosal Immunol* **2020,** *13* (2), 205-215.
64. Wang, J.; Wang, L.; Li, X.; Mao, C., Virus activated artificial ECM induces the osteoblastic differentiation of mesenchymal stem cells without osteogenic supplements. *Scientific Reports* **2013,** *3* (1), 1242.
65. Smith, G. P.; Petrenko, V. A., Phage display. *Chem Rev* **1997,** *97* (2), 391-410.
66. Kehoe, J. W.; Kay, B. K., Filamentous phage display in the new millennium. *Chem Rev* **2005,** *105* (11), 4056-4072.
67. Rakonjac, J.; Bennett, N. J.; Spagnuolo, J.; Gagic, D.; Russel, M., Filamentous bacteriophage: biology, phage display and nanotechnology applications. *Current issues in molecular biology* **2011,** *13* (2), 51-76.
68. Moon, J. S.; Choi, E. J.; Jeong, N. N.; Sohn, J. R.; Han, D. W.; Oh, J. W., Research Progress of M13 Bacteriophage-Based Biosensors. *Nanomaterials (Basel)* **2019,** *9* (10).
69. Krag, D. N.; Shukla, G. S.; Shen, G. P.; Pero, S.; Ashikaga, T.; Fuller, S.; Weaver, D. L.; Burdette-Radoux, S.; Thomas, C., Selection of tumor-binding ligands in cancer patients with phage display libraries. *Cancer Res* **2006,** *66* (15), 7724-33.
70. Sarikaya, M.; Tamerler, C.; Schwartz, D. T.; Baneyx, F. O., Materials assembly and formation using engineered polypeptides. *Annu Rev Mater Res* **2004,** *34*, 373-408.
71. Huang, W.; Petrosino, J.; Palzkill, T., Display of functional beta-lactamase inhibitory protein on the surface of M13 bacteriophage. *Antimicrobial agents and chemotherapy* **1998,** *42* (11), 2893-7.
72. Lee, S. K.; Yun, D. S.; Belcher, A. M., Cobalt ion mediated self-assembly of genetically engineered bacteriophage for biomimetic Co-Pt hybrid material. *Biomacromolecules* **2006,** *7* (1), 14-7.
73. Tomszak, F.; Weber, S.; Zantow, J.; Schirrmann, T.; Hust, M.; Frenzel, A., Selection of Recombinant Human Antibodies. In *Protein Targeting Compounds: Prediction, Selection and Activity of Specific Inhibitors*, Böldicke, T., Ed. Springer International Publishing: Cham, 2016; pp 23-54.
74. Maeda, H.; Khatami, M., Analyses of repeated failures in cancer therapy for solid tumors: poor tumor-selective drug delivery, low therapeutic efficacy and unsustainable costs. *Clin Transl Med* **2018,** *7* (1), 11.

75. Harrington, K. J.; Mohammadtaghi, S.; Uster, P. S.; Glass, D.; Peters, A. M.; Vile, R. G.; Stewart, J. S. W., Effective Targeting of Solid Tumors in Patients With Locally Advanced Cancers by Radiolabeled Pegylated Liposomes. *Clinical Cancer Research* **2001,** *7* (2), 243-254.
76. Tanaka, N.; Kanatani, S.; Tomer, R.; Sahlgren, C.; Kronqvist, P.; Kaczynska, D.; Louhivuori, L.; Kis, L.; Lindh, C.; Mitura, P.; Stepulak, A.; Corvigno, S.; Hartman, J.; Micke, P.; Mezheyeuski, A.; Strell, C.; Carlson, J. W.; Fernandez Moro, C.; Dahlstrand, H.; Ostman, A.; Matsumoto, K.; Wiklund, P.; Oya, M.; Miyakawa, A.; Deisseroth, K.; Uhlen, P., Whole-tissue biopsy phenotyping of three-dimensional tumours reveals patterns of cancer heterogeneity. *Nat Biomed Eng* **2017,** *1* (10), 796-806.
77. Laurent, M.; Ricard, J.-L.; Bahain, J.-J.; Voinchet, P.; Rousseau, L., Datation du site Paléolithique moyen de la Butte d'Arvigny (Moissy-Cramayel, Seine-et-Marne). *Comptes Rendus de l'Académie des Sciences - Series IIA - Earth and Planetary Science* **2000,** *330* (8), 581-583.
78. McDonald, R. J.; McDonald, J. S.; Kallmes, D. F.; Jentoft, M. E.; Murray, D. L.; Thielen, K. R.; Williamson, E. E.; Eckel, L. J., Intracranial Gadolinium Deposition after Contrast-enhanced MR Imaging. *Radiology* **2015,** *275* (3), 772-82.
79. Kim, B. H.; Lee, N.; Kim, H.; An, K.; Park, Y. I.; Choi, Y.; Shin, K.; Lee, Y.; Kwon, S. G.; Na, H. B.; Park, J. G.; Ahn, T. Y.; Kim, Y. W.; Moon, W. K.; Choi, S. H.; Hyeon, T., Large-scale synthesis of uniform and extremely small-sized iron oxide nanoparticles for high-resolution T1 magnetic resonance imaging contrast agents. *J Am Chem Soc* **2011,** *133* (32), 12624-31.
80. Qiu, P.; Jensen, C.; Charity, N.; Towner, R.; Mao, C., Oil phase evaporation-induced self-assembly of hydrophobic nanoparticles into spherical clusters with controlled surface chemistry in an oil-in-water dispersion and comparison of behaviors of individual and clustered iron oxide nanoparticles. *J Am Chem Soc* **2010,** *132* (50), 17724-32.
81. Wu, M.; Zhang, D.; Zeng, Y.; Wu, L.; Liu, X.; Liu, J., Nanocluster of superparamagnetic iron oxide nanoparticles coated with poly (dopamine) for magnetic field-targeting, highly sensitive MRI and photothermal cancer therapy. *Nanotechnology* **2015,** *26* (11), 115102.
82. Sun, S. H.; Zeng, H.; Robinson, D. B.; Raoux, S.; Rice, P. M.; Wang, S. X.; Li, G. X., Monodisperse MFe2O4 (M = Fe, Co, Mn) nanoparticles. *Journal of the American Chemical Society* **2004,** *126* (1), 273-279.
83. Sun, S. H.; Zeng, H., Size-controlled synthesis of magnetite nanoparticles. *Journal of the American Chemical Society* **2002,** *124* (28), 8204-8205.
84. Park, J.; An, K. J.; Hwang, Y. S.; Park, J. G.; Noh, H. J.; Kim, J. Y.; Park, J. H.; Hwang, N. M.; Hyeon, T., Ultra-large-scale syntheses of monodisperse nanocrystals. *Nature Materials* **2004,** *3* (12), 891-895.
85. Wang, X.; Zhuang, J.; Peng, Q.; Li, Y. D., A general strategy for nanocrystal synthesis. *Nature* **2005,** *437* (7055), 121-124.
86. Wan, S. R.; Huang, J. S.; Yan, H. S.; Liu, K. L., Size-controlled preparation of magnetite nanoparticles in the presence of graft copolymers. *Journal of Materials Chemistry* **2006,** *16* (3), 298-303.
87. Li, Z.; Tan, B.; Allix, M.; Cooper, A. I.; Rosseinsky, M. J., Direct coprecipitation route to monodisperse dual-functionalized magnetic iron oxide nanocrystals without size selection. *Small* **2008,** *4* (2), 231-239.
88. Li, X. L.; Li, H.; Liu, G. Q.; Deng, Z. W.; Wu, S. L.; Li, P. H.; Xu, Z. S.; Xu, H. B.; Chu, P. K., Magnetite-loaded fluorine-containing polymeric micelles for magnetic resonance imaging and drug delivery. *Biomaterials* **2012,** *33* (10), 3013-3024.
89. Xie, Y. H.; Sougrat, R.; Nunes, S. P., Synthesis and Characterization of Polystyrene Coated Iron Oxide Nanoparticles and Asymmetric Assemblies by Phase Inversion. *Journal of Applied Polymer Science* **2015,** *132* (5).
90. Rusckowski, M.; Gupta, S.; Liu, G.; Dou, S.; Hnatowich, D. J., Investigations of a (99m)Tc-labeled bacteriophage as a potential infection-specific imaging agent. *J Nucl Med* **2004,** *45* (7), 1201-8.

91. Zhang, T. R.; Ge, J. P.; Hu, Y. X.; Yin, Y. D., A general approach for transferring hydrophobic nanocrystals into water. *Nano Letters* **2007,** *7* (10), 3203-3207.
92. Qiu, P. H.; Jensen, C.; Charity, N.; Towner, R.; Mao, C. B., Oil Phase Evaporation-Induced Self-Assembly of Hydrophobic Nanoparticles into Spherical Clusters with Controlled Surface Chemistry in an Oil-in-Water Dispersion and Comparison of Behaviors of Individual and Clustered Iron Oxide Nanoparticles. *Journal of the American Chemical Society* **2010,** *132* (50), 17724-17732.
93. Ge, J. P.; Hu, Y. X.; Biasini, M.; Dong, C. L.; Guo, J. H.; Beyermann, W. P.; Yin, Y. D., One-step synthesis of highly water-soluble magnetite colloidal nanocrystals. *Chemistry-a European Journal* **2007,** *13* (25), 7153-7161.
94. Ravikumar, C.; Bandyopadhyaya, R., Mechanistic Study on Magnetite Nanoparticle Formation by Thermal Decomposition and Coprecipitation Routes. *Journal of Physical Chemistry C* **2011,** *115* (5), 1380-1387.
95. Qiu, P. H.; Mao, C. B., Viscosity Gradient as a Novel Mechanism for the Centrifugation-Based Separation of Nanoparticles. *Advanced Materials* **2011,** *23* (42), 4880-4885.
96. Ban, E.; Chae, D. K.; Song, E. J., Determination of micro-RNA in cardiomyoblast cells using CE with LIF detection. *Electrophoresis* **2013,** *34* (4), 598-604.
97. Lee, Y. J.; Moon, S. U.; Park, M. G.; Jung, W. Y.; Park, Y. K.; Song, S. K.; Ryu, J. G.; Lee, Y. S.; Heo, H. J.; Gu, H. N.; Cho, S. J.; Ali, B. A.; Al-Khedhairy, A. A.; Lee, I.; Kim, S., Multiplex bioimaging of piRNA molecular pathway-regulated theragnostic effects in a single breast cancer cell using a piRNA molecular beacon. *Biomaterials* **2016,** *101*, 143-55.
98. Devaux, Y.; Mueller, M.; Haaf, P.; Goretti, E.; Twerenbold, R.; Zangrando, J.; Vausort, M.; Reichlin, T.; Wildi, K.; Moehring, B.; Wagner, D. R.; Mueller, C., Diagnostic and prognostic value of circulating microRNAs in patients with acute chest pain. *J Intern Med* **2015,** *277* (2), 260-71.
99. Wang, G. K.; Zhu, J. Q.; Zhang, J. T.; Li, Q.; Li, Y.; He, J.; Qin, Y. W.; Jing, Q., Circulating microRNA: a novel potential biomarker for early diagnosis of acute myocardial infarction in humans. *Eur Heart J* **2010,** *31* (6), 659-66.
100. Sun, X.; Jiang, S. W.; Liu, J.; Wang, H. Z.; Zhang, Y. W.; Tang, S. C.; Wang, J. C.; Du, N.; Xu, C. W.; Wang, C. G.; Qin, S. D.; Zhang, J.; Liu, D. P.; Zhang, Y. F.; Li, X. J.; Wang, J. S.; Dong, J.; Wang, X.; Xu, S. H.; Tao, Z.; Xu, F.; Zhou, J.; Wang, T.; Ren, H., MiR-208a stimulates the cocktail of SOX2 and beta-catenin to inhibit the let-7 induction of self-renewal repression of breast cancer stem cells and formed miR208a/let-7 feedback loop via LIN28 and DICER1. *Oncotarget* **2015,** *6* (32), 32944-32954.
101. Bachmayr-Heyda, A.; Reiner, A. T.; Auer, K.; Sukhbaatar, N.; Aust, S.; Bachleitner-Hofmann, T.; Mesteri, I.; Grunt, T. W.; Zeillinger, R.; Pils, D., Correlation of circular RNA abundance with proliferation--exemplified with colorectal and ovarian cancer, idiopathic lung fibrosis, and normal human tissues. *Sci Rep* **2015,** *5*, 8057.
102. Li, P.; Chen, S.; Chen, H.; Mo, X.; Li, T.; Shao, Y.; Xiao, B.; Guo, J., Using circular RNA as a novel type of biomarker in the screening of gastric cancer. *Clin Chim Acta* **2015,** *444*, 132-6.
103. Zhang, Y.; Yang, P.; Wang, X. F., Microenvironmental regulation of cancer metastasis by miRNAs. *Trends Cell Biol* **2014,** *24* (3), 153-60.
104. Gidlof, O.; Smith, J. G.; Miyazu, K.; Gilje, P.; Spencer, A.; Blomquist, S.; Erlinge, D., Circulating cardio-enriched microRNAs are associated with long-term prognosis following myocardial infarction. *BMC Cardiovasc Disord* **2013,** *13*, 12.
105. Widera, C.; Gupta, S. K.; Lorenzen, J. M.; Bang, C.; Bauersachs, J.; Bethmann, K.; Kempf, T.; Wollert, K. C.; Thum, T., Diagnostic and prognostic impact of six circulating microRNAs in acute coronary syndrome. *J Mol Cell Cardiol* **2011,** *51* (5), 872-5.
106. Li, W.; Wang, Y.; Zhang, Q.; Tang, L.; Liu, X.; Dai, Y.; Xiao, L.; Huang, S.; Chen, L.; Guo, Z.; Lu, J.; Yuan, K., MicroRNA-486 as a Biomarker for Early Diagnosis and Recurrence of Non-Small Cell Lung Cancer. *PLoS One* **2015,** *10* (8), e0134220.

107. Yin, Q. W.; Sun, X. F.; Yang, G. T.; Li, X. B.; Wu, M. S.; Zhao, J., Increased expression of microRNA-150 is associated with poor prognosis in non-small cell lung cancer. *Int J Clin Exp Patho* **2015,** *8* (1), 842-846.
108. Liu, X. G.; Zhu, W. Y.; Huang, Y. Y.; Ma, L. N.; Zhou, S. Q.; Wang, Y. K.; Zeng, F.; Zhou, J. H.; Zhang, Y. K., High expression of serum miR-21 and tumor miR-200c associated with poor prognosis in patients with lung cancer. *Med Oncol* **2012,** *29* (2), 618-26.
109. Hu, Z.; Zhang, A.; Storz, G.; Gottesman, S.; Leppla, S. H., An antibody-based microarray assay for small RNA detection. *Nucleic Acids Res* **2006,** *34* (7), e52.
110. Qavi, A. J.; Kindt, J. T.; Gleeson, M. A.; Bailey, R. C., Anti-DNA:RNA antibodies and silicon photonic microring resonators: increased sensitivity for multiplexed microRNA detection. *Anal Chem* **2011,** *83* (15), 5949-56.
111. Fang, J.; Subr, V.; Islam, W.; Hackbarth, S.; Islam, R.; Etrych, T.; Ulbrich, K.; Maeda, H., N-(2-hydroxypropyl)methacrylamide polymer conjugated pyropheophorbide-a, a promising tumor-targeted theranostic probe for photodynamic therapy and imaging. *Eur J Pharm Biopharm* **2018,** *130*, 165-176.
112. Wang, K.; Tang, Z.; Yang, C. J.; Kim, Y.; Fang, X.; Li, W.; Wu, Y.; Medley, C. D.; Cao, Z.; Li, J.; Colon, P.; Lin, H.; Tan, W., Molecular engineering of DNA: molecular beacons. *Angew Chem Int Ed Engl* **2009,** *48* (5), 856-70.
113. Zhang, Z.-M.; Chen, S.; Liang, Y.-Z.; Liu, Z.-X.; Zhang, Q.-M.; Ding, L.-X.; Ye, F.; Zhou, H., An intelligent background-correction algorithm for highly fluorescent samples in Raman spectroscopy. *Journal of Raman Spectroscopy* **2009,** *41* (6), 659-669.
114. Zhao, J.; Lui, H.; McLean, D. I.; Zeng, H., Automated Autofluorescence Background Subtraction Algorithm for Biomedical Raman Spectroscopy. *Appl. Spectrosc.* **2007,** *61* (11), 1225-1232.
115. Stark, L.; Giersch, T.; Wunschiers, R., Efficiency of RNA extraction from selected bacteria in the context of biogas production and metatranscriptomics. *Anaerobe* **2014,** *29*, 85-90.
116. Hagan, K. A.; Meier, W. L.; Ferrance, J. P.; Landers, J. P., Chitosan-Coated Silica as a Solid Phase for RNA Purification in a Microfluidic Device. *Analytical Chemistry* **2009,** *81* (13), 5249-5256.
117. Giloh, H.; Sedat, J. W., Fluorescence microscopy: reduced photobleaching of rhodamine and fluorescein protein conjugates by n-propyl gallate. *Science* **1982,** *217* (4566), 1252-5.
118. Song, L.; Hennink, E. J.; Young, I. T.; Tanke, H. J., Photobleaching kinetics of fluorescein in quantitative fluorescence microscopy. *Biophysical Journal* **1995,** *68* (6), 2588-2600.
119. Li, L. L.; Wu, P.; Hwang, K.; Lu, Y., An exceptionally simple strategy for DNA-functionalized up-conversion nanoparticles as biocompatible agents for nanoassembly, DNA delivery, and imaging. *J Am Chem Soc* **2013,** *135* (7), 2411-4.
120. Pallenberg, A. J.; Dobhal, M. P.; Pandey, R. K., Efficient Synthesis of Pyropheophorbide-a and Its Derivatives. *Organic Process Research & Development* **2004,** *8* (2), 287-290.
121. Zheng, G.; Chen, J.; Stefflova, K.; Jarvi, M.; Li, H.; Wilson, B. C., Photodynamic molecular beacon as an activatable photosensitizer based on protease-controlled singlet oxygen quenching and activation. *Proc Natl Acad Sci U S A* **2007,** *104* (21), 8989-94.
122. Hurst, S. J.; Lytton-Jean, A. K.; Mirkin, C. A., Maximizing DNA loading on a range of gold nanoparticle sizes. *Anal Chem* **2006,** *78* (24), 8313-8.
123. Levy, M.; Ellington, A. D., Directed evolution of streptavidin variants using in vitro compartmentalization. *Chem Biol* **2008,** *15* (9), 979-89.
124. Hirsch, J. D.; Eslamizar, L.; Filanoski, B. J.; Malekzadeh, N.; Haugland, R. P.; Beechem, J. M.; Haugland, R. P., Easily reversible desthiobiotin binding to streptavidin, avidin, and other biotin-binding proteins: uses for protein labeling, detection, and isolation. *Anal Biochem* **2002,** *308* (2), 343-57.
125. Shrivastava, A.; Gupta, V., Methods for the determination of limit of detection and limit of quantitation of the analytical methods. *Chronicles of Young Scientists* **2011,** *2* (1).

Appendix A: List of Abbreviations

2D	two-dimensional
3D	three-dimensional
AFP	alpha-fetoprotein
Au ND	gold nanodendrite
Au NP	gold nanoparticle
Au NR	gold nanorod
Au NS	gold nanostar
beta-HCG	beta-human chorionic Gonadotropin
CPM	count per minute
CT	computed tomography
CTAB	cetrimonium bromide
DIPEA	N,N-diisopropylethylamine
DMF	N,N-dimethylformamide
DTB	desthiobiotin
em	emission
EPR	Enhanced Permeability and Retention
ex	excitation
FDA	Food and Drug Administration
i.v.	intravenous
IONP	iron oxide nanoparticle
lncRNA	long non-coding RNA

MAG_3	mercatuacetyltriglycine
MB	molecular beacon
miRNA	micro RNA
MNP	magnetic nanoparticle
MNPC	magnetic iron oxide nanoparticle cluster
MRI	magnetic resonance imaging
ncRNA	non-coding RNA
NHS	N-hydroxysuccinimide
NIR	near-infrared
NM	nanomaterial
NP	nanoparticle
NPMB	nanoparticle-based MB
nt	nucleotide
PET	positron emission tomography
pyro	pyropheophorbide-a
qRT-PCR	Real-Time Quantitative Reverse Transcription polymerase chain reaction
ROI	region of interest
rpm	revolutions per minute
rRNA	ribosomal RNA
scaRNA	small cajal RNA
siRNA	short interfering RNA
sncRNA	small non-coding RNA

snoRNA	small nucleolar RNA
snRNA	small nuclear RNA
SOSG	Singlet Oxygen Sensor Green
SPECT	single-photon emission computed tomography
T_1	longitudinal relaxation time
T_2	transverse relaxation time
TBTU	N,N,N′,N′-tetramethyl-O-(benzotriazol-1-yl)uronium tetrafluoroborate
THF	tetrahydrofuran
tRNA	transfer RNA
WHO	World Health Organization
wt%	weight percent

Appendix B: List of Copyrights and Permissions

This Agreement between University of Oklahoma -- YUEYI SUN ("You") and Elsevier ("Elsevier") consists of your license details and the terms and conditions provided by Elsevier and Copyright Clearance Center.

License Number	4945390735432
License date	Nov 10, 2020
Licensed Content Publisher	Elsevier
Licensed Content Publication	Spectrochimica Acta Part A: Molecular and Biomolecular Spectroscopy
Licensed Content Title	A study on the sizes and concentrations of gold nanoparticles by spectra of absorption, resonance Rayleigh scattering and resonance non-linear scattering
Licensed Content Author	You Qiu He,Shao Pu Liu,Ling Kong,Zhong Fang Liu
Licensed Content Date	Oct 1, 2005
Licensed Content Volume	61
Licensed Content Issue	13-14
Licensed Content Pages	6
Start Page	2861
End Page	2866
Type of Use	reuse in a thesis/dissertation
Portion	figures/tables/illustrations
Number of figures/tables/illustrations	1

Permission for Figure 1.1

This is a License Agreement between Yueyi Sun ("You") and Royal Society of Chemistry ("Publisher") provided by Copyright Clearance Center ("CCC"). The license consists of your order details, the terms and conditions provided by Royal Society of Chemistry, and the CCC terms and conditions.

All payments must be made in full to CCC.

Order Date	10-Nov-2020	**Type of Use**	Republish in a thesis/dissertation
Order license ID	1076499-1	**Publisher**	ROYAL SOCIETY OF CHEMISTRY
ISSN	1364-548X	**Portion**	Image/photo/illustration

LICENSED CONTENT

Publication Title	Chemical communications	**Country**	United Kingdom of Great Britain and Northern Ireland
Author/Editor	Royal Society of Chemistry (Great Britain)	**Rightsholder**	Royal Society of Chemistry
Date	12/31/1995	**Publication Type**	e-Journal
Language	English		

REQUEST DETAILS

Portion Type	Image/photo/illustration	**Distribution**	United States
Number of images / photos / illustrations	1	**Translation**	Original language of publication
Format (select all that apply)	Electronic	**Copies for the disabled?**	No
Who will republish the content?	Academic institution	**Minor editing privileges?**	No
Duration of Use	Current edition and up to 5 years	**Incidental promotional use?**	No
Lifetime Unit Quantity	Up to 499	**Currency**	USD
Rights Requested	Main product		

Permission for Figure 1.2

informa healthcare

Gold nanoparticles: opportunities and challenges in nanomedicine

Author: Rochelle Arvizo, , Resham Bhattacharya, et al
Publication: Expert Opinion on Drug Delivery
Publisher: Taylor & Francis
Date: Jun 1, 2010

Rights managed by Taylor & Francis

Thesis/Dissertation Reuse Request

Taylor & Francis is pleased to offer reuses of its content for a thesis or dissertation free of charge contingent on resubmission of permission request if work is published.

BACK CLOSE

Permission for Figure 1.3

Reuse of Content Within a Thesis or Dissertation

Content (full-text or portions thereof) may be used in print and electronic versions of a dissertation or thesis without formal permission from the Massachusetts Medical Society (MMS), Publisher of the *New England Journal of Medicine*.

The following credit line must be printed along with the copyrighted material:

> Reproduced with permission from (scientific reference citation), Copyright Massachusetts Medical Society.

Permission for Figure 1.4

Permissions

No special permission is required to reuse all or part of article published by MDPI, including figures and tables. For articles published under an open access Creative Common CC BY license, any part of the article may be reused without permission provided that the original article is clearly cited. Reuse of an article does not imply endorsement by the authors or MDPI.

Permission for Figure 1.5 and 1.9

This is a License Agreement between Yueyi Sun ("You") and Royal Society of Chemistry ("Publisher") provided by Copyright Clearance Center ("CCC"). The license consists of your order details, the terms and conditions provided by Royal Society of Chemistry, and the CCC terms and conditions.

All payments must be made in full to CCC.

Order Date	10-Nov-2020	**Type of Use**	Republish in a thesis/dissertation
Order license ID	1076506-1	**Publisher**	Royal Society of Chemistry
ISSN	1364-5528	**Portion**	Image/photo/illustration

LICENSED CONTENT

Publication Title	The analyst online	**Country**	United Kingdom of Great Britain and Northern Ireland
Author/Editor	Society of Public Analysts (Great Britain), Chemical Society (Great Britain), Society for Analytical Chemistry, Society of Public Analysts (Great Britain), Royal Society of Chemistry (Great Britain)	**Rightsholder**	Royal Society of Chemistry
		Publication Type	e-Journal
		URL	http://www.rsc.org/is/journals/current/an...
Date	12/31/1875		
Language	English		

REQUEST DETAILS

Portion Type	Image/photo/illustration	**Distribution**	United States
Number of images / photos / illustrations	1	**Translation**	Original language of publication
Format (select all that apply)	Electronic	**Copies for the disabled?**	No
Who will republish the content?	Academic institution	**Minor editing privileges?**	No
Duration of Use	Current edition and up to 5 years	**Incidental promotional use?**	No
Lifetime Unit Quantity	Up to 499	**Currency**	USD
Rights Requested	Main product		

Permission for Figure 1.6

This Agreement between University of Oklahoma -- YUEYI SUN ("You") and John Wiley and Sons ("John Wiley and Sons") consists of your license details and the terms and conditions provided by John Wiley and Sons and Copyright Clearance Center.

License Number	4945401117547
License date	Nov 10, 2020
Licensed Content Publisher	John Wiley and Sons
Licensed Content Publication	Advanced Materials
Licensed Content Title	Recent Advances in Upconversion Nanoparticles-Based Multifunctional Nanocomposites for Combined Cancer Therapy
Licensed Content Author	Gan Tian, Xiao Zhang, Zhanjun Gu, et al
Licensed Content Date	Oct 27, 2015
Licensed Content Volume	27
Licensed Content Issue	47
Licensed Content Pages	21
Type of use	Dissertation/Thesis
Requestor type	University/Academic
Format	Electronic
Portion	Figure/table

Permission for Figure 1.7

This is a human-readable summary of (and not a substitute for) the license. Disclaimer.

You are free to:

Share — copy and redistribute the material in any medium or format

Adapt — remix, transform, and build upon the material for any purpose, even commercially.

The licensor cannot revoke these freedoms as long as you follow the license terms.



Permission for Figure 1.8

This Agreement between University of Oklahoma -- YUEYI SUN ("You") and Springer Nature ("Springer Nature") consists of your license details and the terms and conditions provided by Springer Nature and Copyright Clearance Center.

License Number	4945410075877
License date	Nov 10, 2020
Licensed Content Publisher	Springer Nature
Licensed Content Publication	Springer eBook
Licensed Content Title	Selection of Recombinant Human Antibodies
Licensed Content Author	Florian Tomszak, Susanne Weber, Jonas Zantow et al
Licensed Content Date	Jan 1, 2016
Type of Use	Thesis/Dissertation
Requestor type	academic/university or research institute
Format	electronic
Portion	figures/tables/illustrations
Number of figures/tables/illustrations	1
Will you be translating?	no
Circulation/distribution	1 - 29

Permission for Figure 1.10